Arrays of gold nanoparticles as a platform for molecular electronics

Inauguraldissertation

zur
Erlangung der Würde eines Doktors der Philosophie
vorgelegt der
Philosophisch-Naturwissenschaftlichen Fakultät
der Universität Basel

von

Jón Skírnir Ágústsson
aus Reykjavík (IS)

UNI
BASEL

Basel, 2012

Genehmigt von der Philosophisch-Naturwissenschaftlichen Fakultät
auf Antrag von
Prof. Dr. Christian Schönenberger
Dr.ir. Sense Jan van der Molen
Dr. Aidan Quinn
Dr. Michel Calame

Basel, den 21. June 2011

<div style="text-align:right">

Prof. Dr. Martin Spiess
Dekan

</div>

*An expert is a man who has made all the mistakes
which can be made in a very narrow field.*
Niels Bohr

Contents

List of Figures

List of Tables

Chapter 1

Introduction

In recent years electronic devices based on organic molecules have emerged. Recently applications utilising organic light emitting diodes (OLED) have become available in commercial products. The development of organic, plastic, electronic devices has paved the way for printable and flexible electronic devices. Modern organic electronic devices are based on conducting or semiconducting polymers [25]. Since polymers are composed of chains of molecules it is reasonable to ask whether the function of an electronic device could be derived from a single molecule. The idea that, indeed, it is possible to construct a functional electronic component out of a single molecule was put forward in the seventies [5]. As fascinating as the idea may be, it left a big unanswered question: How does one bring electrical contacts to a single molecule?

Many scientists have pondered the question and many solutions have been proposed. Most of the devices used to contact molecules today comprise of a molecule bound to a substrate and contacted with an atomically sharp metallic tip (STM break junction) or the molecule contacted by a pair of atomically sharp metallic tips (Mechanically controllable break junction) [46]. These devices work very well in a laboratory setting, but suffer from the fact that they are not suited to applications outside the laboratory. Other kinds of devices have also been built, such as self assembled monolayers of molecules on an metallic substrate contacted with a relatively soft metallic electrode [46]. These devices are prone to metallic shortcuts forming between the electrodes. They are also difficult to use in devices where the function of the device depends on the interaction of the molecules with the environment.

Self assembled arrays of metallic nanoparticles can be used as a platform for molecular electronic devices. Devices are then made by coating the nanoparticles

by an organic molecule and allowing the metallic, usually gold, nanoparticles to self assemble into well ordered structures. Devices made from those arrays can be operated outside of the laboratory and do not depend on specialised equipment to retain their function. The structure of the devices can be such that the molecules covering the nanoparticles can interact with the environment.
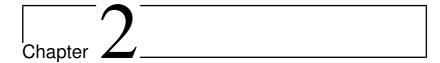
Large arrays, comprising of millions of nanoparticles, are useful as a platform for molecular electronics. They have been used to measure the conductance of several molecules and even been used to build devices where the function of the individual molecules, bridging the nanoparticles, defines the function of the device. It is challenging to precisely control the geometry of devices made by arrays of nanoparticles. Making small arrays, where several hundreds or thousands of nanoparticles make up the array, is difficult. However, making these small arrays is useful if one wants to investigate the details of the transport through the arrays.

In this thesis, we will focus on the challenges stated above. In particular, we will discuss measurements on nanoparticle array devices, where the function of the device is determined by the function of the individual molecules bridging the nanoparticles. We will also see how it is possible to control the geometry of the nanoparticle array devices. The ability to make smaller nanoparticle arrays opens up the possibility to investigate the transport through the devices in more detail, as we will do.

The thesis is presented in two parts. Part I focuses on measurements of active molecular devices at room temperature. Chapter 2 shows how the nanoparticle array devices are fabricated. Chapter 3 introduces an experiment where redox–active molecules were introduced to the nanoparticle array devices and used to tune their conductance. In Part II we change the temperature and move on towards liquid He temperatures. In Chapter 4 we discuss how to fabricate small nanoparticle arrays. We look at the contribution from the nanoparticles to the transport of the nanoparticle arrays in Chapter 5. In Chapter 6 we look at the contribution of the molecules to the transport in the arrays. In particular, we look at the contribution of the vibrational modes of the molecules to the transport. Chapter 7 contains the conclusions and an outlook on the project.

Part I

Nanoparticle arrays as a platform for molecular devices

Chapter 2

Device fabrication

2.1 Introduction

The greatest challenge in measuring the electrical properties of a single molecule is how to contact it with electrodes. To be able to contact a single molecule one needs to prepare electrodes that have similar dimensions as the molecule, attach them at the desired positions on the molecule, and hold the assembly stable during the measurement.

Several methods of bringing electrical contacts to a single molecule have been used. The most well known methods are the scanning tunnelling microscope break junction method [22] and the mechanically controlled break junction [48]. These methods have the advantage of contacting only a single, or a few (< 100) molecules in parallel, at once. These methods are not practical for device applications since they do not scale well and due to drift and fluctuations, in these molecular junctions, they are not stable for more than a few minutes or hours.

One way to contact an individual molecule is to prepare an ordered array of electrodes. This array is analogous to the breadboard used for the prototyping of electrical circuits. The array provides well defined docking sites where molecules can interlink the electrodes in the array to produce a network. The network then consists of many electrode–molecule–electrode junctions; and each junction is made up of a single molecule bridging a pair of electrodes.

In order to fabricate an array of electrodes as described above Liao et al. [43] synthesized colloidal Au nanoparticles with a diameter of 10 nm. The nanoparticles were coated with monothiolated carbon chains (alkane monothiols) to prevent them from aggregating and to control the interparticle distance in the array. The nanoparticles were then allowed to self–assemble into hexagonally close–

packed arrays, where the interparticle distance was ~2 nm and the curvature of the nanoparticles was such that only a few molecules could bridge two neighbouring nanoparticles. Using nanoparticles with a 10 nm diameter, assuming a ±10% size distribution of the nanoparticles, and a 1 nm^2 area of the nanoparticle surface occupied by each molecule: Fewer than 100 molecules, each 2 nm long, can bridge two neighbouring nanoparticles.

Liao et al. [43] and Bernard et al. [9] demonstrated that the saturated carbon chains coating the nanoparticles can be partially replaced by a new molecule. By choosing a molecular rod of the correct length that could bind to gold on each end, Liao et al. [44] showed that a network was formed by the new molecules interlinking the nanoparticles. The nanoparticle arrays have been shown to be stable and versatile platforms for molecular electronics. First of all, the nanoparticle arrays can withstand common solvents and thus it is possible to perform molecular place–exchange to insert new molecules into them [9, 42, 43, 44, 73]. Molecules designed with a specific function can retain their function after insertion into the nanoparticle arrays. This opens up the way to fabricate functional devices where the function is derived from the molecules in the nanoparticle arrays [42, 73].

In this chapter the synthesis of gold nanoparticles, preparation of nanoparticle arrays, and device preparation is described. For full details on the protocol refer to Appendix D.

2.2 Preparation of Au nanoparticles and Au nanoparticle arrays

Gold colloidal particles (Au nanoparticles) with a 10 nm diameter were synthesized by the reduction of chloroauric acid (HAuCl$_4$·H$_2$O) with trisodium citrate (C$_6$H$_5$O$_7$Na$_3$·2H$_2$O) and tannic acid (C$_{14}$H$_{10}$O$_9$) in deionised water (DI-H$_2$O) [43, 71], Figure 2.1(a). The nanoparticles were transferred from water to ethanol (CH$_3$CH$_2$OH) by centrifugation and mixed with monothiolated alkane ligands (i.e. C$_8$H$_{18}$S, hereafter known as C8). The concentration of nanoparticles in the solution is $\sim 10^{13}$ NP/ml. Typically, 10 ml of a solution containing the nanoparticles in ethanol was mixed with 200 μl of the ligand. After 48 hours the ligands had covered the nanoparticles. When covered, the nanoparticles precipitated to the bottom of the container. By pipetting the excess ethanol from the container and replacing it with new ethanol, the excess ligands were removed from the solution. After precipitation the ethanol was removed and the nanoparticles were dispersed in 4 ml chloroform (CHCl$_3$) by an ultrasonic treatment, Figure 2.1(b).

Patterned 2D nanoparticle arrays were prepared by a combination of self–assembly and micro–contact printing [43, 61, 62]. The solution of nanoparticles in chloroform was spread on a convex water surface with a pipette. During the evaporation of the solvent, the alkanethiol–capped Au nanoparticles self–assembled into a 2D array at the air–water interface. Patterned polydimethylsiloxane (PDMS, (C$_2$H$_6$OSi)$_n$) stamps

(a)

- 1 ml 1% weight to volume Gold(III) chloride hydrate (HAuCl$_4$ · 4H$_2$O)
- 79 ml de-ionized water (DI-H$_2$O)

- 4 ml 1% weight to volume Sodium citrate tribasic dihydrate (C$_6$H$_5$O$_7$Na$_3$ · 2H$_2$O)
- 80 µl 1% weight to volume Tannic acid (C$_{76}$H$_{52}$O$_{46}$)
- 16 ml de-ionized water (DI-H$_2$O)

- Heat to 80° C
- Mix solutions
- Bring to boiling
- Stirr and keep boiling
- Solution turns purple

- After 15 minutes
- Solution turns bright red
- Nanoparticles are ready
- Cool in ice water
- Place in a glass bottle for storing.

(b)

- Put 1 ml of the nanoparticle solution in eppendorfs
- Centrefuge to seperate nanoparticles from the water.

- Remove the Water from the nanoparticles
- Add 1ml ethanol in each eppendorf

- Add 200 µl of ligand to the solution
- When the ligands cover the nanoparticles they percipitate to the bottom of the container.

- Remove the ethanol
- Add 4 ml of chloroform
- Sonicate to resuspend the nanoparticles.

(c)

- Suspend the solution of nanoparticles in chloroform on top of a convex water surface.

- Ink a patterned PDMS stamp with the nanoparticle array on the water air interface.

(d)

- Place the PDMS stamp with the nanoparticle array on the substrate.

- After stamping lines of nanoparticle arrays are left on the substrate.

- Use TEM grids as shadow masks to pattern electrodes
- One device is composed of two adjacent contact pads and the nanopartice array between them.

Figure 2.1: The synthesis of Au nanoparticles is illustrated in Figure (a). Heated solutions of 4 ml C$_6$H$_5$O$_7$Na$_3$ and C$_{14}$H$_{10}$O$_9$ in DI–H$_2$O are mixed with 1 ml 1% (w/v) HAuCl$_4$ in DI–H$_2$O. The solution is heated to boiling and stirred continuously for 15 minutes. Figure (b) illustrates how the nanoparticles are removed from the aqueous solution and transferred to ethanol. The ligand used to cover the nanoparticles is added to the ethanol solution. After 2-3 days the ligand has covered the nanoparticles and they precipitate to the bottom of the container. Before using the nanoparticles they are re–suspended in 4 ml of chloroform using an ultrasonic treatment. Figure (c) illustrates how a convex water surface is made in the centre of a Teflon disk with a hole in it. The solution of the nanoparticles in chloroform is suspended on top of the convex water surface. The nanoparticles self–assemble into an array during solvent evaporation. Figure (d) shows how a PDMS stamp can be used to transfer the nanoparticle array from the air/water interface to a substrate. Patterns on the PDMS stamps control the geometry of the nanoparticle array on the substrate. TEM grids are used as a shadow mask to deposit on top of the nanoparticle arrays.

were used to transfer the 2D array from the water surface onto a solid SiO$_2$/Si substrate. The pattern consisted of 20 μm wide lines with a spacing of 20 μm [43, 44]. Metallic contact pads (5 nm Ti and 45 nm Au) were evaporated on top of the

nanoparticle arrays using transmission electron microscope (TEM) grids as shadow masks. A device is formed by two adjacent contact pads and the nanoparticle array between them, Figure 2.1(c)–(d). Figure 2.2(a) shows a scanning electron microscope (SEM) image of several devices. The large light squares are the contact pads, the two horizontal dashed lines emphasise a 20 μm wide nanoparticle array connecting the contact pads, and the two vertical dashed lines emphasize the length of one device, 10 μm, between two contact pads. The array size, within a single device, is $\sim$ 10 x 20 μm^2, consisting of $\sim 10^7$ molecular junctions. Figures 2.2(b) and (c) show SEM images of a nanoparticle array stamped on a SiO$_2$ substrate. Figure 2.2(b) shows the overall ordering of the nanoparticles in the array. The array consists of a monolayer of the nanoparticles, globally the nanoparticles form crystallites with a few vacancy defects. Figure 2.2(c) is a close up of the nanoparticle array. It shows that the nanoparticles arrange locally in a hexagonally close packed formation within each crystallite. Figure 2.2(d) is a schematic showing how the alkane ligands, white rods, coat the Au nanoparticles, yellow spheres. Dithiolated molecules, blue rods with a white sphere at each end, can interlink two neighbouring nanoparticles, emphasised with a red arrow. The dithiolated molecules can also bind to the nanoparticles with one thiol while the other thiol is free, emphasised with red circles around the white spheres.

2.3 Au nanoparticle arrays as a platform for molecular electronics

Arrays of alkane monothiol covered Au nanoparticles can be thought of as a platform for transport measurements of molecules. After stamping the arrays onto a substrate and depositing electrodes on top of them, a new molecule can be inserted into the arrays. The samples can be placed in a solution containing a relatively high ($\sim$ 1 mM) concentration of the new molecule. Monothiol ligands covering the Au nanoparticles can be partially replaced by new thiolated molecules [9, 16, 29, 43, 44]. Since the surface of the nanoparticles is highly mobile there is a probability that an alkane monothiol is desorbed from it and a new molecule can bind to the nanoparticles where there is a vacancy in the alkane layer. If the new molecule is a rod of the correct length and has groups on both ends that can bind strongly to Au, i.e. thiols, there is a probability that if it binds to a nanoparticle on one side it may find a vacancy on a neighbouring nanoparticle and bind there. Thus, bridging two neighbouring nanoparticles.

It has been shown that the arrays can resist common solvents such as deionised water, ethanol and tetrahydrofouran (THF, C$_4$H$_8$O). Molecular place–exchange in a solvent has been shown to work. Optical and electrical measurements were used to confirm that dithiolated molecules can interlink neighbouring nanoparticles in the array. It has been estimated that 20%–40% of the original ligands are replaced by
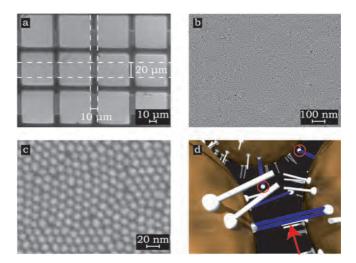
Figure 2.2: An overview of the devices used to measure molecular junctions. (a) The nanoparticle array width is 20 μm and the distance between two neighbouring contact pads is 10 μm. Each device consists of two large Ti/Au contact pads and the nanoparticle array between them. The scale bar is 100 μm. (b) and (c) show close ups of the Au nanoparticle array taken by SEM. Figure (b) shows the global ordering of the nanoparticles in the array. The array is a monolayer, comprised of crystallites with a few vacancy defects. Figure (c) shows how the nanoparticles arrange in a hexagonally close packed arrangement within each crystallite. Figure (d) is a schematic showing the relatively large Au nanoparticles covered with octanethiols (white rods) and a conjugated molecule of interest (blue double rods). The figure depicts that some of the dithiolated conjugated molecules can bridge two neighbouring nanoparticles, highlighted with a red arrow, while others have only one thiol connected to a nanoparticle and the other thiol is free, highlighted with red circles around the free thiol.

the new molecules [9, 43, 44]. Figure 2.2(d) illustrates how two Au nanoparticles covered with monothiols (white rods) can be interconnected by a dithiol (blue double rod). However, only a fraction of these incoming molecules have a chance to form two bonds with the gold surfaces available and effectively bridge two neighbouring nanoparticles. For geometrical reasons, a part of the dithiolated molecules can only bind to the gold surface via one anchor group, leaving the other end–thiol group free as shown by spectroscopic characterisation [34].

Chapter 3

Adding function to nanoparticle arrays

3.1 Introduction

The field of molecular electronics was started when it was first proposed that one could build an electrical device which utilised the function of a single molecule placed between two electrodes [5]. Since then several groups have pursued this goal and achieved molecular devices which have a function based on the properties of a single molecule. Several devices have been fabricated, where the conductance of the device can be switched from a high conducting state to a low conducting state and back, due to the properties of a single molecule. The simplest molecule used in such a device was a single H_2 molecule trapped between two gold electrodes of a cryogenic mechanically controllable break junction [70]. There Trouwborst et al. [70] switched the conductance of the molecular junction by applying a bias to it. Several other devices containing larger organic molecules have also been proposed and fabricated [33].

Using the nanoparticle array platform outlined in Chapter 2 two distinctively different devices have been produced. The first was an optically sensitive device based on a photochromic diarylethene molecule [73]. The conjugation of this molecule could be altered by exposing it to light at the correct wavelength. By exposing the molecule in a solution to visible light, in the range from 590 nm to 650 nm, the conjugation was broken in the center of the molecule. By exposing the molecule to UV light, in the range from 300 nm to 400 nm, the conjugation was restored. This function was preserved when the molecule was inserted into the nanoparticle arrays. Using this scheme the conductance of the nanoparticle arrays could be switched from a high conducting state, fully conjugated molecule, to a low conducting state, conjugation broken. This switching was reversible and could be

repeated several times. These measurements were performed in Ar atmosphere at room temperature.

In this work, a different scheme involved inserting a Tetrathiafulvalene (TTF, $(H_2C_2S_2C)_2$) molecule into the arrays. TTF is a redox active molecule, meaning that the charge of the molecule can be changed by oxidation and reduction. The TTF and its derivatives have been used as organic metals and superconductors since their discovery in the 1970's [8].

In this chapter we discuss how a redox–active molecule, TTF, can be inserted into the nanoparticle array devices. First we confirm that we can tune the oxidation state of the molecule in solution, then insert the molecule into the nanoparticle arrays and measure the conductance of the devices at different oxidation states of the molecule. To prove that the changes in conductance observed are due to the TTF molecule and not something else we did two control experiments, which are covered towards the end of the chapter.

3.2 Controlling the oxidation state of a redox–active molecule

The TTF derivative under investigation is depicted in Figure 3.1. The molecule is composed of a TTF redox group in the center, three methylene units on each side, and a thiol anchor group at each end of the molecule. From now on the TTF dithiol molecule will be known as TTFDT.

The oxidation state of the TTFDT can be changed by a chemical reaction using an oxidant (i.e. iron(III) chloride, $FeCl_3 \cdot 6h_2O$) and a reductant (i.e. ferrocene, $Fe(C_5H_5)_2$). The absorption spectra of several TTF derivatives, in different oxidation states, have been measured [75, 76]. The maximum absorption peak of the TTF derivatives has been found to move towards longer wavelengths, towards the red, when the oxidation state changes from the neutral state to the cation–radical ($TTF^{\bullet+}$) state. Even more redshift is measured when the molecule is oxidised to the dication (TTF^{2+}) state. This redshift of the absorption peak is attributed to an extension of the π–conjugation of the TTF unit. These measurements indicate that the π–conjugation is especially extended in the case of the dication. The increase in delocalisation of the π–conjugation should increase the conductance of the molecule.

Before introducing the TTFDT into the nanoparticle arrays, UV–Vis absorption measurements were used to confirm the reversible redox properties of the molecule in solution. Acetyl–protected TTFDT molecules were used to prevent the reaction between two free thiols. The measurements were carried out in a solution of acetonitrile (ACN, C_2H_3N). The oxidation to the cation–radical ($TTFDT^{\bullet+}$) and dication ($TTFDT^{2+}$) states was performed by respectively adding $FeCl_3$ in an 1:1 and a 2:1 ratio to the TTF in solution. The reduction was performed by adding ferrocene to the solution.

Figure 3.2 shows the UV–Vis absorption of the protected TTFDT in the ACN
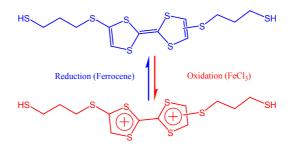
Figure 3.1: A schematic showing the TTFDT in blue. The molecule is composed of a TTF center, with a chain of three methylene units on each side. Terminating the free ends of the methylene chains are thiol groups, which bind to the gold nanoparticles. After oxidation with an superfluous amount of iron chloride two electrons are removed from the TTF center. The molecule can be reduced back to its uncharged state by ferrocene.

solution at different oxidation states. The initial absorption of the molecule is shown with the blue line. The spectrum has a strong absorption peak around 320 nm and a small shoulder around 370 nm. When the molecule is in the cation–radical state, the black line in Figure 3.2, two absorption peaks are visible one around 450 nm and the second around 700 nm. When the molecule is in the dication state, red line, a single absorption peak is visible around 550 nm. The molecule can be reduced back to the TTF cation–radical state by adding ferrocene to the solution. The green curve in Figure 3.2 shows the absorption of the TTFDT$^{\bullet+}$ after reduction and by further increasing the amount of ferrocene the molecule is reduced back to the neutral state shown by the orange curve in the figure. The inset in Figure 3.2 shows the oxidation cycle performed in the measurement and relates the colours of the lines to the corresponding oxidation states of the molecule.

It is obvious that the absorption spectrum of the TTFDT in the ground state before oxidation, blue line in Figure 3.2, and after reduction, orange line in Figure 3.2, is not the same. This change in the absorption is attributed to the iron chloride and ferrocene in the solution. Figure 3.3 shows the absorption of the TTFDT molecule in ACN, blue line, and the TTFDT in the neutral state after oxidation and reduction, orange line. To verify the contribution of iron chloride and ferrocene to the absorption a solution was prepared with the same amount, of iron chloride and ferrocene in ACN, as was used to oxidise and reduce the TTFDT molecule. No TTFDT molecules were added
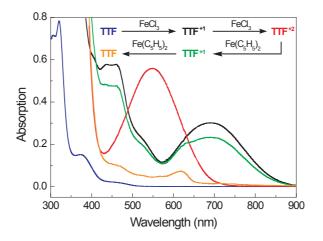
Figure 3.2: The absorption of the TTF molecule in a solution of ACN as prepared (blue), oxidised to the +1 state (black), oxidised to the +2 state (red), reduced from +2 to +1 (green), and reduced from the +1 to the ground state (orange). The TTF in the ground state shows a single absorption peak at 320 nm and a shoulder around 370 nm. The +1 state shows two absorption peaks one at 450 nm and the other at 700 nm. The +2 state shows one absorption peak at 550 nm. The difference between the as prepared TTF and the ground state TTF after reduction can be attributed to oxidised ferrocene in the solution.

to this reference solution. The absorption of the iron chloride and ferrocene in ACN is shown by the green line in Figure 3.3. The curve shows a small peak around 620 nm, similar to the peak in the orange curve. This feature stems from the absorption of oxidised ferrocene in the solution. From these absorption measurements we conclude that the oxidation state of the TTFDT molecule can be controlled by iron chloride and ferrocene.

3.3 Introducing function to the nanoparticle arrays

To investigate the influence of the oxidation state of the TTFDT molecule we prepared nanoparticle array devices and inserted the molecule into them. The devices of nanoparticle arrays were fabricated, as described in Chapter 2, to measure the electrical properties of the TTFDT. Colloidal Au nanoparticles with 10 nm diameter were synthesised and coated with octane monothiol ligands. The coated nanoparticles were allowed to self assemble at a water–air interface and the self assembled array was transferred to a Si/SiO$_2$ substrate using patterned PDMS stamps. The pattern on
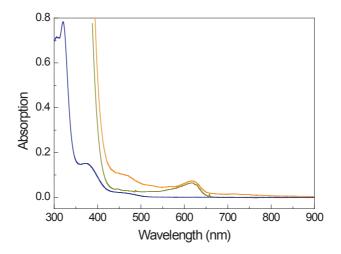
Figure 3.3: The blue line shows the absorption of TTFDT in ACN before oxidation, same as in Figure 3.2. The orange line show the absorption of the TTFDT in the neutral state after oxidation and reduction, same as in Figure 3.2. The green line shows the absorption of iron chloride and ferrocene in ACN with out the TTFDT molecule. The small peak observed around 620 nm can be attributed to oxidised ferrocene in the solution. The increase in absorption below 400 nm is attributed to the iron chloride in the solution.

the PDMS stamps consisted of 20 μm wide lines. Using a TEM grid as a shadow mask Ti/Au (5 nm/45 nm) contact pads were evaporated on top of the nanoparticle array.

The conductance of the devices was measured by applying a dc voltage and measuring the resulting current through the device. The I–V measurements were performed in a probe station in air at room temperature. A National Instrument DAQ board was used to apply the dc voltage. The current was measured by a DL1212 I/V converter and the voltage output of the I/V converter was measured by the DAQ board. The measurement was controlled by a LabView program.

After measuring the conductance of the devices with the C8 covered nanoparticles molecular place–exchange was used to insert the TTFDT into the arrays. During the molecular place–exchange the TTFDT partially replaces the C8 monothiols covering the gold nanoparticles. A solution of 1mM TTFDT in THF was prepared and the sample immersed in it for more than 24 hrs. After molecular place–exchange the sample was removed from the solution, rinsed in THF and blow dried with nitrogen gas. TTFDT has eight sulphur atoms. On a bare Au surface any of these eight sulphurs can coordinate with the Au. Since the nanoparticles were covered with

the C8 monothiols during the molecular place–exchange, the TTFDT can only bind
to the nanoparticles by the thiol groups at each end of the molecule. Even if the
TTFDT could bind to the nanoparticles in a different way, i.e. by other sulphur atoms
in the molecule, the distance between the nanoparticles inhibits those molecule from
bridging two neighbouring nanoparticles. After the molecular place–exchange the
conductance of the same devices as before was measured using the probe station
setup.

Oxidation was performed by placing the sample in 10 mM iron(III) chloride
dissolved in DI–H_2O for 40 min, each cycle. After oxidation the sample was removed
from the solution, rinsed with DI–H_2O, and blown dry with nitrogen. After oxidation
the conductance of the same devices was measured again with the probe station
setup. The oxidised TTF was reduced by placing the sample in a 10 mM solution
of ferrocene in THF overnight. After reduction the sample was removed from the
solution, rinsed with THF, and blown dry with nitrogen gas. After reduction the
conductance of the same devices were measured again. These *IV* measurements were
repeated after each oxidation and reduction step.

The TTFDT in the nanoparticle arrays was only oxidised to the TTFDT^{+2} state.
This is because it is impossible to know exactly how many TTFDT molecules are in
the nanoparticle arrays and thus impossible to add exactly 1:1 ratio of TTFDT:$FeCl_3$.
In order to have well controlled experiments we chose to investigate only the
TTFDT^{+2} state. This was easy to obtain by adding a superfluous amount of iron
chloride during oxidation.

3.4 Defining the conductance of a nanoparticle array device with the oxidation state of a molecule

Figure 3.4 shows the sheet conductance $G_{\square} = G \cdot l/w$ of 24 devices on one silicon
chip obtained from the measured conductance G, where l and w are the distance
between two electrodes and the width of the nanoparticle array, respectively. Figure
3.4(a) shows the sheet conductance of the 24 devices measured while Figure 3.4(b)
shows histograms of the conductance values in Figure 3.4(a). The conductance
was measured before molecular place–exchange (turquoise squares), after molecular
place–exchange (dark blue dots), after the first oxidation with excess iron chloride
(red up triangles), and the first reduction with excess ferrocene (orange down
triangles).

The conductance is low in the devices containing only C8 in the nanoparticle
arrays. This is expected since the C8 molecule is saturated, and thus insulating.
Furthermore, these molecules have only one thiol group, binding each molecule to
only one Au nanoparticle. After the molecular place–exchange with TTFDT the
conductance of the devices increases by one order of magnitude. This reflects the
higher conductance of the partly conjugated TTFDT molecule. After oxidation in
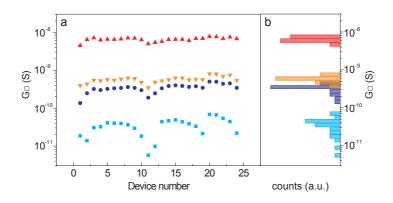
Figure 3.4: (a) The measured sheet conductance values of TTFDT in Au nanoparticle array devices, 24 devices were measured on one sample. The figure shows the conductance of the devices as prepared with C8 (■), after molecular place–exchange with TTFDT (●), after the oxidation (▲), and after reduction (▼). (b) Histograms of the measurement points in Figure (a). The conductance increases by an order of magnitude after molecular place–exchange. After oxidation the conductance increases about a factor of 20. After reduction the conductance is decreased by about one order of magnitude. The conductance after reduction is about a factor of 2 higher than the conductance of the devices after molecular place–exchange and before the oxidation.

an excess of iron chloride the conductance of the devices increases by a factor of 20 and after reduction the conductance decreases by one order of magnitude. The conductance of the devices after reduction is a factor of 2 higher than in the devices before oxidation. This point will be discussed late in this section.

At this point it is tempting to contribute the change in conductance to the oxidation and reduction of the TTF center of the molecules. Indeed the UV–Vis spectra of the TTFDT in its neutral and dicationic states clearly differentiate the underlying molecular obital situations [75]. To prove that the conductance changes are indeed due to the oxidation and reduction of the TTF centers we performed control experiments.

Firstly, we wanted to investigate whether ions were getting trapped in the arrays during oxidation and then removed during reduction. Using a sample with 20 devices containing C8 covered Au nanoparticles, we performed the same oxidation–reduction experiment as before. Figure 3.5 shows the sheet conductance of the devices and a histogram of the measured sheet conductances. The figure shows that the conductance of the devices does not change systematically or significantly after the oxidation and the reduction. This proves that the conductance of the TTF devices
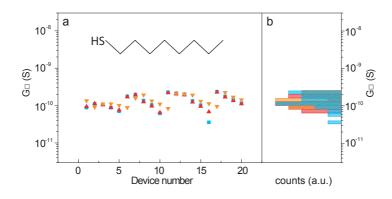
Figure 3.5: The conductance of 20 devices on one sample, as prepared with C8 (■), after the oxidation (▲), and after reduction (▼). The figure shows that the oxidation and reduction have no systematic or significant effect on the conductance of devices with only C8 covered Au nanoparticles.

was not caused by ions being trapped in the arrays during oxidation and removed during reduction.

As a second control, we repeated a similar experiment after inserting a conjugated compound into the nanoparticle arrays. This compound should not be influenced by the oxidation and reduction agents. Before molecular place–exchange the conductance of 21 as prepared devices, containing only C8, on one sample was measured. After measuring the conductance of the devices dithiolated oligo(phenylene vinylene)(OPVDT) was inserted into the arrays, see inset Figure 3.6 for the molecular structure. Figure 3.6 shows the sheet conductance of the 21 devices after molecular place–exchange, blue circles. It is interesting to note in Figure 3.6, that after oxidation the conductance increases by a factor of 2, red up triangles, and does not decrease after reduction, orange down triangles. The increase in conductance after the oxidation is similar to what is seen in Figure 3.4 after reduction. This point will be discussed later in the text.

Table 3.1 summarises the results of the three experiments. $G_\square^i$ corresponds to the averaged sheet conductance measured after molecular place–exchange, in the case of the TTFDT and the OPVDT, or directly after stamping, in the case of the C8. $G_\square^{ox}$ and $G_\square^{re}$ correspond to the average conductances measured after oxidation and reduction, respectively. In all three experiments we characterised more than 20 devices on a single silicone chip. The data in Table 3.1 show that devices containing TTFDT
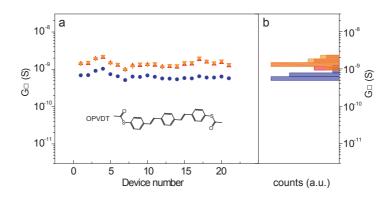
Figure 3.6: The measured conductance values of OPVDT in Au nanoparticle array devices, 21 devices were measured on one sample. The conductance was measured after molecular place–exchange with OPVDT (●), after the oxidation (▲), and reduction (▼). After oxidation the conductance of the devices increases. After reduction the conductance of the OPV does not return to the original conductance value of the OPV. This is similar to the change observed in devices with TTF, Figure 3.4.

compounds exhibit on average a conductance change of one order of magnitude while, devices containing C8 the conductance remains constant. Devices containing OPVDT show an increase in conductance of a factor of 2.2 after oxidation while no change is observed after reduction.

As seen in Table 3.1 the conductance of the devices containing TTFDT or OPVDT measured after reduction is not the same as the conductance of these devices before oxidation. Rather, the conductance increases by about factor of 2. In the devices containing C8 this increase in conductance is not observed. Notice that the C8 molecules carry only a single thiol anchor group while both TTFDT and OPVDT carry two. We attribute the effect described above to the presence of free thiol groups after molecular place–exchange. As mentioned in Chapter 2 due to geometrical reasons, only a fraction of the molecules introduced into the arrays during molecular place–exchange can bind to a gold surface with both thiol groups. This results in the presence of free unbound thiols in the arrays. It can therefore be expected that, during immersion of the sample in the oxidation solution, the free thiol groups will coordinate with the iron species present, thereby altering the overall conductance of the array. In the case of C8, the situation is different since no free thiols are available. Here, no conductance change was observed after immersion in the oxidation solution.

molecule	$G_\square^i$ [nS]	$G_\square^{ox}/G_\square^i$	$G_\square^{re}/G_\square^i$
TTFDT	0.34	20 ± 4	1.7 ± 0.3
C8	0.14	1.0 ± 0.2	1.2 ± 0.6
OPVDT	0.65	2.2 ± 0.2	2.3 ± 0.3

Table 3.1: Comparison of the sheet conductance for devices with different molecules during oxidation and reduction. $G_\square^i$ corresponds to the averaged sheet conductance measured after molecular place–exchange, in the case of the TTFDT and the OPVDT, or directly after stamping, in the case of the C8. $G_\square^{ox}$ and $G_\square^{re}$ correspond to the average conductance measured after oxidation and reduction, respectively. Note that the second and third column indicate a conductance ratio, namely, the conductance after oxidation and reduction normalised with the initial conductance, respectively.

We have shown that the conductance of the nanoparticle array devices can be influenced by the oxidation state of the molecules in the array. In the following section we introduce two models to help us understand the physics behind the change in conductance.

3.5 Understanding the changes in conductance

To understand the origin of the conductance changes due to the changes in the oxidation state of the TTFDT molecules in the array we look at two models.

In the devices containing the TTFDT molecule an increase of about one order of magnitude was observed in the conductance after oxidation. To assess this observed change in conductance, we first consider a commonly used single–step tunnelling model for the transport through the molecular junction, Figure 3.7(a). The conductance can be written as:

$$G = G_C \exp\left(-2d\sqrt{2\Phi m}/\hbar\right) \tag{3.1}$$

Where G_C is the contact conductance determined by the coupling to the electrodes, Φ is the barrier height ($E_{HL}/2$), d is the length of the molecule, $m = 9.1 \times 10^{-31}$ kg is the electron mass, and $\hbar = 1.05 \times 10^{-34}$ J·s is the reduced Planck constant. The barrier will be taken as the half of the energy gap between the highest occupied molecular orbital (HOMO) and the lowest unoccupied molecular orbital (LUMO). This is a crude approximation since we can expect that one of the molecular orbitals, normally the HOMO, will lie closer to the Fermi energy of the Au electrodes than the other. This approximation also assumes that the molecule has some mean effective barrier while in reality the HOMO–LUMO gap E_{HL} will be different in the TTF center of the molecule than it is in the alkane chains on each side.

Given the presence of the alkane spacers between the TTF center and the –SH binding group we do not expect substantial charge transfer between the Au nanoparticles and the molecule. We therefore anticipate that the molecular orbitals

of the TTF are only weakly affected by the Au terminals. Therefore, we assume that the Fermi level of the Au terminals lies in the middle of the HOMO–LUMO gap in a symmetric junction at equilibrium. Deviations of the order $k_B T / E_{HL}$ can be expected depending on the degeneracy of the HOMO and LUMO levels. When the molecule is brought into the dication state, the molecular orbitals are again filled and the π system is globally neutral. The situation is therefore analogous to the neutral case, and the Fermi level is also expected to lie approximately in the middle of the HOMO–LUMO gap.

The HOMO–LUMO gap of the TTFDT in the dication state was determined from the UV–Vis absorption spectrum shown in Figure 3.2. The spectrum shows a strong absorption peak around 550 nm which reflects a HOMO–LUMO transition. The onset around 700 nm gives an estimate of the optical HOMO–LUMO gap. In the neutral case the optical transition does not correspond to the HOMO–LUMO gap. Therefore, we have to use values from time–dependent density functional theory (TD–DFT) calculations to obtain the HOMO–LUMO gap [3]. Overall, the values obtained for the HOMO–LUMO gap of the molecule are $E_{HL} = 3.7$ eV for the neutral TTF and $E_{HL} = 1.8$ eV for the molecule in the dication state. Using $d = 2.2$ nm as the length of the molecule we calculate the conductance ratio:

$$G_{TTFDT^{+2}}/G_{TTFDT} \quad = \quad \exp\left(\frac{-2d\sqrt{2m}}{\hbar} \cdot \left(\sqrt{\Phi^{+2}} - \sqrt{\Phi}\right)\right) \qquad (3.2)$$

$$G_{TTFDT^{+2}}/G_{TTFDT} \quad \simeq \quad 1.1 \times 10^4$$

Where Φ^{+2} and Φ are the barrier heights of the TTFDT^{+2} and TTFDT, respectively. ChemDraw 3D was used to calculate the length of the molecule by minimising its energy using the MM2 force field and measuring the distance between the two terminal sulphur atoms.

The estimate of the conductance change given by this simple tunnelling model is almost three orders of magnitude larger than the measured change ($\simeq 20$). There are several reasons why this might happen. An obvious reason for the discrepancy is the approximation of the effective tunnelling barrier height is simplistic. Furthermore, it does not take into account any possible charging effect and reorganisation of the molecular orbitals upon contacting the Au electrodes. The estimate given by this model can be looked at as an upper limit of the conductance change after oxidation of the TTFDT.

A two step tunnelling model would be more appropriate to describe the process in this system. In fact, the alkane linkers were added to the TTF center to reduce the coupling between the TTF and the electrodes. A HOMO–LUMO gap of about 7 eV can be expected for short alkane chains [60]. This decoupling is essential to ensure stable oxidation and reduction of the molecule. Such a configuration suggest that a resonant tunnelling model is more appropriate to describe the process, Figure 3.7(b).

The TTF center plays the role of a weakly coupled quantum dot and the
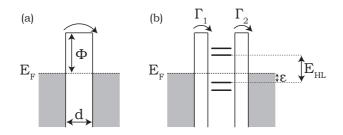
Figure 3.7: A schematic showing two tunnelling processes. (a) A simple one step tunnelling process where an electron tunnels from the left to the right electrodes. The molecule, between the electrodes, is treated as a tunnelling barrier. Here Φ is the barrier height and d the distance between the electrodes. (b) A two step tunnelling process. An electron tunnels from the left electrode through a large barrier onto the molecule and then again through a large barrier onto the right electrode. The tunnelling rates through the barriers are indicated by Γ_1 and Γ_2, and ε is the energy difference from the closes molecular orbital and the Fermi level of the electrodes.

alkane chains act as large barriers. At low bias voltages, the conductance can be approximated by:

$$G = \frac{2e^2}{h} \frac{\Gamma_1 \Gamma_2}{\varepsilon^2 + (\Gamma_1 + \Gamma_2)^2/4} \qquad (3.3)$$

Where Γ_1 and Γ_2 are the electronic coupling between the molecule and the left and right electrodes, respectively, ε is the energy difference between the closest molecular orbital and the Fermi level of the reservoirs, e is the charge of an electron, and h the Planck constant. Since the molecule is symmetric we assume $\Gamma_1 = \Gamma_2 = \Gamma$. In the weak coupling limit $\Gamma \ll \varepsilon$. The weak coupling approximation can be justified by the presence of the alkane linkers. In a similar study on an asymmetric C_{60}–based system with a slightly different but comparable linker, a coupling constant $\Gamma \lesssim 5$ meV was found[23]. The change in conductance can be expressed as:

$$
\begin{aligned}
G_{\text{TTFDT}^{+2}}/G_{\text{TTFDT}} &= \left(\frac{\varepsilon_{\text{TTFDT}}}{\varepsilon_{\text{TTFDT}^{+2}}} \right)^2 \\
G_{\text{TTFDT}^{+2}}/G_{\text{TTFDT}} &\simeq 4.2
\end{aligned}
\qquad (3.4)
$$

This second estimate is about a factor of 5 lower than the observed change in conductance. This model is an oversimplification since the distance between the Fermi energy and the closest orbital relevant for transport might not by simply a fraction of E_{HL}. This model does not take into account any charging effects or energy level broadening. While phenomenological, the above estimates remain reasonable and provide an upper and a lower bound to the conductance ratio expected in the measurement.
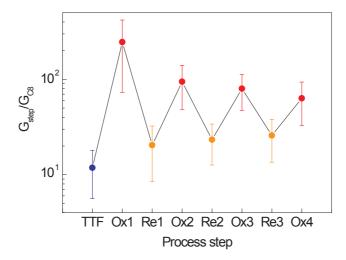
Figure 3.8: The device conductance normalised with the conductance of the devices before TTF molecular place–exchange averaged over the 20 devices measured as a function of redox step, TTF (●), after oxidation (●), and after reduction (●). The switching amplitude decays with the number of repetitions. This might be caused by the breaking of Au–S bonds between the TTFDT and the nanoparticles by the oxidant and the coordination of the unbound end groups with iron ions from the oxidant. There is also a possibility of the formation of dimers and oligomers via disulphide bond formation during the redox cycles.
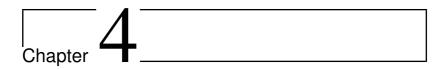
To examine the reversibility of the conductance change upon exposure to the oxidant and reductant, we repeated the redox process several times. Figure 3.8 shows the average ratio $G_{\square\ TTFDT}/G_{\square\ C8}$ of 24 devices at different stages during four oxidation–reduction cycles. The red points correspond to the oxidised, dication, state while the orange pints correspond to the neutral state. The data demonstrates that the conductance of the devices can be reproducibly switched between a high conductance level, after oxidation, and a low conductance level, after reduction. Note that the switching amplitude decays with the number of repetitions. This might be caused by the breaking of Au–S bonds between the TTFDT molecule and the nanoparticles by the oxidant and the coordination of the unbound end groups with iron ions of the oxidant. We also cannot exclude the formation of dimers or oligomers via disulphide bond formation during the redox cycles. Such effects will result in a lower maximum conductance and a higher minimum conductance.

3.6 Summary

We have successfully inserted molecules with tetrathiafulvalene redox units into two–dimensional nanoparticle arrays to form functional networks of molecular junctions. The conductance of the networks could be repeatedly switched between a high conductance level and a low conductance level by means of chemical oxidation and reduction. The change in conductance arises from the reorganisation of the TTFDT molecular orbitals upon oxidation, as supported by UV–Vis spectroscopy. The high– and low–conductance states are stable enough to permit electrical characterisation after each oxidation and reduction step. Our experiments not only demonstrate the efficient modulation of the conductance of molecular junctions by up to one order of magnitude but also raise interesting prospectives for chemical sensing based on networks of active molecular junctions.

Part II

Non–linear transport through nanoparticle arrays

Chapter 4
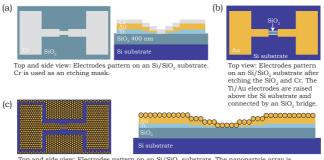
Reducing the size of nanoparticle arrays

4.1 Introduction

In Part I we introduced the nanoparticle arrays as a platform for molecular electronics. One could think of them like the breadboards used to design and test electronic circuits. Instead of resistors and capacitors inserted into the breadboard, molecules can be inserted into the arrays to bridge the nanoparticles. Furthermore, we discussed how the conductance of the arrays was influenced not only by the molecules used to bridge the nanoparticles, but also the oxidation state of those molecules.

In order to access non–linear IV characteristics of the devices it is important to be able to apply large voltages over each molecular junction. Furthermore, applying large bias voltages over the molecular junctions enables us to investigate the contribution of inelastic tunnelling through them. The bias voltages applied to the arrays in Part I were on the order of ± 10 V. Assuming that the applied voltage drops evenly over each molecular junction in series, the voltage drop over each molecular junction is only on the order of 10 mV. The devices described in Section 2.3 are relatively large, ~ $10 \times 20 \ \mu m^2$ in size containing ~ 1000×2000 molecular junctions in series and parallel. To investigate the transport through the nanoparticle arrays in more detail, it is necessary to fabricate smaller arrays. Using PDMS stamps to make small structures is not feasible, PDMS is not rigid enough to support narrow high aspect ratio structures. Using the procedure described in Section 2.3, it is impossible to bring the metal electrodes closer to each other than a few micrometers. Therefore, a new method had to be devised to fabricate nanoparticle arrays with dimensions on the order of hundreds of nanometers.

4.2 Fabrication of small nanoparticle arrays

(a) Top and side view: Electrodes pattern on an Si/SiO$_2$ substrate. Cr is used as an etching mask.

(b) Top view: Electrodes pattern on an Si/SiO$_2$ substrate after etching the SiO$_2$ and Cr. The Ti/Au electrodes are raised above the Si substrate and connected by an SiO$_2$ bridge.

(c) Top and side view: Electrodes pattern on an Si/SiO$_2$ substrate. The nanopartcie array is transferred on to the surface with an unpatterned PDMS stamp. The structured electrodes on top of the SiO$_2$ and the SiO$_2$ area between the electrodes define a device. The 8 nm high steps in the electrode height ensure that the nanoparticle array is continious over the whole device after stamping.

Figure 4.1: A schematic showing the structure of devices with small nanoparticle arrays. (a) A top and a side view of the structure of the device on top of 400 nm thick SiO$_2$ after the two evaporation steps. The device structure is determined by the Cr etching mask. In the first evaporation step the Ti, Au, and the Cr on top of the Au are evaporated. The Ti and Au layers are evaporated at ± 7° and 0° angles from the normal of the substrate. The Cr layers are evaporated at ± 8° and 0° angles from the normal. This results in the thickness of the electrodes decreasing towards the center of the device. The Cr layer on the SiO$_2$ is evaporated in the second evaporation step at 0° angle from the normal of the substrate. This Cr layer defines the size of the nanoparticle array measured in the device. (b) The device after the SiO$_2$ and the Cr have been etched away. (c) A top and a side view of the device after stamping with the nanoparticle array. The array is deposited everywhere, but the 400 nm height difference between the device and the surrounding substrate ensures that the array on top of the device is not connected to the surrounding substrate. The height decrease in the electrodes, near the center of the device, ensures the continuity of the nanoparticle array over the whole device.

To make the small nanoparticle arrays Ti/Au electrodes were evaporated on top of a Si/SiO$_2$ substrate. The SiO$_2$ had a thickness of 400 nm, and the electrodes were 24 nm thick structured in a way to become gradually thinner towards the ends. The structure is shown in Figure 4.1 and described in details below. The electrodes were patterned using electron beam lithography, metal evaporation and etching.

First the electrode pattern was written into a PMMA–MA/PMMA layer with a thickness of 100 nm and 600 nm, respectively. The PMMA–MA layer provides a large undercut under the PMMA layer. Titanium (Ti) and gold (Au) layers were evaporated at three different angles, thus creating gradually decreasing electrode thickness towards the center of the device. The electrode metals were evaporated at ± 7°, and 0° angles from the normal of the substrate. The thickness of each Ti layer at

each angle was 3 nm, and the thickness of the three Au layers was 5 nm at each angle. This results in 8 nm high steps. After evaporating the Ti and the Au layers three 15 nm thick chromium (Cr) layers were evaporated on top of the Au at $\pm$ 8°, and 0° angles from the normal of the substrate. After lift off PMMA–MA and PMMA were again spun on the substrate and a second lithography step was performed. In the second lithography step lines were patterned on the substrate connecting the two electrodes. After development a 45 nm thick Cr layer was evaporated onto the substrate at a 0° angle from the substrate normal. This Cr layer covered the SiO_2 between the two electrodes.

After lift off the substrate was treated with O_2 and CHF_3 plasma to etch away the uncovered SiO_2. Then the Cr was etched away with a solution of ceric ammonium nitrate (CAN, $Ce(NH_4)_2(NO_3)_6$) in DI-H_2O and acetic acid (CH_3CO_2H). The resulting structure comprised of the electrodes on top of 400 nm thick SiO_2 bridged by a small SiO_2 area. The electrodes having a thickness of 9 nm Ti and 15 nm Au became gradually thinner, in steps of 8 nm, close to the SiO_2 bridge. The size of the SiO_2 bridge determined the size of the nanoparticle array in the device.

After fabrication, of the electrodes, the samples were soldered to a chip carrier using flux free solder. This provided the possibility of performing molecular place–exchange on the samples in organic solvents without having unwanted organic molecules influencing the exchange.

Using un–patterned PDMS stamps Au nanoparticle arrays were stamped on top of the substrate. The 400 nm height difference between the electrodes and the surrounding Si substrate caused the nanopartice array on the electrodes to be disjoint from the surrounding nanoparticle array while the 8 nm step towards the SiO_2 bridge allowed the array to be continuous over the whole device, the two electrodes and the SiO_2 bridge between them. The result were well defined nanoparticle arrays with a length of 200–500 nm and width of 200–1000 nm contacted by two metal electrodes.

After stamping the electrodes were connected to the contacts of the chip carrier using Au wire wedge bonding. The substrate was also connected to a contact pad on the chip carrier using Al wire wedge bonding. This allowed the substrate to be grounded during measurements.

Figure 4.2 shows images of an actual sample. Figure 4.2 (a) is an optical image of a sample in a chip carrier after stamping with a nanoparticle array and bonding. The chip carrier is 1 cm^2. The sample is fixed into the chip carrier by soldering. Figure 4.2 (b) is an SEM image of the sample, showing the device contact pads surrounding the devices, which reside in the center. Figures 4.2 (c) shows a closer look of three devices in the center. The leads come in from left and right to each device. A nanoparticle array has been stamped on top of the sample in the figure. The figures is taken at a 70° angle from the normal to the substrate. It shows the raised structure of the electrodes and how the nanoparticle arrays on top of the electrodes are not connected to the nanoparticle arrays deposited on the Si substrate around the leads. Figure 4.2 (d) shows a close up of a device before the deposition of the nanoparticle
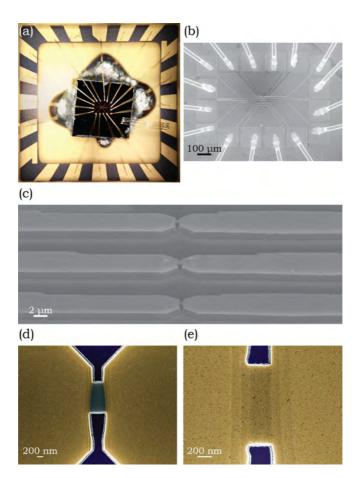
Figure 4.2: (a) A photo of a bonded sample in a chip carrier taken by an optical microscope. The sample is soldered in the chip carrier to mechanically fix it. The contacts of the devices are bonded with an Au wire to the contacts of the chip carrier. (b) An SEM image of the sample. The scale bar is 100 μm. (c) A closer look at the devices taken by an SEM at 70° angle from the normal of the surface. The image shows the raised structure of the electrodes. The scale bar is 2 μm. (d) A close up of a device before the nanoparticle array was stamped on it. The yellow areas represent the Au electrodes. The light blue area in the center is the SiO_2 where the nanoparticle array will we deposited later. On each side of the SiO_2 one can see the steps in the Au electrodes. The dark areas above and below the SiO_2 in the figure are the exposed Si substrate. The scale bar is 200 nm. (e) A close up of a device, after the nanoparticle array has been stamped on it, taken by an SEM. The figure shows that the nanoparticle array is continuous over the whole device. The colours are the same as in Figure (d) and were added by Adobe Photoshop CS. The scale bar is 200 nm.

array. The two Au electrodes, yellow, are separated by a SiO_2 bridge shown in a light blue color in the center of the image. The dark areas above and below the SiO_2 bridge are the Si substrate. Towards the SiO_2 bridge one can see the steps in the Au electrodes. Figure 4.2 (e) shows a device after the deposition of the nanoparticle array. The figure shows clearly that the nanoparticle array is continuous over the device. Furthermore, it shows that no nanoparticles are deposited on the Si substrate next to the device. In Figures 4.2 (d)–(e) the color was added using Adobe Photoshop CS.

4.3 Transport measurements at low temperature

The transport properties of the devices were measured using the set up shown in Figure 4.3. The sample, already placed in a ceramic chip carrier, was inserted into a socket at the end of a dipstick. The socket of the dipstick was wired to a break out box, on top of the dipstick, with a ribbon of 12 twisted pair wires. The sample devices were connected in such a way that one wire in a twisted pair was connected to one side of the device and one wire in another twisted pair was connected to the other side of the devices. Normally wires from the first twisted pair were used with wires from the seventh twisted pair, wires from the second with wires from the eighth and so on. While measuring, all wires of all the twisted pairs are grounded, except for the two wires needed for the measurement. This spatial separation of the wires used, and the grounding of all other wires decreased the capacitive cross talk between the measurement lines.

The dipstick was characterised by measuring a 10 GΩ resistor that was soldered to a chip carrier and inserted into it. The measurements were done at room temperature. The differential conductance of the resistor in the dipstick was measured while the frequency of the applied ac voltage was varied from 11 Hz to 11 kHz, the dc bias was at 0 V during the measurement. From the frequency sweep we calculated the leakage capacitance to ground in the dipstick to be ~ 2 pF. The IV, dI/dV, and d^2I/dV^2 were also measured using the 10 GΩ resistor. The frequency of the ac voltage was 73 Hz. The measurement data are to be found in Appendix E.

The measurements were controlled with a LabView program on a PC. The program was used to control a Yokogawa YK7651 dc voltage source and two Stanford Research SR830 lock–in amplifiers, one set to detect the first harmonic of the ac signal and the other to detect the second harmonic of the signal. The resulting current was detected using a DL Instruments DL1212 IV converter. The dc part of the signal was measured on a National Instruments data acquisition board (NI–DAQ). The ac part of the signal was measured by the two lock–in amplifiers and their output passed on to the data acquisition board and the PC.

When performing the measurement a small ac voltage signal was added on top of a dc voltage signal via a NLT1 1:1 transformer. The dc voltage is supplied by
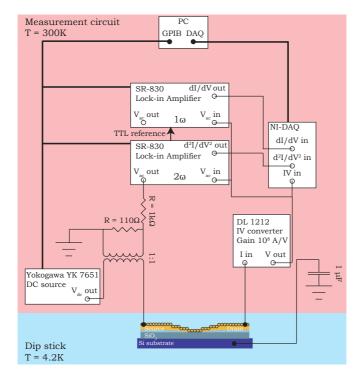
Figure 4.3: A schematic showing the measurement set up used to measure the electrical transport in small nanoparticle arrays at 4.2 K. An SR 830 lock–in amplifier supplies an ac voltage. The amplitude of the ac voltage is attenuated by a factor of 1/10 by a voltage divider before the signal goes through an NTL1 1:1 transformer. An Yokogawa YK651 dc voltage source is connected to the secondary coil in the transformer. The resulting signal from the secondary coil of the transformer is an ac voltage on top of a dc voltage. This signal is applied to the source contact of the measured device. The drain of the device is connected to a DL 1212 IV converter. The output of the IV converter is measured directly by a NI–DAQ board and two SR830 lock–in amplifiers. The NI–DAQ board measures the dc response of the device. The lock–in amplifiers measure the first and second harmonics of the ac response of the device, which are proportional to the dI/dV and the d^2I/dV^2 of the device, respectively. The substrate is grounded via an 1 μF capacitor. This capacitor is ~6 orders of magnitude large than the capacitance between the metal contacts on the device and the substrate. This shorts the ac current that runs in the substrate to ground, but allows a dc charge to build up in the substrate thus reducing the dc voltage drop from the device contacts to the substrate.

the Yokogawa voltage source. The ac voltage was supplied by one of the lock–in amplifiers. A large ac signal was passed through a voltage divider to decrease its amplitude without inducing digitisation error in the signal. The lock–in amplifiers were synchronised using the TTL signal from the amplifier set to detect the second harmonic of the ac signal. This lock–in amplifier also supplied the ac signal.

The capacitance between the device electrodes and the substrate is $C = A\epsilon_0\epsilon_r/d$ with $A \sim 150 \times 150 \ \mu\text{m}^2$, $d = 400$ nm, ϵ_0 is the permittivity of vacuum, and $\epsilon_r = 3.9$ for SiO_2. The capacitance is $C = 1.9 \times 10^{-12}$ F. The substrate was grounded through an 1 μF capacitor. This capacitor is about six orders of magnitude larger than the capacitance between the device electrodes and the substrate. An ac signal is thus effectively grounded while any dc charging in the substrate is not grounded. This reduces the dc voltage drop from a device contact to the substrate over the oxide and thus reduces the probability of the oxide breaking down under high dc bias.

The current flowing in the device is comprised of an ac part and a dc part and can be expressed by a Taylor series to second order as

$$
\begin{aligned}
I(V_{\text{dc}} + V_{\text{ac}}\sin(\omega t)) \quad = \quad & I(V_{\text{dc}}) + \frac{dI(V_{\text{dc}})}{dV} V_{\text{ac}}\sin(\omega t) + \\
& + \frac{1}{4}\frac{d^2 I(V_{\text{dc}})}{dV^2} V_{\text{ac}}^2 \left(\cos(2\omega t + \pi) + 1\right) \quad (4.1)
\end{aligned}
$$

For details on the calculation see Appendix F.

Chapter 5

Characterisation of the nanoparticles in the arrays

5.1 Introduction

The transport through arrays of nanoparticles is governed by several competing energy scales. Regarding the nanoparticles, their charging energy and the tunnelling conductance between them are important [7]. These energy scales can be adjusted by tuning the size of the nanoparticles, the interparticle spacing, and the interparticle coupling. The interparticle spacing and coupling can be adjusted by the molecules surrounding the nanoparticles. Having perfect control over these parameters would open up a large range of possible devices where the device function would be determined by the properties of the nanoparticle arrays. Metallic nanoparticles can be viewed as artificial atoms and therefore arrays of nanoparticles could be engineered into artificial solids with tunable electronic and optical properties [7].

The nanoparticles form the basis of the nanoparticle array, therefore it is important to understand their contribution to the transport in the arrays. The transport through arrays of metallic nanoparticles has been studied experimentally [78]. The questions we strive to answer concern the detailed transport through the molecules bridging the nanoparticles. Understanding the contribution of the nanoparticles in the transport is the first step towards understanding the transport through the molecules in the array.

In this chapter, we investigate what the contribution of the nanoparticles to the transport in the arrays is and what role disorder of the arrays plays in the transport.
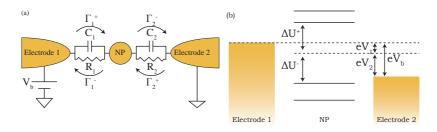
Figure 5.1: The generic model of transport through two tunnel junctions connected in series. The model is comprised of a nanoparticle contacted to two electrodes via an *RC* circuit. Figure (a) shows a RC model of the tunnel junctions. The nanoparticle is coupled to the two electrodes via capacitors C_j and resistors R_j, where j is the junction number. The tunnelling rates onto and of the nanoparticle are indicated by Γ_j^+, and Γ_j^-, respectively. Electrode 1 is at bias V_b and Electrode 2 is at ground. Figure (b) shows the energy scales relevant to transport through the junction. The change in energy when a single charge is added (+) or removed (-) is indicated by $\Delta U^{\pm}$. The total potential difference between the electrodes is V_b.

5.2 Coulomb blockade in a double junction

The nanoparticles forming the arrays are quite small. They have a radius of 5 nm and are small enough so that a charge moving onto or off the nanoparticle will feel the force of the charges which are already on it. This gives rise to a voltage dependent impedance in the array. This phenomenon is the single–electron charging of the nanoparticle. When an electron tunnels onto or off the nanoparticle its charge changes. The energy required to charge the nanoparticle must be supplied from the environment, either thermally or from the external applied bias. This is known as Coulomb blockade and gives rise to the nanoparticle charging energy [78].

A simple model has been set forward to describe the transport through a nanoparticle in the single–electron charging regime [2, 24]. The model describes the transport through a series of two tunnel junctions. A schematic of the system is shown in Figure 5.1. We start by introducing this model and later build on it when the transport through an array of nanoparticles is characterised.

The transport through the model system will be governed by the energy needed to add or remove charge to/from the nanoparticle. This charging energy of the metallic nanoparticle is calculated as [40]

$$E_c = \frac{e^2}{2C}, \tag{5.1}$$

where e is the elemental charge of an electron and C the capacitance of the

nanoparticle. The capacitance of a single spherical nanoparticle is

$$C = 4\pi\epsilon_0\epsilon_r R, \tag{5.2}$$

where ϵ_0 is the permittivity of free space, ϵ_r the dielectric constant, and R the particle radius. The change in charging energy of the nanoparticle when a single charge is added (+) or removed (-) is calculated as

$$\Delta U^\pm = \frac{(Q \pm e)^2}{2C_\Sigma} - \frac{Q^2}{2C_\Sigma}, \tag{5.3}$$

where $C_\Sigma = C_1 + C_2$ is the sum of the capacitances in Figure 5.1 and Q is the charge on the nanoparticle. The change in the energy of the whole system when an electron tunnels on (+) or off (−) the nanoparticle through junction 1 (ΔE_1) or junction 2 (ΔE_1) is

$$\Delta E_1^\pm = \Delta U^\pm \mp e\frac{C_2}{C_\Sigma}V_b,$$

$$\Delta E_2^\pm = \Delta U^\pm \pm e\frac{C_1}{C_\Sigma}V_b, \tag{5.4}$$

where V_b is the potential difference between the two electrodes. The first term in the equation is the change in the electrostatic energy of the nanopartice $\Delta U^\pm$ as defined in Equation 5.3. The second term in the equation is the work done by the voltage source while the electron tunnels over the junction j. The voltage drop over each junction in Figure 5.1 is

$$V_j = \frac{C_1 C_2}{C_j C_\Sigma}V_b. \tag{5.5}$$

The tunnelling rate is controlled by the resistors in Figure 5.1

$$\Gamma_j^\pm = \frac{1}{e^2 R_j}\frac{-\Delta E_j^\pm}{1 - \exp\left(\Delta E_j^\pm/k_B T\right)}. \tag{5.6}$$

At $T = 0$ K, Equation 5.6 can be simplified as

$$\Gamma_j^\pm(T = 0\text{K}) = \begin{cases} -\Delta E_j^\pm/e^2 R_j, & \Delta E_j^\pm < 0, \\ 0, & \Delta E_j^\pm \geq 0, \end{cases} \tag{5.7}$$

using the condition for conductance, $\Delta E_j^\pm < 0$, from Equation 5.7 and inserting the value of $\Delta E_j^\pm$ from Equation 5.4 into it gives

$$\Delta U^\pm \mp e\frac{C_j}{C_\Sigma}|V_b| < 0, \tag{5.8}$$

assuming $C_1 = C_2$. Taking the initial charge on the nanoparticle to be zero, $Q = 0$, and inserting the value of $\Delta U^{\pm}$ from Equation 5.3 into Equation 5.8

$$\frac{e^2}{2C_\Sigma} \mp e\frac{1}{2}|V_b| \quad < \quad 0. \tag{5.9}$$

Inserting Equation 5.1 into Equation 5.9 and rearranging the terms gives the threshold voltage for conductance

$$|V_{CB}| \quad = \quad 2E_C/e. \tag{5.10}$$

The current through the double junction is determined by the difference in the tunnelling rates on to and off the nanoparticle

$$I = e\left(\Gamma_1^+ - \Gamma_1^-\right) = -e\left(\Gamma_2^+ - \Gamma_2^-\right). \tag{5.11}$$

Combining equations 5.7 and 5.11 the current flowing through the double junction is

$$I = \begin{cases} \dfrac{V_b - |V_{CB}|}{2R} & V_b > |V_{CB}|, \\[2mm] 0 & -|V_{CB}| < V_b < |V_{CB}|, \\[2mm] \dfrac{V_b + |V_{CB}|}{2R} & V_b < -|V_{CB}|. \end{cases} \tag{5.12}$$
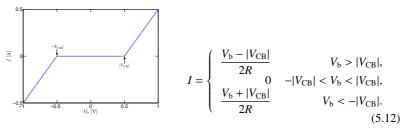
Figure 5.2: The *IV* curve calculated by Equation 5.12 with $|V_{CB}| = 0.5$ and $R = 1\ \Omega$.

5.3 From a double junction to an array of junctions

The double junction model introduced in Section 5.2 captures the dynamics of transport through a single nanoparticle between two electrodes. The devices we measure contain many nanoparticles, in series and parallel, between two electrodes. The problem we face is how to understand the role of Coulomb blockade in such arrays. One way to use the model in Section 5.2 to model the junctions in the arrays is to see if we can treat the array as a simple parallel and series connection of junctions. Can we estimate the voltage drop over each junction by dividing the total voltage by the number of junctions in series and can we estimate the current through each junction by dividing the total current measured by the junctions in parallel? Mapping this in details would be an interesting measurement requiring high resolution Kelvin
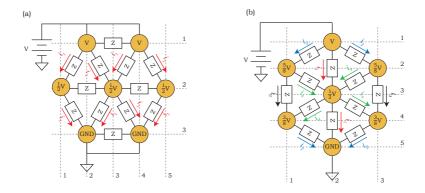
Figure 5.3: Schematics of hexagonal impedance networks. Metallic electrodes (yellow circles) are connected via an impedance Z. A voltage V_b is applied to the topmost electrode while the bottommost electrode is kept at ground potential. The proportional voltage at each electrode is indicated in each yellow circle. The currents flowing in the circuit are shown with color coded arrows. Each color represents the magnitude of the current, currents with the same color have the same magnitude. Here two cases are shown: (a) The side–to–side case when two electrodes are connected to the bias source and another two to the ground. The voltages at each electrode can be readily obtained. The same current flows through each impedance going from top to bottom and thus the same voltage drops over each of them. There is no voltage drop over the impedances going from left to right and no current flows there. (b) The head–to–tail case when only one electrode is connected to the bias source and another electrode to the ground. The head–to–tail case is comprised of the same hexagonal unit as the side–to–side case, but rotated by 30°. The head–to–tail case is more complex to solve, than the side–to–side case, and the voltages at each electrode cannot practically be calculated analytically for large arrays.

probe force microscopy (KPFM). This is beyond the scope of this work. Although, in a collaboration with Thilo Glatzel and Marcin Kisiel, in the group of Ernst Meyer at Basel University, we have started looking at the arrays with a KPFM. An overview of preliminary measurements is in Appendix B. To gain some insight into the voltage drops over the junctions in the arrays we have made simple models using linear circuit elements.

5.3.1 An impedance network model of the nanoparticle array

In a first attempt to investigate how voltages drop and how currents flow in the array we start by looking at what happens in a single hexagonal unit comprising of a central nanoparticle surrounded by six nanoparticles. Figure 5.3 shows a schematic of an electrical circuit where metal electrodes, yellow circles, are connected with impedances Z. A potential V_b is applied to the top electrode while the bottom electrode is kept at ground potential. The voltage at each nanoparticle is indicated inside it, as a fraction of the applied voltage. The figure shows two cases: The side–

to–side case, has two electrodes connected to the voltage source and two connected to the ground and the head–to–tail case, where only a single nanoparticle is connected to the voltage source and a single nanoparticle is connected to the ground. The two cases consist of the same hexagonal unit, but rotated by 30°.

Due to symmetry in the side–to–side case the same voltage drops over each impedance going from top to bottom, while no voltage drops over the impedances going from left to right. Thus, the voltage drop over each impedance scales as the number of lines of nanoparticles, $V_{\text{jnct}} = V_{\text{b}}/(N-1)$, where N is the number of lines of nanoparticles. This can be related to the voltage drop over each molecular junction in the nanoparticle array assuming each molecular junction has an impedance Z. In the case when the measured array is monocrystalline with the side–to–side orientation the voltage drop per molecular junction scales as

$$V_{\text{jnct}} \quad = \quad V_{\text{b}} \frac{h}{L}, \tag{5.13}$$

where $L = h(N - 1)$ is the distance between the electrodes connected to the array, $h = d\sqrt{3}/2$, d is the distance from center to center of the nanoparticles, and V_{b} is the voltage applied to the electrodes connected to the array.

The current in the array scales with the array width. The arrays are assumed to be a monolayer so the thickness is not a factor. The linear current density in the array is defined as the current flowing in each current path. In the side–to–side configuration the current scales with the number of vertical columns as

$$I_{\text{dens}} \quad = \quad I_{\text{total}} \frac{d}{W}, \tag{5.14}$$

where $W = d(M - 1)$ is the width of the array, d is distance from center to center of the nanoparticles, M is the number of columns, and I_{total} is the total current flowing in the array.

In the head–to–tail case the voltage drop over each impedance is not always identical. Solving for the voltages at each nanoparticle analytically is not practical for large arrays. To investigate the influence of scaling the array we used PSpice Student version Release 9 by OrCAD to calculate the voltages of nodes, representing the nanoparticles, connected by identical resistors in the head–to–tail formation. Figure 5.4 shows the results of the simulation for: (a) The basic hexagonal unit, seven nanoparticles the center one connected to the outer six; (b) A narrow array with three hexagonal units in series; (c) An array with two hexagonal units in series and a two hexagonal in parallel; (d) The generic array. The color of the nanoparticles, circles, indicates their potential. Red indicates that the nanoparticle is at the highest potential, equal to V_{b}, and white indicates that the node is at ground potential, shades in between red and white indicate intermediate potentials. The lines connecting the circles represent the potential difference between two neighbouring nanoparticles, the voltage drop over a resistor in this model. The blue color indicates the highest
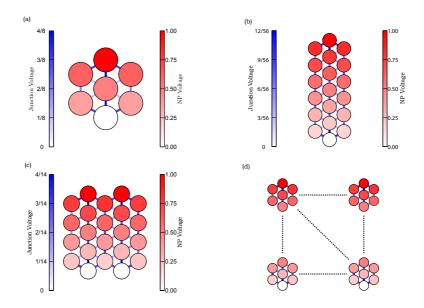
Figure 5.4: A Spice simulation of metallic electrodes connected by identical resistors. The electrodes are arranged as the nanoparticles in the nanoparticle array in the head–tail case. (a) The smallest unit containing a full hexagon. (b) Three hexagonal units in series. (c) Two hexagonal units in series and two in parallel. (d) A representation of the generic array. The color of the circles indicates their voltage with red representing 100% of the applied voltage and white the ground potential. The color of the lines connecting the circles indicates the voltage drop over each resistor. Here the blue color indicates the largest voltage drop over the resistor. The fraction of the applied voltage dropping over each resistor is indicated on the blue color bar. The voltage per junction decreases as the number of electrodes in series increases. The rate of the decrease is shown in Figure 5.5. The voltage drop per junction does not change significantly as more junctions are added in parallel.

voltage drop over a resistor in the model array and white indicates no voltage drop over the resistor. The most prominent lines in the figure imply the highest voltage drop between the nanoparticles. The blue color bar indicates the fraction of the applied bias voltage that drops over the resistor. Looking at the scale by the blue color bar one can see how the maximum voltage drop decreases when the units are connected in series. Connecting the units in parallel does not change the voltage drop over the resistors. Figure 5.5 shows how the inverse of the voltage drop over each resistor scales with the number of lines of nanoparticles in the array. The red circles are values calculated using Equation 5.13, and the blue circles were obtained from the Spice simulations. The dotted lines are guides for the eye. The insets in the figure show the orientation of the hexagonal unit with red showing the side–to–side case
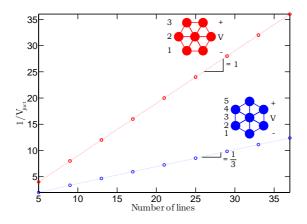
Figure 5.5: The inverse of the voltage drop per junction in the nanoparticle array as a function of the number of lines in the array. In the side–to–side case, red circles, the voltage drop per junction decreases linearly with the increase in the number of lines. The values plotted in the figure are calculated using Equation 5.13. In the head–to–tail configuration, blue circles, the voltage drop per junction decreases with the increasing number of lines in the array with a factor of 3. The data plotted in the figure was obtained by the Spice simulation.

and blue showing the head–to–tail case, as well as the slope of the lines.

As shown in Eq. 5.13 the voltage over each junction in the side–to–side case decreases as $1/(N-1)$. In the head–to–tail case the voltage over each junction decreases as $3/N$, so the voltage drop over each junction as a function of the distance between the electrodes is then

$$V_{\text{jnct}} \quad = \quad V_{\text{b}}\frac{d}{L}, \tag{5.15}$$

where $L = d(N-1)$.

The number of current paths scales as the number of vertical columns of nanoparticles. The current density can be estimated as

$$I_{\text{dens}} \quad = \quad I_{\text{total}}\frac{h}{W}, \tag{5.16}$$

where $W = h(M-1)$ is the width of the array, h is as defined in Eq. 5.13, and I_{total} is the total current flowing in the array.

In reality the nanoparticle array bridging two electrodes is neither perfectly in the head–to–tail nor the side–to–side configuration. Moreover, the array has some variations in the impedance of each molecular junction due to the size distribution of

the nanoparticles and defects in the array. The array is also never monocrystalline between the electrodes and the effect of grain boundaries on the transport of the array is not known. In this thesis we assume $L \gg d, h$ and normalise the applied voltage by d/L to obtain the voltage drop over each junction. Furthermore, Middleton and Wingreen [47] showed that, in a two dimensional array of capacitively coupled normal–metal dots arranged in a square lattice, the onset of conduction occurs at a voltage V_{th} proportional to the linear array size. Tran et al. [67] report that the bias per junction and the bias applied across a short stack of N particles is $V_{jnct} = V_{total}/N$.

As with the voltage scaling the linear current density will not scale exactly as described in Equations 5.14 and 5.16. From now on the total current will be scaled by d/W to find the linear current density, assuming $W \gg d, h$. As a consequence of this, scaling, the sheet conductance of the devices is found by scaling the measured conductance by L/W, and the second derivative of the current–voltage response is scaled by L^2/W to remove the influence of the array geometry from the signal.

5.3.2 Models describing the transport through arrays of nanoparticles linked by tunnel barriers

Modelling the nanoparticle array as nodes connected by resistors is useful to learn how to calculate the voltage drop over, and the current through, a single junction. This model does not take into account the properties of the nanoparticles introduced in the tunnelling model in Section 5.2. The transport through an array of nanoparticles coupled via tunnelling junctions has been studied by several groups. Here we look more into the details of those models.

The first thing to consider is how the charging energy of a nanoparticle changes when the particle is placed in an array of many nanoparticles which can interact with each other. The charging energy of the nanoparticle in the array depends on the inter–nanoparticle coupling, since a charge on one nanoparticle can polarize its neighbouring nanoparticles. The capacitance of the nanoparticles in the array can be approximated by assuming that the nanoparticle is separated from a conducting continuum by an insulating shell. The nanoparticle capacitance can then be calculated as [78]

$$ C = 4\pi\epsilon_0\epsilon_r \frac{R(R + s)}{s} \tag{5.17} $$

where s is the interparticle separation. This in turn affects the charging energy E_c calculated in Equation 5.1 and thus the threshold to over come Coulomb blockade calculated in Equation 5.10.

The effective capacitance of the nanoparticles is not enough to model a whole array. Effects of random charges on the nanoparticles and meandering current paths in two dimensions need to be considered. Elaborating on the double junction model Middleton and Wingreen [47] describe the collective transport in arrays of small

metallic dots. They define their array as capacitively coupled, via tunnel junctions, metallic dots in one or two dimensions. The onset of conduction is found to occur at a voltage V_{th} proportional to the linear array size. The current at voltages above V_{th} in linear and square arrays is found to behave as

$$I \quad \sim \quad (V_b/V_{th} - 1)^\zeta \qquad (5.18)$$

Figure 5.6 shows the shape of the current calculated by Equation 5.18 using the parameters $V_{th} = 0.5$ and $\zeta = 5/3$. There are two characteristic parameters in the model namely the threshold voltage V_{th} and the exponent ζ. We will now discuss the two parameters, starting with the threshold voltage.

Figure 5.6: The *IV* curve calculated by Equation 5.18 with $|V_t| = 0.5$ and $\zeta = 5/3$.

The threshold voltage in Equation 5.18 is closely related to $|V_{CB}|$ in equation 5.10. Parthasarathy et al. [52] look at how V_{th} scales in networks of metal nanoparticle arrays with random threshold voltages at each nanoparticle at finite temperatures. They assume that at a finite temperature T a fraction of the barriers, due to the nanoparticle charging energies, $p(T)$ can be overcome by thermal fluctuations. These junctions are assumed to behave as ohmic junctions. The fraction of barriers overcome by thermal fluctuations increases as T increases. When a certain fraction of the barriers can be overcome by the thermal fluctuations a conducting path is formed between the contacts. The fraction of barriers needed to be overcome is the percolation threshold of the array. The threshold voltage V_{th} for the conducting pathway is zero. In a two dimensional hexagonally close packed (hcp) array the threshold voltage is

$$V_{th} \quad = \quad V_{CB}N\left(1 - \frac{4.8k_B T}{p_c \bar{E}_C}\right) \qquad (5.19)$$
$$\text{with } p_c \quad = \quad 2\sin\left(\frac{\pi}{18}\right), \qquad \text{for an hcp array}$$

where N is the number of molecular junctions spanning the gap between the electrodes and $\bar{E}_c$ is the mean charging energy of the nanoparticles as calculated by Equation 5.1.

The other characteristic parameter of the model in Equation 5.18 is the exponent ζ. The exponent takes the values 1 and 5/3 for one and two dimensional square arrays, respectively [35, 47]. In recent work Šuvakov and Tadić [74] model the *IV* characteristic in two dimensional hexagonal arrays of nanoparticles. They find that the exponent ζ takes values of $\zeta \approx 2.5 - 2.8$ in weakly disordered hexagonally close packed arrays. When quenched charge disorder is added to the array the exponent

is reduced to $\zeta \approx 1.3$. In highly topologically disordered arrays the exponent takes higher values $\zeta \approx 3.9$.

In the following section we estimate the value of the threshold voltage and the exponent from our measured data.

5.4 Measurements of two dimensional nanoparticle arrays at low temperatures

The transport through several devices was measured. First we will look at the measurement results of a single device and see how to extract the threshold voltage V_{th} and the exponent ζ. From the threshold voltage we get information about the charging energy of the nanoparticles in the array, these values can be compared with theoretical values calculated using the equations presented above. Furthermore, the threshold voltage is useful to scale the measured data. By scaling the data, we see that the device fabrication and the measurement results are reproducible and the transport is not governed by size effects. Once the threshold voltage is known we can obtain the exponent ζ. This exponent gives information about the disorder in the arrays, this will be discussed below.

Before we look at the data we can calculate typical values of the parameters we expect in the measurements. The size of nanoparticles and interparticle spacing fabricated using the same protocol we use have been reported [9]. The nanoparticle radius was $R \approx 5$ nm, and the interparticle spacing $s \approx 2.5$ nm. The effective dielectric constant of the octane monothiol molecules (S–C8) covering the nanoparticles was reported as $\epsilon_r = 2.5$ [9].

Using Equation 5.2 and the values for R, s, and ϵ_r from above, the capacitance of a single nanoparticle is $C_{\text{NP}} = 1.4$ aF. Using Equations 5.1 and 5.10 one can calculate the charging energy of the nanoparticle $E_c = 57$ meV and the voltage needed to overcome the Coulomb blockade $V_{\text{CB}} = 115$ mV. When an array is composed of many such nanoparticles the effective capacitance of the nanoparticles scales as shown in Equation 5.17 and the capacitance takes the value $C^c_{\text{array}} = 4.2$ aF. The superscript c is used to indicate a calculated value. This changes the effective charging energy which becomes $E^c_c = 19$ meV and the voltage to overcome Coulomb blockade becomes $V_{\text{CB}} = 38$ mV. At finite temperatures electrons can overcome the Coulomb barrier by thermal excitations. Taking this into account the threshold voltage for conduction is scaled as shown in Equation 5.19 and becomes $V^c_{\text{th}} = 28$ mV at a temperature of $T = 4.2$ K. Now we will look at the data and see how the measured value of V_{th} compares with the calculated one.

5.4.1 Extracting a threshold voltage from the measured data

First we look at a single measurement of a single device. The sample was kept at a temperature of 4.2 K during the measurements. The device had a width of 410 ± 10 nm and a length of 410 ± 10 nm, thus comprising of a $N \times M = (35 \pm 2) \times (35 \pm 2)$ nanoparticle array. The voltage and current in all figures have been scaled to give the values per molecular junction as described in Section 5.3.1.
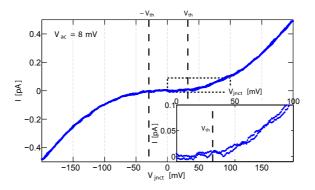
Figure 5.7: An *IV* measurement of a typical device. The data shows an onset of conductance between 0 and ±50 mV. Beyond the threshold voltage the current increases according to a power law. The dashed lines indicate the threshold voltage for conduction. Their positions are extracted from the d^2I/dV^2 data, Figure 5.9

Figure 5.7 shows the measured *IV* curve. The measured curve has an S–shape similar to the calculated curve in Figure 5.6. The onset of conduction is not as clear in the measured data as in the calculated curve. The data shows an onset of conduction somewhere midway between 0 and ±50 mV. Beyond the onset the current increases according to a power law. Figure 5.8 shows the measured derivative of the *IV* curve, namely the dI/dV curve. The data shows a minimum around zero bias voltage. From 0 V to around ±50 mV the differential conductance increases sharply, indicating an onset of conductance. The structure visible in the curve beyond ±50 mV will be described later in the text. From Figures 5.7 and 5.8 it is clear that the onset of conductance takes place between 0 and ±50 mV. The threshold voltage seems to have some spread and it is hard to determine it exactly from these figures.

Looking at the measurement of the second derivative of the *IV*, shown in Figure 5.9, there is a peak/dip between 0 and ±50 mV. The position of this peak/dip is where the steepest slope in the dI/dV is and is taken to correspond to the mean threshold voltage. Beyond ±50 mV are more peaks and dips. Those features will be discussed in detail in Chapter 6. From the d^2I/dV^2 data we extract a threshold voltage of $V_{th}^m =$

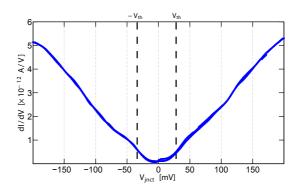**Figure 5.8:** A dI/dV measurement of a typical device. The differential conductance has a minimum around zero bias. The differential conductance increases sharply when the applied bias changes away from zero. This sharp increase in the conductance happens as the charge carriers overcome the Coulomb blockade in the nanoparticles. The dashed lines indicate the threshold voltage for conduction. Their positions are extracted from the d^2I/dV^2 data, Figure 5.9

31 mV. The superscript m is used to indicate a measured value. This corresponds to a charging energy of $E_c^m \approx 20$ meV, the nanoparticle capacitance is $C^m \approx 4$ aF. The measured threshold voltage agrees well with the calculated values, $V_{th}^c = 28$ mV, as well as the charging energy $E_c^c = 19$ meV and the capacitance, $C^c = 4.2$ aF. The observed difference in the measured and calculated capacitance comes from variations in R, s, and ϵ_r from the values stated above.

It is convenient to use the position of the highest peak and lowest dip in the d^2I/dV^2 data to estimate the position of the threshold voltage of the devices. The threshold voltage obtained from the peak/dip position can be thought of as a mean threshold voltage. The width of the peak indicates that there is some distribution in the onset of conductance in the device. The broadening of the peak in the d^2I/dV^2 will be discussed in Section 5.5.

Using the method discussed above the threshold voltage of several devices was measured. Table 5.1 summarises the results of these measurements. The table shows a device number composed of a sample number, first digit, and a device number, second digit. Seven devices on four samples were measured. The table shows the dimensions of the devices in units of nanoparticles. The arrays in the devices are N nanoparticles long and M nanoparticles wide. The measured threshold voltage V_{th}^m is shown for each device. The measured threshold values compare well to a calculated value of $V_{th}^c = 28mV$. The table also shows the values of the exponent ζ and a fitting parameter G_i, the details of these parameters are discussed in the following section.
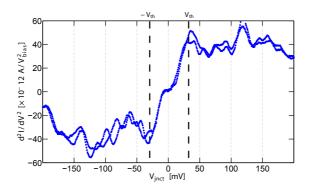
Figure 5.9: A d^2I/dV^2 measurement on a typical device. The highest peak and lowest dip on either side of zero bias voltage correspond to the fast increase in the differential conductance shown in Figure 5.8. The peak position corresponds to the mean threshold voltage to overcome Coulomb blockade and the peak width corresponds to the distribution in energies sufficient to overcome the Coulomb blockade. The dashed lines indicate the threshold voltage for conduction.

Dev.	N	M	V_{th}^m [mV]	ζ	G_i [pS]
S1–D1	13	18	28.8	1.18	0.20
S1–D2	23	31	26.4	1.20	0.14
S2–D1	35	35	25.8	1.43	0.32
S2–D2	37	88	24.6	1.32	0.09
S3–D1	48	19	26.9	1.32	2.30
S3–D2	40	90	30.5	1.33	0.21
S4–D1	19	91	35.1	1.33	0.23

Table 5.1: The values obtained for the threshold voltage V_{th}^m measured by the position of the highest/lowest peak/dip in the d^2I/dV^2 data in seven devices on four samples. The devices measured are numbered by two digits, the first digit indicates a sample number and the second a device number. The dimensions of the device are indicated in units of nanoparticles, the array in the device consists of $N \times M$ nanoparticles. The measured threshold values compare well to a calculated value of $V_{th}^c = 28mV$. The exponent ζ is extracted from Figure 5.10. The parameter G_i is a fitting parameter used to have all IV curves in Figure 5.10 collapse on top of each other.

5.4.2 Determining the exponent ζ

When the threshold voltage is known it is time to inspect the ζ exponent in Equation 5.18. The value of this exponent is related to the dimensionality of the nanoparticle array [35, 47] and the disorder in the array [74].

Equation 5.18 shows that the current, above V_{th}, in the nanoparticle arrays should grow in proportion with the applied voltage and the exponent ζ. It has been shown that
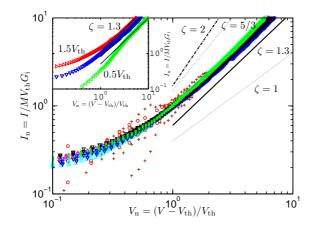
Figure 5.10: *IV* measurements on seven devices from four different samples are shown in the main figure. The current is scaled with $1/MV_{th}G_i$ where M is the number of nanoparticles in parallel in each device, V_{th} is the threshold voltage for conduction in each device, and G_i is a scaling parameter used to make the curves collapse on each other. The slope of the curves at high voltages is fitted to get the exponent ζ. The black solid line shows a curve calculated using Equation 5.18 with $\zeta = 1.3$. The dotted lines are calculated using Equation 5.18 using the ζ values proposed by Middleton and Wingreen [47] and have a slope of 5/3, and 1. The dash–dot line is calculated by Equation 5.18 using $\zeta = 2$ for weakly disordered arrays proposed by Šuvakov and Tadić [74] The inset figure shows a measurement of a single device. The figure shows that changing the threshold voltage used to normalise the *IV* data does not influence the slope of the curve at high bias voltages. The figure shows the same data normalised with different threshold voltages. The blue symbols show the data normalised with the measured V_{th}, the red symbols show the data when a threshold voltage of $1.5V_{th}$ is used, and the green shows the data when a threshold voltage of $0.5V_{th}$ is used to normalise the data. The black lines show a calculated curve with and exponent $\zeta = 1.3$.

in arrays containing $\sim 10^3$ nanoparticles size effects do not govern the conductance [74]. Assuming that the device fabrication is reproducible regarding disorder in the arrays and that the device conductance is not influenced by size effects, one would expect the normalised current $I_n = I/MV_{th}G_i$ to be identical in different devices. Where the measured current I is normalised by the number of nanoparticles spanning the width of the device M, the threshold voltage V_{th}, and an initial conductance G_i. The initial conductance G_i is a fitting parameter used to have all the curves in Figure 5.10 falling on top of each other. The values obtained from fitting G_i are displayed in Table 5.1. The inset in Figure 5.10 shows that changing the threshold voltage used to normalise the data does not influence the slope of the data at high voltages. The figure shows the same data normalised with V_{th} plotted in blue symbols, normalised with $1.5V_{th}$ plotted in red symbols, and normalised with $0.5V_{th}$ plotted in green symbols.

A straight line can be fitted to the measured curves at the high bias end of the plot. The resulting slope corresponds to ζ in Equation 5.18. The fitted ζ values for the measured data in Figure 5.10 are shown in Table 5.1. The value obtained for the exponent is $\zeta = 1.3$. These values are lower than $5/3$ as proposed by Middleton and Wingreen [47] for a two dimensional array, $\zeta = 5/3$. Middleton and Wingreen [47] calculate that the ζ value in a one dimensional array is $\zeta = 1$. One might argue that the value for $\zeta = 1.3$ obtained in the measurements indicates that the arrays behave as though they are in an intermediate regime between purely one dimensional and purely two dimensional. This would suggest that the conductance paths in the array were a mixture of paths confined to a chain of nanoparticles, and paths where electrons are able to meander and branch through a patch of nanoparticles.

A different explanation is offered by Šuvakov and Tadić [74], which calculate $\zeta = 1.3$ in topologically ordered arrays with quenched charge disorder. In the model the arrays have a small dispersion of cell sizes around the hexagonal structure and they are locally homogeneous, with each node in the array having exactly three links. The charge disorder is uniformly distributed at each node and has a size of $0 \leq q_i \leq 1e$, e is the charge of a single electron [74]. The value they calculate corresponds to the values of ζ shown in Table 5.1. The quenched charging disorder could arise from trapped charges in the SiO_2 substrate.

The ζ exponent has been measured by a few groups and the values obtained vary. Elteto et al. [17] measured the transport in quasi one dimensional arrays of Au nanoparticles. The average width of the array was 4 nanoparticles and the length around 60 nanoparticles. They find $\zeta \sim 1.4 - 2.6$. They claim that these narrow arrays have not yet reached the one dimensional limit and that their findings indicate that the current paths are still able to meander and branch. In two dimensional arrays current paths are able to branch as more voltage is applied to the device the electrons have enough energy to overcome higher barriers and can choose new paths. Furthermore, Parthasarathy et al. [52] find $\zeta = 2.25 \pm 0.1$ in two dimensional arrays of hexagonally packed Au nanoparticles with 27–170 nanoparticles spanning the gap between the electrodes and a width of ~ 270 nanoparticles. Their value comes close to the values of ζ in weakly disordered arrays without charge disorder [74].

Liao et al. [45] investigate the influence of the substrate on ζ. They fabricate both free–standing nanoparticle arrays and nanoparticle arrays on a substrate. They measure a value of $\zeta = 2$ for free–standing arrays and report there is a significant difference in the exponent depending on whether the arrays are free standing or on a substrate. They report $\zeta = 2.4$ for arrays on a substrate. The claims made by Liao et al. [45] support the idea that the substrate has an influence on the ζ exponent.

So far, measurements of the ζ exponent in several experiments have given an wide range of values. Theoretically, it has been predicted that the exponent depends on the dimensionality of the conducting paths in the arrays [47] as well as the topological and charging disorder [74]. Even though the range of values the exponent ζ can take has been shown to depend on the topological and charging disorder of the array, the

underlying physical reason was not explained [74].

Charge disorder in the array would influence the threshold voltage for the onset of conductance. The details of the peaks observed in the d^2I/dV^2 can give an indication of whether charge disorder is present in the arrays. This will be discussed in the following section.

5.5 Broadening of Coulomb blockade induced features

In this section we look in detail at the peak/dips around $\pm V_{th}$ in the d^2I/dV^2 data. These peaks/dips were used in Section 5.4.1 to determine the value of the threshold voltage for conduction. These peaks/dips have a finite width. In this section we look at what causes their broadening.

The broadening of a Coulomb blockade induced feature in the d^2I/dV^2 data can be calculated as

$$W_{jnct} = \sqrt{W_T^2 + W_{ac}^2 + W_n^2 + W_a^2 + W_q^2} \qquad (5.20)$$

where W_{jnct} is the full width at half maximum (FWHM) of the measured peak. The broadening includes a thermal broadening term $W_T = 5.4 k_B T N/e$ [56], a term due to the ac modulation used to measure the peak W_{ac}, a broadening term W_n due to the distribution in the nanoparticle capacitance, a term W_a due to topological disorder in the array, and a term W_q due to charge disorder in the array. The broadening due to the ac voltage applied to the junctions is calculated by convoluting a Gaussian peak by an ac voltage and measuring the resulting broadening. The influence of the distribution in the nanoparticle capacitance is calculated as:

$$W_n = \frac{\delta V_{th}}{N} \qquad (5.21)$$

where δV_{th} is the error in the threshold voltage due to the distribution in the charging energy of the nanoparticles, and N is the number of nanoparticles spanning the gap between the electrodes in series. The broadening due to topological disorder in the arrays is found by:

$$W_a = \frac{V_{th}}{N^2} \delta N \qquad (5.22)$$

where δN is the error in the number of nanoparticles bridging the electrodes. The full error calculation is given in Appendix G. The broadening due to charge disorder in the array can be calculated by looking at how the energy of the nanoparticles changes when their charge changes as in Equation 5.3:

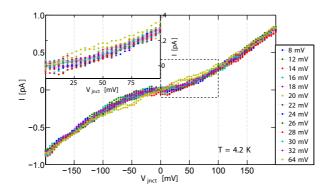$$\Delta U^{\pm} = \frac{(Q \pm e)^2}{2C} + \frac{Q^2}{2C}$$

Figure 5.11: *IV* curves measured while an ac voltage of different amplitudes was added to the dc voltage applied to the device. The figure shows that the *IV* response of the device is not influenced significantly by the ac voltage. When the amplitude of the ac voltage is at 64 mV per molecular junction the onset of conductance around ± 30 mV dc bias is smeared out.

The capacitance of the nanoparticle plays a role in how the energy of the nanoparticles changes when the charge on them changes. The charge disorder is carried forward to the charging energy of the nanoparticles and the threshold voltage. The full error calculation is in Section G.2 in Appendix G. We assume that the error values from the calculations in Appendix G are the standard deviation σ of a Gaussian distribution. Thus, the full width at half maximum values are obtained by $FWHM = \sigma 2 \sqrt{2 \ln(2)}$.

Of the terms contributing to the broadening only the amplitude of the ac voltage and the temperature of the sample can be easily controlled. In the rest of the section we look at how these terms influence the broadening of the peaks.

First we look at the influence of the ac voltage on the peak width. Figures 5.11, 5.12, and 5.13 show the influence of changing the amplitude of the applied ac voltage on the measured current, differential conductance and the second derivative of the current, respectively. The influence of the ac amplitude on the *IV* measurement is minimal, except in the case where 64 mV ac is applied over each molecular junction in the device. With this high ac voltage the onset of conductance above the threshold voltage is washed out in the *IV* curves. This is also evident when one looks at the differential conductance in Figure 5.12. The dip around zero bias voltage decreases monochromically with increasing amplitude of the ac voltage. In the second derivative of the current, Figure 5.13, the peak/dip at $\pm V_{\text{th}}$ is broadened, and lowered with increasing ac voltage. From Figure 5.13 a value of $V_{\text{th}} \approx 30$ mV is found. The amplitude of the largest ac voltage used, 64 mV, is larger than twice the threshold voltage. In the analysis of the data the measurement with this large ac voltage is omitted.
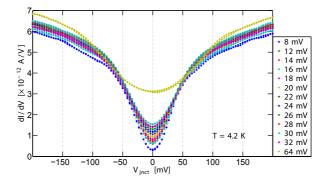
Figure 5.12: dI/dV measurement of the same device as the IV measurement shown in Figure 5.11. The zero bias conductance increases as the amplitude of the ac signal increases. Furthermore, the features in the dI/dV visible beyond the Coulomb blockade are smeared out with increasing amplitude.
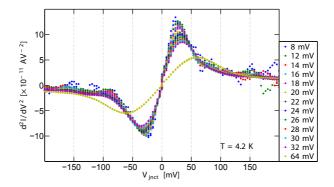
Figure 5.13: The d^2I/dV^2 measurement of the same device as the IV measurement shown in Figure 5.11. The curves are measured using different amplitudes of the ac voltage applied to the device. Most notably the amplitude and the broadening, of the peak around ±30 mV dc bias, decrease and increase, respectively. Features in the curves measured beyond the Coulomb blockade region, peaks on the positive dc bias side and dips on the negative side, are most prominent when the amplitude of the ac voltage is between 14 and 22 mV. Below 14 mV the signal is barely above the noise threshold, above 22 mV ac amplitude smearing of the features starts being apparent and at 64 mV the features are completely washed out.
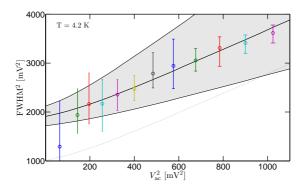
Figure 5.14: The full width at half maximum of the Coulomb induced feature around ± 30 mV dc bias in Figure 5.13. The black dotted line is the calculated full width at half maximum by the thermal broadening, the broadening due to the ac voltage applied to the device, the broadening due to the distribution in nanoparticle capacitances, and the broadening due to topological disorder. The black solid line is the calculated broadening with a broadening term $W_q = 30$ mV added to it. This extra broadening in the peak is assumed to come from the charge disorder in the array. The shaded area represents the error of the calculated broadening, the black line. The width of the shaded area comes from the error of the number of nanoparticles in the conducting path and ±10% of the measured broadening.

The values of the temperature broadening, broadening due to a distribution in the nanoparticle capacitance, broadening due to topological disorder, and charge disorder should all be constant in the device at low temperatures. These broadening values can be calculated and have values of $W_T = 5.4k_B T/e = 2.0$ mV, $W_n = 9.1$ mV, $W_a = 7.6$ mV. The broadening due to charge disorder cannot be calculated directly, since it is impossible to know the exact charge disorder.

Figure 5.14 shows how the broadening squared evolves as the amplitude of the applied ac voltage squared. The black dotted line is the calculated broadening using Equation 5.20 and the broadening values mentioned above, but $W_q = 0$ at this point. The broadening due to the ac voltage is calculated by convoluting an Gaussian peak with an averaging filter of a length equivalent to the amplitude of the ac voltage. The black dotted line is the lowest expected broadening. The black solid line is the same as the black dotted line, but with an extra broadening term $W = 30$ mV added to it. Setting this extra broadening term as W_q one can estimate the charge disorder in the arrays. Following the error calculations in Section G.2 in Appendix G the resulting distribution in the charges on the nanoparticles is $\Delta Q = 0.19e$. The shaded area is found from the error on the number of nanoparticles spanning the length of the device and a ± 10% measurement error of the peak broadening.

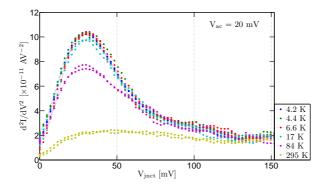The broadening of the Coulomb blockade induced features in the d^2I/dV^2

Figure 5.15: The d^2I/dV^2 measurement of the same device as the IV measurement shown in Figure 5.11. The d^2I/dV^2 signal is measured at different sample temperatures. The measurement shows a similar trend as the measurement shown in Figure 5.13 where the amplitude of the ac voltage was varied. The amplitude decreases as the temperature increases while the full width of the peak at half maximum increases with temperature.

measurement were also measured as a function of temperature for the temperature range from 4.2–300 K, Figure 5.15. The peak evolves in a similar manner with increasing temperature as it did with increasing ac voltage, that is the peak height decreases while its width increases. Figure 5.16 shows the broadening squared plotted as a function of the temperature squared. The main figure shows the data plotted on a log–log scale to emphasise the low temperature values. The inset shows the data on a linear scale. The black dotted line is the calculated broadening using the known broadening parameters, $W_q = 0$ since it is unknown. The broadening per junction W_{jnct}, black curve in Figure 5.16, was calculated using Equation 5.20 and the same parameters for W_n, and W_a as above. The broadening due to the 20 mV ac voltage was found to be $W_{ac} = 34$ mV, which corresponds to the same width as was used above in Figure 5.14. An extra broadening term $W = 35$ mV is added to the calculated broadening. We assume that this extra broadening term corresponds with the broadening due to the charge disorder W_q. This corresponds well with the magnitude for this broadening term obtained when the amplitude of the ac voltage was increased. There it was 30 mV. Broadening due to charge disorder of a magnitude $W_q = 35$ mV, corresponds to a distribution in the charge on the nanoparticles of $\Delta Q = 0.23e$. The black line shows the calculated values of the broadening with $W_q = 35$ mV. The shaded area represents the error in the calculation

The charge distribution on the nanoparticles extracted from the measurement where the amplitude of the ac voltage was varied and the measurements where the temperature of the sample was varied agree well with each other. The charge fluctuations calculated $\Delta Q = 0.2e$ is with in reasonable bounds and might indicate
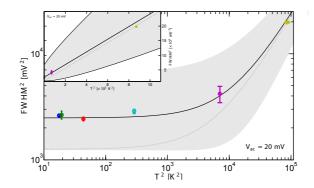
Figure 5.16: The full width at half maximum of the Coulomb induce feature around ± 30 mV dc bias in Figure 5.15. The main figure and the inset show the same data. The main figure shows the data on a double logarithmic scale to emphasise the points measured at low temperatures. The inset shows the data on a double linear scale. The black line shows the calculated broadening using Equation 5.20 setting the broadening due to charge disorder W_q = 35 mV. The grey are represent the error in the calculated broadening. The black dotted curve is the same as the black curve, but with the broadening due to charge disorder W_q = 0 mV. This is the lower limit of the possible broadening.

that charge disorder does play a role in the transport through the devices.

5.6 Summary

In this chapter we have introduced a model for the transport through a double tunnel junction. The model characterises the transport through a nanoparticle coupled to an electrode on either side of it via tunnel junctions. To describe the transport in an array of nanoparticles, building on this model, we investigated how the topology of the nanoparticle array affects the voltage drop over each junction and the current flowing through it. The effects of the environment on the charging energy of a nanoparticle were discussed and the influence of temperature on the transport through a nanoparticle array.

We looked at how to extract the threshold voltage for conductance from our measurements. Using the extracted threshold voltage we could rescale the data and fit it to a model where an exponent in the model describes the topology of the array

as well as the disorder in the array. Two distinct disorders play a role, the topological disorder and the charge disorder in the array.

Looking into the broadening of features arising from Coulomb blockade in the nanoparticle arrays. Several parameters causing broadening can be estimated from error calculations while others can be calculated directly. When comparing the sum of all the known broadening parameters to the measured broadening it is evident that the calculated broadening is smaller than the measured one. Assuming this broadening, which is unaccounted for, stems from the charge disorder we calculate the fluctuations in the nanoparticle charges that would cause broadening of that magnitude.

6

Chapter

The influence of molecules on transport in the nanoparticle arrays

6.1 Introduction

In Chapter 5 we looked at how nanoparticles influence transport in the nanoparticle arrays at low temperatures. From measurements done at room temperature we also know that the molecules present in the nanoparticle arrays contribute to the transport [43]. Not only do the molecules in the array contribute to the transport, but even the oxidation state of the molecules plays a role. As discussed in Chapter 3 the function of a nanoparticle array device can be determined by the function of the molecules in it, at room temperature. In this chapter we will look at the contribution of the molecules in the array to the transport at low temperatures.

Molecular vibrations, phonons, can contribute to the conductance of a metal–molecule–metal junction. The effect is known as inelastic electron tunnelling. The energies of the molecular vibrations contributing to the conductance can be mapped. This mapping is called inelastic electron tunnelling spectroscopy (IETS). The first IETS experiment through a molecular junction was first performed on metal–metal oxide–metal structures where a thin layer of organic molecules had been deposited on the metal oxide [32, 39].

Thirty years after the experiment by Jaklevic and Lambe [32], Stipe et al. [64] could distinguish between hydrogen and deuterium in a single acetylene (C_2H_2) and a deuterated acetylene (C_2D_2) molecule on a copper surface using a scanning tunnelling microscope (STM) in ultra high vacuum. The distinction was made by measuring the vibrational energy of the C–H and C–D stretch modes in the C_2H_2 and C_2D_2 molecules, respectively. Since the first IETS measurements several research

groups have started working on measuring IETS in junctions containing a single molecule. How the electron–phonon interaction influences the conductance of the metal–molecule–metal junction is determined by the junction conductance, the strain of the molecule, the metal–molecule coupling, and other factors [1, 14, 21, 53, 55, 65, 72]. Until now, the methods used to measure IETS are: STM break junction [1, 4, 27, 28, 41, 50, 51, 58], mechanically controllable break junction [15, 65, 66], cross wire junction [6, 38], and electromigrated junction [63]. To our knowledge no one has tried to measure IETS in devices comprising of a collection of molecular junctions, such as a nanoparticle arrays.

As discussed in Chapters 2 and 3 nanoparticle arrays are a highly versatile platform for molecular electronics. They offer the possibility of investigating how a molecule responds to its environment. The properties of individual molecules have been shown to define the transport through the nanoparticle arrays. In particular, the conductance of a nanoparticle array can be changed by illuminating a photo–sensitive molecule to change its conformation [73] or the conductance can be changed by altering the oxidation state of a redox–active molecule [42]. The ability to probe the phonon modes of a molecule before and after such treatment would be of great interest to the molecular electronics community. This would open up the possibility to measure a unique fingerprint of the molecules taking part in the electrical transport in the devices and distinguish between different molecular conformations or oxidation states. Current methods used to measure IETS of molecules do not offer the same flexibility of device treatment as the nanoparticle arrays do.

Previously infrared spectroscopy has been used to identify the molecules present in the nanoparticle arrays [9]. The position of the maximum in UV–vis absorption spectroscopy has been correlated with the conductance of the molecules in the arrays [9, 73]. The next step could be to detect the structure of the molecules taking part in transport directly with IETS.

Measuring the contribution of vibrational modes of individual molecules within an array of nanoparticles is a challenging task. As discussed in Chapter 5 we know that disorder in the array itself would cause the voltage drop over each molecular junction to vary, thus causing broadening of peaks or even the same peak to appear at more than one voltage. The coupling between the electrodes and the array could cause the IETS to be non–symmetric. So far, symmetry has been used to identify IETS peaks from other peaks in the measured signal [4, 27]. The rewards for overcoming the challenges are a better understanding of the transport through molecular devices based on nanoparticle arrays and yet another tool to identify the molecular contribution to the transport in the arrays.

6.1.1 A general description of IETS

The transport through a molecule can be influenced by the electron–phonon (e–ph) interactions during charge transfer. In low conducting junctions $G \ll G_0$, where
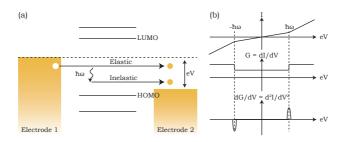
Figure 6.1: (a) Inelastic electron tunnelling becomes possible when an electron tunnelling through a molecule has enough energy eV to excite a vibrational mode, phonon of energy $\hbar\omega$, in the molecule. In a low conducting junction $G \ll G_0$ the electron is scattered forward and the conductance of the junction increases. (b) The increase in conductance is observed as a kink in an IV measurement, a step in the dI/dV measurement, and a peak in the d^2/dV^2 measurement of the junction. The peak positions in the d^2I/dV^2 give a spectrum of the energies of the molecular phonon modes contributing to transport.

$G_0 = 2e^2/h$ is the conductance quantum, the conductance in the junction is enhanced by the e–ph interaction. The electron is scattered inelastically forward and it is said that an inelastic conductance channel opens up. The increase in conductance due to forward scattering of electrons by phonons is on the order of $\sim 1\%$ [4, 18], although an increase as high as 10% has been reported [28]. Since inelastic electron tunnelling causes an increase in conductance it is observed as a kink in the IV measurement, a step in the dI/dV measurement, and a peak in the d^2I/dV^2 measurement, as illustrated in Figure 6.1. The dc part of the current corresponds to the current flowing in the device, the first harmonic of the current corresponds to the differential conductance of the device, and the second harmonic of the current correspond to the second derivative of the current in the device. The detailed Taylor expansion of the current is given in Appendix F. The peak positions in the d^2I/dV^2 measurement give a spectrum of the molecular phonon energies which contribute to transport. This transport spectroscopy is known as inelastic electron tunnelling spectroscopy.

The phonon modes of a molecule can be measured by other means, in particular infrared (IR) and Raman spectroscopy. The main advantage of IETS over IR and conventional Raman spectroscopy is the sensitivity of IETS. While IR and Raman spectroscopies require 10^3 or more molecules to provide a spectrum, IETS can be done on a few molecules trapped between a pair of electrodes [59]. IETS can also be used to determine whether a certain molecule is present in a molecular junction and contributing to the transport.

While the phonon modes observed by IR and Raman spectroscopy are governed by well known selection rules, there are no strict selection rules for IETS [51, 59]. Instead of selection rules, a set of propensity rules has been set forward and used as

guidelines to help determine which phonon modes are expected to take part in the transport. These rules imply that the most important phonon modes to transport are those that are along the most active conduction paths of the molecule. Symmetric modes are usually more active than others [68, 69]. The majority of the measured IETS signal is attributed to a few phonon modes at high energies [19]. In practise, the low energy modes are masked by a zero bias feature caused by scattering in the leads, Coulomb blockade, and other processes [79].

6.1.2 A general IETS measurement of a nanoparticle array device

The IETS of the nanoparticle array device was measured at 4.2 K using the set up described in Chapter 4. Two SR830 Lock–in amplifiers were used during the measurement. One supplying an ac voltage to the sample and measuring the 2nd harmonic of the resulting signal, the other measuring the 1st harmonic of the signal. The measurement was performed by applying a voltage, comprising of a dc part and an ac part, to a device. The dc voltage was increased in small steps, normally one tenth of the amplitude of the ac voltage. Before measuring at each dc voltage we waited until the device and measurement circuit reached steady state. The time for the measurement circuit and device to reach steady state was normally $\sim$ 21 sec for the Lock–in amplifier at 73 Hz with a 12 dB/Oct filter, and a time constant of 3 sec. Normally 400 measurements were performed at each dc bias. The mean value of the 400 points was used as the measured value. This method was preferred, to increase the signal–to–noise ratio, over many voltage sweeps. A normal measurement takes 3–8 hours.

In Section 5.4.1 we looked at an example of a transport measurement in a single device and saw how to locate the threshold voltage V_{th} using peaks in the d^2I/dV^2 measurement. The device was fabricated using the protocol described in Section 4.2. The nanoparticles were coated with S–C8, $(S(CH_2)_7CH_3)$, molecules. The measurement was done by sweeping the voltage from 0 – 200 mV, from 200 – −200 mV, and from −200 – 0 mV. Using the same measurement data again, now we look at the features beyond V_{th}. Figures 6.2, 6.3, and 6.4 show the same data as in Section 5.4.1, IV, dI/dV, and d^2I/dV^2 respectively, the background has been colored to emphasise the features we are interested in. Looking at the d^2I/dV^2 measurement in Figure 6.4 working our way from 0 V: The red area represents an area dominated by the Coulomb blockade; The yellow area emphasises a feature which appears as two peaks on the positive voltage side. On the negative voltage side there is a strong dip there when scanning the voltage from 0 – −200 mV, but it does not appear when scanning the voltage from −200 – 0 mV; The green area emphasises strong peaks/dips symmetric about 0 voltage. The increase in conductance in this area causes a clearly visible step in the dI/dV measurement. The blue area shows two peaks/dips which appear at positive and negative voltage.

In Figure 6.4 it is evident that the fine structure of the measurement is not
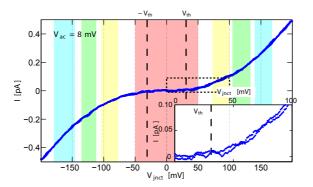
Figure 6.2: An *IV* measurement of a typical device. The colored areas refer to colored areas in Figure 6.4. The measurement was done at 4.2 K and the amplitude of the ac voltage was 8 mV per molecular junction.
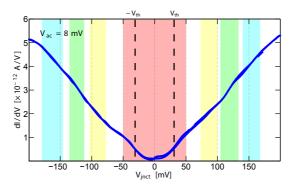

Figure 6.3: A *dI/dV* measurement of a typical device. The colored areas refer to the colored areas in Figure 6.4. The step up in the red and the green areas correspond to strong peaks in the d^2I/dV^2. The measurement was done at 4.2 K and the amplitude of the ac voltage was 8 mV per molecular junction.
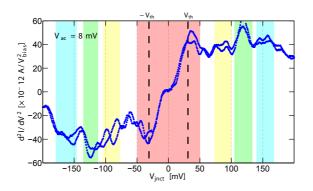
Figure 6.4: A d^2I/dV^2 measurement of a typical device. The peak and dip around ± 30 mV were identified the threshold voltage for conductance. The red area represents the voltage range where any contribution from inelastic tunnelling through molecules is masked by the Coulomb blockade feature. The green area emphasises a strong peak/dip on the positive and negative voltage side, respectively. The blue colored area represents two weak peaks on both voltage sides. The yellow area emphasises two weak peaks on the positive voltage side. On the negative side the same curve is not traced when scanning the voltage from $0-{-}200$ mV and when scanning from $-200{-}0$ mV. The measurement was done at 4.2 K and the amplitude of the ac voltage was 8 mV per molecular junction.

symmetric around 0 V, and that scanning twice over the same voltage does not necessarily give the same exact result. The origin of the asymmetry will be discussed in Section 6.2. The variation in peak heights and positions when scanning the same voltage range from 0 to $\pm V_{max}$ can arise for several reasons. The most probable one is that the current paths in the sample change during the voltage scan. When the voltage is increased new barriers can be overcome and a new current path can be formed. In Section 6.4 we look at the peak positions in the d^2I/dV^2 data more carefully.

Figure 6.5 shows d^2I/dV^2 data from the same device as in Figure 6.4. Here the voltage was swept over a larger range, ± 400 mV instead of ± 200 mV. From Figure 6.5 it is evident that the largest fluctuations in the d^2I/dV^2 measurement are in the bias range from $0 - \pm 200$ mV. In this bias range several active phonon modes have been observed [6, 38, 54, 63]. In our following discussion we will focus on the bias range between ± 200 mV.

6.2 Asymmetric transport

A molecular junction can have an asymmetric *IV* response even though the molecule and electrodes on either side are symmetric. This asymmetry can arise from asymmetric coupling between the molecule and the electrodes [13]. In a relatively
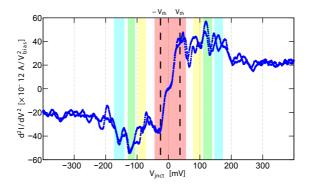
Figure 6.5: A d^2I/dV^2 measurement of a typical device. The dc bias voltage was scanned to ±400 mV. The largest fluctuations in the signal are between 0 and ±200 mV. In this bias range it has been noted that several phonon modes are active [54]. The measurement was done at 4.2 K and the amplitude of the ac voltage was 8 mV per molecular junction.

large nanoparticle array one would, a priory, expect the *IV* response to by symmetric. The nanoparticles are inherently symmetric and all asymmetry due to disorder in the array should average out over the whole array. The coupling between the electrodes, on either side of the array, to the array can induce asymmetric responses in the transport of the array.

Figure 6.6: A schematic showing how an asymmetric contact between the electrodes and the nanoparticle array might arise. The nanoparticle array is stamped on top of the electrodes. The nanoparticle array has to accommodate strain that is induced due to the raised electrodes. In the schematic the distance between the nanoparticles and the left and the right electrode is not identical. This difference in distance causes the asymmetric coupling of the electrodes to the array.

Figure 6.6 shows how asymmetric coupling between two electrodes and a nanoparticle coated with an organic ligand can be formed. The nanoparticle array is stamped on top of the electrodes and has to cover the height difference between the electrodes and the SiO_2. Due to this height difference there will be strain on the nanoparticle array. If this strain is not divided evenly on both sides of the nanoparticle array the distance between the electrodes and the nanoparticle array can be dis–similar

on either side. Thus, the coupling between the electrodes and the array can be asymmetric.
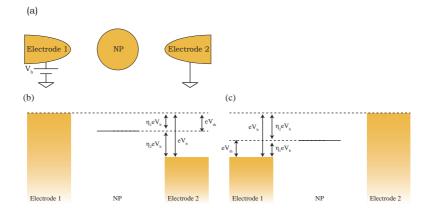

Figure 6.7: A schematic illustrating how an applied bias voltage V_b drops over a double junction comprising of a nanoparticle between two electrodes. A schematic of the junction is shown in figure (a). The schematic shows how the threshold voltage is overcome at the same applied bias voltage V_b when the voltage is applied to Electrode 1, figure (b), or Electrode 2, figure (c). The voltage drops over two junctions: A factor η_1 of the applied voltage drops over the junction between Electrode 1 and the nanoparticle, NP; A factor $\eta_2 = 1 - \eta_1$ drops over the junction between NP and Electrode 2. The voltage needed for conduction to start is $V_{th} \leq |V_b| \min(\eta_1, \eta_2)$.

Figure 6.7 shows a simple model on how the voltage drops over a double junction. A nanoparticle, NP, is trapped between two electrodes. The junctions are assumed to be asymmetric in the sense that a portion of the applied voltage η_1 drops over the junction between Electrode 1 and a nanoparticle NP. A portion $\eta_2 = 1 - \eta_1$ drops over the junction between Electrode 2 and NP. In order for conduction to start the voltage drop over each junction needs to exceed a threshold voltage V_{th}. Even though the junctions are asymmetric the bias voltage V_b needed to overcome the threshold voltage is the same, regardless whether the voltage is applied to Electrode 1 or Electrode 2. The voltage needed for conduction to start is:

$$V_{th} \quad \leq \quad |V_b| \min(\eta_1, \eta_2) \tag{6.1}$$

The nanoparticles are coated with molecules. These molecules bind to the Au nanoparticles with a thiol group giving a strong chemical bond. The electrodes, on the other hand, have no molecules attached to them. It is reasonable to assume that the energy levels associated with the molecules are pinned more strongly to the nanoparticles than the electrodes. To make things simple, we assume that the energy
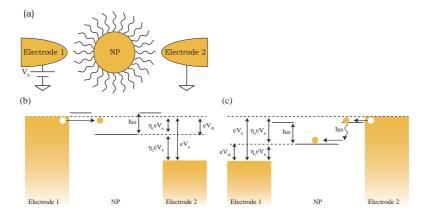
Figure 6.8: A schematic illustrating how a voltage drops over a double junction comprising of a nanoparticle coated with an organic molecule and placed between two electrodes. The structure of the junction is shown in figure (a). The schematic shows how a phonon mode with energy $\hbar\omega$ is not excited when a bias voltage V_b is applied to Electrode 1, figure (b). If the bias voltage is applied to Electrode 2 the phonon mode is excited, figure (c).

levels of the molecules fully follow the energy levels of the nanoparticle. In this case the schematic in Figure 6.8(b) shows how a phonon mode of energy $\hbar\omega$ is not excited when a bias voltage V_b is applied to Electrode 1. Figure 6.8(c) on the other hand, shows how the phonon mode is excited when the bias voltage is applied to Electrode 2.

We have attempted to describe, by a simple model, why the contribution of inelastic electron tunnelling might appear at asymmetric positive and negative bias voltages in the nanoparticle array devices. We attribute the asymmetry in the inelastic transport to asymmetric coupling between the nanoparticle array and the electrodes. A more rigorous model of asymmetry in inelastic tunnelling processes has been developed [20]. It describes how, at low bias voltages far from resonance with HOMO or LUMO of the molecule, the inelastic processes contributing to the transport can become asymmetric while the elastic processes are symmetric. The asymmetric contribution of the inelastic processes is not visible in the IV response since the contribution is so small compared to the contribution of the elastic processes. Asymmetric IETS spectra have been measured in single molecular junctions [57, 66]

6.3 Broadening in peaks beyond the threshold voltage

We have seen in Section 6.1.1 that it is possible to measure peaks in the d^2I/dV^2 beyond the Coulomb blockade. Before looking at IET spectra measured in the arrays we look at the broadening in peaks beyond the threshold voltage. The measurements were performed on a different sample than the measurements shown in Section 6.1.2.
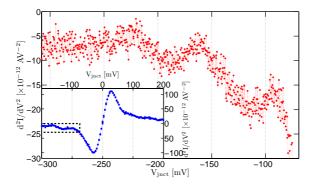

Figure 6.9: A detailed measurement of two negative peaks beyond the threshold voltage. The dc bias voltage is negative in the measurement so the dips in the measurement around -120 mV and -180 mV correspond to peaks while positive voltage is applied to the device. The inset shows the full measurement of the d^2I/dV^2 of the device. The measurements were done at T = 4.2 K.

Looking at the d^2I/dV^2 at voltages beyond the threshold voltage small peaks can be observed. Figure 6.9 shows a close up of two such peaks, the inset shows the d^2I/dV^2 data from the whole voltage scan. Comparing the positions of these peaks, around -120 meV and -180 meV, with the known peaks for S–C8 in Table H.1 in Appendix H one can see that they appear at similar energies as the C–C stretch and a CH_2 wagging and CH_2 twisting phonon modes.

The broadening of these peaks as a function of applied ac voltage is shown in Figures 6.10 and 6.11. Figure 6.10 shows the two peaks after an exponential background has been removed from the measured signal and the sign of the measurement in Figure 6.9 reversed. Gaussian curves have been fitted to each peak, blue dotted curves, and the sum of the two Gaussian curves is also plotted on the figure in a black dotted line. The measurement of the peaks is performed at 12, 16, 20, 24, 28, and 32 mV ac amplitude. Figure 6.11 shows the full width at half maximum of the Gaussian fits in Figure 6.10. The red marks correspond to the peaks around -120 mV and the blue marks correspond to the peaks around -180 mV. The
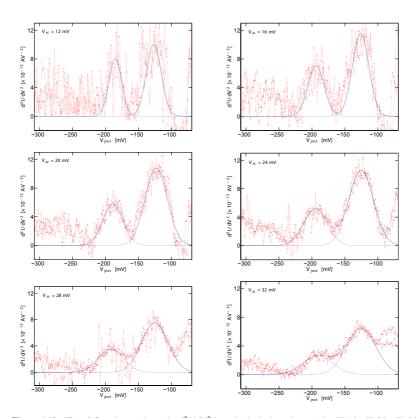
Figure 6.10: Fits of Gaussian peaks to the d^2I/dV^2 in a single device taken at 12 mV, 16 mV, 20 mV, 24 mV, 28 mV, and 32 mV, reading the figures from left to right and top to bottom. The peaks in the figure correspond to the two dips shown in Figure 6.9 with the background removed and the inverse of the sign. The background is determined by fitting an exponential function to the peak around the threshold voltage of the measurement taken with 12 mV ac amplitude. The peak is fitted to the curve between 30% and 80% of the peak height. The same background is used to subtract from all the measurements. The blue curves in the figure show the two individual Gaussian peaks fitted to the measurement and the black curve is the sum of the two blue curves. The measurements were done at T = 4.2 K.
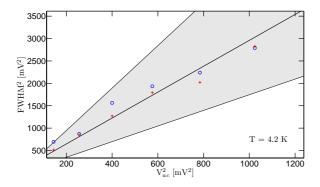
Figure 6.11: The full width half maximum values of the peaks shown in Figure 6.10. The red marks correspond to the peak around −120 mV, and the blue marks correspond to the peak around −180 mV. The FWHM values are extracted from the Gaussian peaks fitted in Figure 6.10. The black line is calculated using the Equation 6.2, with $W_T = 2$ mV and $W_a = 8$ mV. The grey area represents the error in the calculated broadening.

black line is the model broadening given by [37, 39, 41]:

$$W_{\text{jnct}} = \sqrt{W_T^2 + W_{\text{ac}}^2 + W_a^2} \tag{6.2}$$

where $W_T = 5.4 k_B T/e = 2$ mV is the thermal broadening, $W_{\text{ac}} = 1.7 V_{\text{ac}}$ is the broadening due to the applied ac voltage, and $W_a = V_{\text{dc}} \delta N/N = 8$ mV is the broadening due to the topological disorder in the array, N is the number of nanoparticles spanning the gap between the electrodes in series, δN is the error in the number of nanoparticles in series bridging the electrodes as calculated by Equation G.7 in Appendix G. The grey area indicates the error due to the error of the number of nanoparticles bridging the electrodes and ±10% error on the fit of the FWHM. The three broadening factors W_T, W_{ac}, and W_a account for all the observed broadening in the peaks. We assume that each peak is a sum of several peaks, corresponding to several phonon modes, but we cannot resolve them due to the broadening of the measurement.

In this section we discussed a source of broadening in the IETS signal observed in the nanoparticle arrays. The major source of broadening comes from the applied ac voltage and the topological disorder in the arrays. Now we have seen that it is possible to observe the influence of inelastic electron tunnelling on transport in the arrays. The question still remains: Is it possible to identify the molecules present in the arrays from the measured IETS signal?

6.4 Systematic IETS measurements of nanoparticle arrays

In Section 6.1.1 we saw that it is possible to measure IETS peaks in the nanoparticle arrays. We also saw that looking at a single measurement is not enough to determine where the peaks are positioned. There is disorder in the peak positions and two consecutive sweeps do not necessarily have the same fine structure. In Section 6.3 we saw that the major contribution to the broadening in the IETS peaks is due to the ac voltage and topological disorder in the nanoparticle arrays. In this section we discuss how we can try to map out the true IET spectrum of the molecules we measure by measuring the d^2I/dV^2 response of the devices several times and find the most probable peak positions in the data. The measurements in this section were performed on a different device than the measurements in Sections 6.1.2 and 6.3.

Figure 6.12 shows the absolute value of the imaginary part of the d^2I/dV^2 signal measured in a nanoparticle array device. The imaginary part of the d^2I/dV^2 signal has the information about the change in differential conductance due the change in tunnelling rates as a function of voltage, as described in Appendix F. Here we choose to look at the absolute value of the imaginary part of the signal since it is convenient to compare peaks to peaks, at negative and positive bias voltages, with the eye. The nanoparticles were coated with a S–C8 molecule. The top figure shows one measurement cycle. The dc bias voltage was swept from 0 V to 220 mV, from 220 mV to −220 mV, and from −220 mV to 0mV. The data in the figure are not symmetric around 0 V bias and sweeping the voltage from 0 V to 220 mV does not give the same fine structure as sweeping the voltage from 220 mV to 0 V. In order to determine which peaks are coming from vibrational modes of the molecules and which peaks stem from other sources 10 measurement cycles were performed. The lower figure shows the results of the 10 measurement cycles. In the 10 measurement cycles some features seem to appear more often than others. Below we discuss how we can use the information in the 10 measurement cycles to determine which peaks are most likely to appear.

To probe which peaks are specific to the molecule in the array we performed molecular place–exchange on the device measured above. If the molecule is truly contributing to the d^2I/dV^2 signal, two different molecules should have different contributions. In that respect we replaced the S–C8 molecule, containing only C–C bonds between carbon atoms, with a S–OPE–S molecule, containing C–C, C=C, and C≡C carbon–carbon bonds. The structure of the molecules is shown in Figure 6.14. Figure 6.13 shows the absolute value of the imaginary part of the d^2I/dV^2 measurement on the same device as in Figure 6.12. Before this measurement was performed the device was slowly warmed to room temperature, taken out of the dipstick, and molecular place–exchange was performed on it overnight. After molecular place–exchange the device was placed in the dipstick again and cooled to 4.2 K. After molecular place–exchange the features due to Coulomb blockade become sharper after each measurement cycle, as is seen in the Figure 6.13. We
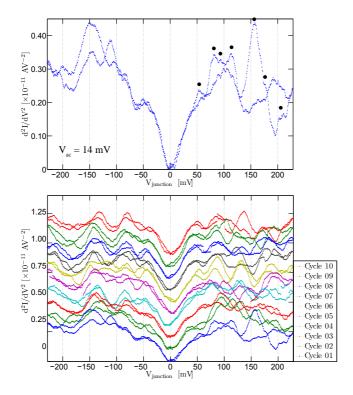
Figure 6.12: IETS measurements of a nanoparticle array device, the absolute value of the imaginary part of the d^2I/dV^2 is plotted. The nanoparticles are coated with a S–C8 molecule. The top figure shows a single measurement. The black dots show an example where peak positions were chosen on the curve. The figures show that the IETS measurement is not symmetric around zero bias voltage. Furthermore, sweeping the bias voltage from 0 V to 220 mV does not give the same fine structure in the data as sweeping the bias voltage from 220 mV to 0V. The lower figure shows 10 consecutive measurements. The voltage is swept from 0V to 220 mV, from 220 mV to −220 mV, and from −220 mV to 0V in each measurement cycle. The results do show some similar features, although the detailed features of each cycle vary. The amplitude of the ac voltage was 14 mV per molecular junction during the measurement. The curves are shifted up for clarity.

interpret this as rearrangement of the nanoparticles. It is possible that during molecular place–exchange the nanoparticles were able to move out of equilibrium. Furthermore, the molecules inserted into the nanoparticle arrays during molecular place–exchange are dithiolated and can interlink two neighbouring nanoparticles [44]. It is possible that by interlinking the nanoparticles strain is induced in the array
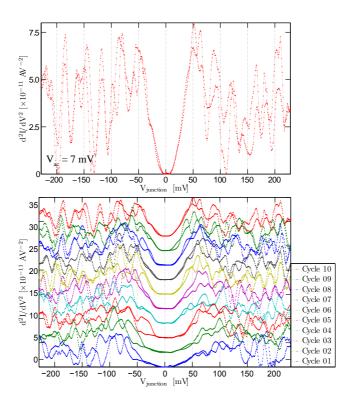
Figure 6.13: IETS measurements of a nanoparticle array device, the absolute value of the imaginary part of the d^2I/dV^2 is plotted. The nanoparticles are coated with a S–OPE–S molecule. The top figure shows a single measurement. The figures shows that the IETS measurement is not symmetric around zero bias voltage. Furthermore, sweeping the bias voltage from 0 V to 220 mV does not give the same fine structure in the data as sweeping the bias voltage from 220 mV to 0V. The lower figure shows 10 consecutive measurements. The voltage is swept from 0V to 220 mV, from 220 mV to −220 mV, and from −220 mV to 0V in each measurement cycle. The results do show some similar features, although the detailed features of each cycle vary from cycle to cycle. The amplitude of the ac voltage was 7 mV per molecular junction during the measurement. The curves are shifted up for clarity.

that relaxes when current flows through it. As discussed above disorder in the array would cause broadening of the peaks. It is unlikely that it would cause new sharp peaks to appear.

There are more peaks observed for the S–OPE–S molecule than the S–C8 molecule. There are several reasons for this. One reason why there are more peaks

in the S–OPE–S measurement is that the molecule has more possible phonon modes than the S–C8 molecule. Furthermore, since the S–OPE–S molecule is a stiff rod like molecule with the option to bind to two neighbouring nanoparticles, it is probable that it is strained in the junctions. It has been shown that due to strain peak positions in an IET spectra can be shifted by about 5 meV/Å [4]. When S–OPE–S molecules are brought close together a $\pi - \pi$ coupling can influence the transport through it [77]. It is unknown how this coupling would influence the IET spectra of the molecules. Finally, the measurement of the S–C8 molecule was done with 14 mV ac applied to each junction while the measurement of the S–OPE–S was done with 7 mV per junction. This means that the resolution in the S–OPE–S measurement is better than in the S–C8 measurement.

One way of quantifying the probability of a peak appearing at a certain dc bias voltage is to identify the positions of each peak in each curve and use them to build a peak–position probability–density function (PDF) [4]. The black dots in Figure 6.12 show an example of selected peak positions in the scan from $0 - -220$ mV. The PDF is obtained by summing up Lorentzian functions centered at each peak position V_{peaks}. The PDF is described by

$$f(V_{\text{dc}}) \quad = \quad \sum_{\text{peaks}} \frac{\epsilon/\pi}{(V_{\text{dc}} - V_{\text{peaks}})^2 + \epsilon^2}, \tag{6.3}$$

where the width of the peak is taken to be $\epsilon = \sqrt{(5.4 k_{\text{B}} T/e)^2 + (1.7 V_{\text{ac}})^2}/10$. Two PDFs are generated, one for the positive bias voltages and one for the negative bias voltages. The PDFs are normalised so that the highest peak in the two PDFs is equal to one. The purpose of the PDFs is to show at which dc bias voltages the peaks appear. They are not intended to indicate the height of each peak, thus the contribution of each phonon mode to the transport cannot be quantified using theses plots.

Figure 6.14 shows peak–position probability–density plots of the IETS peaks for the two measured molecules, S–C8 and S–OPE–S. The red and blue dots indicate, respectively, dip positions on the negative voltage side and peak positions on the positive voltage side in the d^2I/dV^2 measurements in Figures 6.12 and 6.13. The red and blue lines show the probability of a peak appearing at a certain dc voltage, calculated using Equation 6.3. The curves are normalised so that the highest probability of the negative voltage or the positive voltage curve is equal to one. The black solid lines show the mean value of the d^2I/dV^2 curves. A separate mean value is calculated for the curves at negative biases and positive biases. Next to the PDF figures are schematics of the two molecules measured. The grey areas indicate the regions where phonon modes are known to be active [54]. The width of the grey areas is set to be equal to the calculated peak broadening $W_{\text{jnct}} = 14$ mV.

The PDFs in Figure 6.14 show a clear difference in the peak positions observed for the S–C8 and the S–OPE–S molecules. The grey areas show reported values of phonon modes active in the transport of similar molecules to the ones we measure,
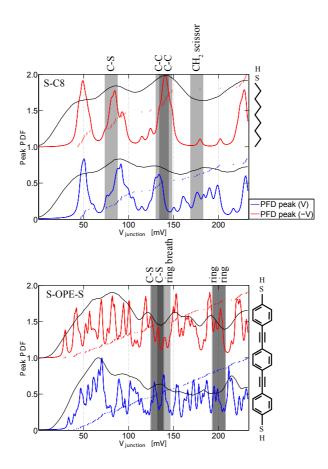
Figure 6.14: Peak–position probability–density plot of the peak positions obtained from Figures 6.12 and 6.13. Red and blue dots indicate the positions of peaks observed in the figures. Red values indicate the position of dips on the negative voltage side and blue values indicate the position of peaks on the positive voltage side. The red and blue lines show the PDF as calculated by Equation 6.3 of the peaks indicated by the red and the blue dots, respectively. The black lines show the mean IETS signal of the 10 cycles shown in Figures 6.12 and 6.13. A separate mean is calculated for the negative and positive voltage sides. The molecular structures of the two molecules measured are shown next to the PDFs. The grey areas indicate phonon modes of similar molecules, S–C11 and S–OPE–S, proposed by Paulsson et al. [54]. The width of the grey areas equals the calculated broadening $W_{jnct} = 14$ mV.

namely S–C11 and S–OPE–S [54]. Although candidate phonon modes are indicated in the figures further investigations are needed to gain a clear IET spectrum. A comprehensive list of known phonon modes for alkane molecules is available in Appendix H.

6.5 Conclusions

In this chapter we have looked at whether it is possible to measure IET spectra in the nanoparticle array devices. We found that there are peaks in the d^2I/dV^2 measurement beyond the threshold voltage and those peaks are most probably due to scattering of electrons on phonons in the molecules in the devices. These peaks can appear at non–symmetric dc voltages about 0V. We attribute this observed asymmetry in the d^2I/dV^2 data to asymmetry in the devices, where the nanoparticle arrays contact the metallic electrodes on each side in an asymmetric manner. The broadening of the IETS peaks can be accounted for by the thermal broadening, broadening due to the applied ac voltage, and the broadening due to the topological disorder in the arrays. Doing several measurements of the same device and collecting the observed peak positions into peak–position probability–density plots might help identify the molecules in the devices.

We showed that it is possible to distinguish between two molecules in the arrays. Measuring two different molecules, before and after molecular place–exchange, in the same device gave different spectra. It is however difficult to assign vibrational modes to the observed peaks and identify the molecule or components of the molecule using the measured spectra.

In spite of the disorder in the arrays we were able to measure the influence of the molecular vibrations on the transport through the nanoparticle arrays. This confirms our former findings that the transport through the array is determined by the individual molecules bridging the nanoparticles [42, 73]. Our findings indicate that although challenging, IETS might be one more tool in our already extensive spectroscopic toolbox and could be useful to gain access to the finer details of the molecular contribution to the transport in our devices.

Part III

Back matter

Chapter 7

Conclusions and outlook

We have shown that at room temperature the transport through our nanoparticle array devices can be tuned with the oxidation state of a redox–active molecule inserted in the arrays. The devices showed a significant increase in conductance after oxidation of the molecule. The conductance was restored close to the starting conductance by reducing the molecule back to its neutral state. The tuning of the device conductance by oxidation and reduction could be repeated several times in the same device. These measurements show that our devices are an interesting platform for molecular electronics where the function of the device is defined by the molecules in it. The function of the molecules is preserved even when they have contacted the nanoparticles and the devices are shown to withstand several cycles of a treatment with organic solvents without losing their function. These measurements were discussed in Part I.

Until now, the width of the nanoparticle arrays has been controlled by patterned PDMS stamps and the distance between the electrodes was controlled by the distance between openings in a TEM grid. This method of patterned PDMS stamps and TEM grids to define the device geometry is limited in flexibility. To gain more precise control over the nanoparticle array geometry a new method had to be developed.

We developed a way of patterning the device on top of a SiO_2 substrate using e–beam lithography. We can adjust the device geometry to our needs. By first depositing the electrodes and an etching mask, then etching away the SiO_2 around the electrodes and leaving a small area of SiO_2 between them. The nanoparticle arrays were then transferred on top of the structures with an unstructured PDMS stamp. Gaining this level of control over the array dimensions was challenging but we were rewarded with the possibility of investigating the transport through the arrays in more depth than ever.

We chose to use our small nanoparticle arrays to investigate the non–linear transport through our devices. We were interested in separating the contribution from the nanoparticles and the molecules to the transport. To do this we performed transport measurements on our devices at liquid He temperatures.

We were able to measure the influence of the Coulomb blockade, due to the small size of the nanoparticles, on the transport. At higher bias voltages we saw evidence of the contribution of molecular vibrations to the transport. By doing molecular place–exchange on a single device we observed different signatures of the vibrational modes of the individual molecules to the transport. We can now quantify the disorder in the arrays and determine its contribution to the transport. This was discussed in Part II.

7.1 Outlook

Our measurements of the conductance of a nanoparticle array device controlled by the oxidation state of individual molecules pave the way towards using nanoparticle arrays as an interface to monitor chemical processes. The high surface area of the nanoparticles in the arrays make them interesting as sensing platforms. Having a large surface to volume ratio in a detector increases the odds of capturing the small amount of molecules present in a dilute solution. The next step towards using the nanoparticle arrays as transport sensitive chemical sensors concern performing electrical transport measurements in a solution. The challenges that need to be over come to accomplish this concern decreasing leakage current from the electrodes through the solution and increasing the device sensitivity to interactions between the molecules in the solution and the nanoparticle arrays. The ultimate limit would be, for example, to detect the oxidation of a single redox–active molecule in the array.

A part of the solution to the challenges stated above was be to be able to make the nanoparticle arrays as small as one likes and have good control over the electrode geometry. To reduce the leakage current between the electrodes their area should be kept as small as possible. To work at low voltages, in order to prevent electrochemical breakdown of the solvent, the distance between the electrodes needs to be small. To be sensitive to the oxidation of a single redox–active molecule the arrays should ideally be one dimensional. Thus, controlling the geometry of the devices precisely is important.

One way to utilise the mechanical stability of molecular junctions on a substrate and avoid the problems of the disorder in the nanoparticle arrays is to contact a single nanoparticle with two electrodes. In a recent collaboration with Hassan Jafri and Klaus Leifer at the Department of Engineering Sciences, Electron Microscopy and Nanoengineering at Uppsala University, we measured the transport through devices comprising of 5 nm diameter nanoparticles trapped in 20 nm wide nanogaps. The nanogaps were made by cutting through a thin gold wire, patterned with e–beam lithography, by a focused ion beam (FIB). The results of these measurements are

presented in Appendix A.

A reoccurring question in molecular electronics is how to independently control the mechanical and electrical coupling of a molecule to the electrodes. One idea proposed to answer the question is to prepare ligands which can wrap around a small gold nanoparticle and give good mechanical stability. The electrical coupling between the molecule and the nanoparticle can then be addressed separately. In this way it is possible to synthesise dumbbell molecules, comprising of two nanoparticles and the molecule bridging them [26]. Nanogap structures might be useful to contact such dumbbell molecules.

In order to know the electronic transport paths in our arrays detailed KPFM measurements are needed. The collaboration with Thilo Glatzel and Marcin Kisiel is still running and we hope that in the future we can directly measure the asymmetry of the coupling between the electrodes and the nanoparticle array and see how the current paths branch through the array.

The possibilities are endless and our imagination is the only limitation, besides the limitation of time.

Bibliography

[1] Agrait, N., Untiedt, C., Rubiobollinger, G., and Vieira, S. (2002). Electron transport and phonons in atomic wires. *Chemical Physics*, 281(2-3):231–234.

[2] Amman, M., Wilkins, R., Jacob, E. B., Maker, P. D., and Jaklevic, R. C. (1991). Analytic solution for the current-voltage characteristic of two mesoscopic tunnel junctions coupled in series. *Physical Review B*, 43(1):1146–1149.

[3] Andreu, R. (2001). Electronic absorption spectra of closed and open-shell tetrathiafulvalenes: the first time-dependent density-functional study. *Tetrahedron*, 57(37):7883–7892.

[4] Arroyo, C. R., Frederiksen, T., Bollinger, G. R., Vélez, M., Arnau, A., Portal, D. S., and Agrait, N. (2010). Characterization of single-molecule pentanedithiol junctions by inelastic electron tunneling spectroscopy and first-principles calculations. *Physical Review B*, 81(7):075405.

[5] Aviram, A. and Ratner, M. A. (1974). Molecular rectifiers. *Chemical Physics Letters*, 29(2):277–283.

[6] Beebe, J. M., Moore, H. J., Lee, T. R., and Kushmerick, J. G. (2007). Vibronic Coupling in Semifluorinated Alkanethiol Junctions: Implications for Selection Rules in Inelastic Electron Tunneling Spectroscopy. *Nano Letters*, 7(5):1364–1368.

[7] Beloborodov, I. S., Lopatin, A. V., Vinokur, V. M., and Efetov, K. B. (2007). Granular electronic systems. *Reviews of Modern Physics*, 79(2):469–518.

[8] Bendikov, M., Wudl, F., and Perepichka, D. F. (2004). Tetrathiafulvalenes, Oligoacenenes, and Their Buckminsterfullerene Derivatives: The Brick and Mortar of Organic Electronics. *Chemical Reviews*, 104(11):4891–4946.

[9] Bernard, L., Kamdzhilov, Y., Calame, M., Van der Molen, S. J., Liao, J., and Schönenberger, C. (2007). Spectroscopy of Molecular Junction Networks Obtained by Place Exchange in 2D Nanoparticle Arrays. *J. Phys. Chem. C*, 111(50):18445–18450.

[10] Blom, T., Welch, K., Strømme, M., Coronel, E., and Leifer, K. (2007). Fabrication and characterization of highly reproducible, high resistance nanogaps made by focused ion beam milling. *Nanotechnology*, 18(28):285301.

[11] Bryant, M. A. and Pemberton, J. E. (1991). Surface Raman scattering of self-assembled monolayers formed from 1-alkanethiols: behavior of films at gold and comparison to films at silver. *Journal of the American Chemical Society*, 113(22):8284–8293.

[12] Castiglioni, C., Gussoni, M., and Zerbi, G. (1991). Charge mobility in sigma-bonded molecules: The infrared spectrum of polymethylene chains in the solid and liquid phases. *The Journal of Chemical Physics*, 95(10):7144–7149.

[13] Datta, S., Tian, W., Hong, S., Reifenberger, R., Henderson, J. I., and Kubiak, C. P. (1997). Current-Voltage Characteristics of Self-Assembled Monolayers by Scanning Tunneling Microscopy. *Physical Review Letters*, 79(13):2530–2533.

[14] de la Vega, Rodero, A. M., Agrait, N., and Yeyati, A. L. (2006). Universal features of electron–phonon interactions in atomic wires. *Physical Review B*, 73(7):075428.

[15] Djukic, D., Thygesen, K. S., Untiedt, C., Smit, R. H. M., Jacobsen, K. W., and van Ruitenbeek, J. M. (2005). Stretching dependence of the vibration modes of a single–molecule Pt–h_2–Pt bridge. *Physical Review B*, 71(16):161402.

[16] Donkers, R. L., Song, Y., and Murray, R. W. (2004). Substituent Effects on the Exchange Dynamics of Ligands on 1.6 nm Diameter Gold Nanoparticles. *Langmuir*, 20(11):4703–4707.

[17] Elteto, K., Lin, X. M., and Jaeger, H. M. (2005). Electronic transport in quasi-one-dimensional arrays of gold nanocrystals. *Physical Review B*, 71(20):205412.

[18] Frederiksen, T., Lorente, N., Paulsson, M., and Brandbyge, M. (2007). From tunneling to contact: Inelastic signals in an atomic gold junction from first principles. *Physical Review B*, 75(23):235441.

[19] Gagliardi, A., Solomon, G. C., Pecchia, A., Frauenheim, T., Di Carlo, A., Hush, N. S., and Reimers, J. R. (2007). A priori method for propensity rules for inelastic electron tunneling spectroscopy of single-molecule conduction. *Physical Review B*, 75(17):174306.

[20] Galperin, M., Nitzan, A., Ratner, M. A., and Stewart, D. R. (2005). Molecular Transport Junctions: Asymmetry in Inelastic Tunneling Processes. *The Journal of Physical Chemistry B*, 109(17):8519–8522.

[21] Galperin, M., Ratner, M. A., and Nitzan, A. (2004). Inelastic electron tunneling spectroscopy in molecular junctions: Peaks and dips. *The Journal of Chemical Physics*, 121(23):11965–11979.

[22] Gimzewski, J. K. and Möller, R. (1987). Transition from the tunneling regime to point contact studied using scanning tunneling microscopy. *Physical Review B*, 36(2):1284–1287.

[23] Grüter, L., Cheng, F., Heikkilä, T. T., Teresa González, M., Diederich, F., Schönenberger, C., and Calame, M. (2005). Resonant tunnelling through a C60 molecular junction in a liquid environment. *Nanotechnology*, 16(10):2143–2148.

[24] Hanna, A. E. and Tinkham, M. (1991). Variation of the Coulomb staircase in a two-junction system by fractional electron charge. *Physical Review B*, 44(11):5919–5922.

[25] Heeger, A. J. (2001). Nobel Lecture: Semiconducting and metallic polymers: The fourth generation of polymeric materials. *Reviews of Modern Physics*, 73(3):681–700.

[26] Hermes, J. P., Sander, F., Peterle, T., and Mayor, M. (2011). Nanoparticles to Hybrid Organic-Inorganic Superstructures. *CHIMIA International Journal for Chemistry*, 65(4):219–222.

[27] Hihath, J., Arroyo, C. R., Rubio-Bollinger, G., Tao, N., and Agrait, N. (2008). Study of Electron–Phonon Interactions in a Single Molecule Covalently Connected to Two Electrodes. *Nano Letters*, 8(6):1673–1678.

[28] Hihath, J., Bruot, C., and Tao, N. (2010). Electron–Phonon Interactions in Single Octanedithiol Molecular Junctions. *ACS Nano*, 4(7):3823–3830.

[29] Hostetler, M. J., Templeton, A. C., and Murray, R. W. (1999). Dynamics of Place-Exchange Reactions on Monolayer-Protected Gold Cluster Molecules. *Langmuir*, 15(11):3782–3789.

[30] Jafri, S. H. M, Blom, T., Wallner, A., Welch, K., Strømme, M., Ottosson, H., and Leifer, K. (2010). Control of junction resistances in molecular electronic devices fabricated by FIB. *Microelectronic Engineering*.

[31] Jafri, S. H. M., Blom, T., Leifer, K., Strømme, M., Löfås, H., Grigoriev, A., Ahuja, R., and Welch, K. (2010). Assessment of a nanoparticle bridge platform for molecular electronics measurements. *Nanotechnology*, 21(43):435204.

[32] Jaklevic, R. C. and Lambe, J. (1966). Molecular Vibration Spectra by Electron Tunneling. *Physical Review Letters*, 17(22):1139–1140.

[33] Jan van der Molen, S. and Liljeroth, P. (2010). Charge transport through molecular switches. *Journal of Physics: Condensed Matter*, 22(13):133001.

[34] Joseph, Y., Besnard, I., Rosenberger, M., Guse, B., Nothofer, H. G., Wessels, J. M., Wild, U., Knop-Gericke, A., Su, D., Schlogl, R., Yasuda, A., and Vossmeyer, T. (2003). Self-Assembled Gold Nanoparticle/Alkanedithiol Films: Preparation, Electron Microscopy, XPS-Analysis, Charge Transport, and Vapor-Sensing Properties. *J. Phys. Chem. B*, 107(30):7406–7413.

[35] Kardar, M., Parisi, G., and Zhang, Y. C. (1986). Dynamic Scaling of Growing Interfaces. *Physical Review Letters*, 56(9):889–892.

[36] Kato, H. S., Noh, J., Hara, M., and Kawai, M. (2002). An HREELS Study of Alkanethiol Self-Assembled Monolayers on Au(111). *The Journal of Physical Chemistry B*, 106(37):9655–9658.

[37] Klein, J., Léger, A., Belin, M., Défourneau, D., and Sangster, M. J. L. (1973). Inelastic-Electron-Tunneling Spectroscopy of Metal-Insulator-Metal Junctions. *Physical Review B*, 7(6):2336–2348.

[38] Kushmerick, J. G., Lazorcik, J., Patterson, C. H., Shashidhar, R., Seferos, D. S., and Bazan, G. C. (2004). Vibronic Contributions to Charge Transport Across Molecular Junctions. *Nano Letters*, 4(4):639–642.

[39] Lambe, J. and Jaklevic, R. C. (1968). Molecular Vibration Spectra by Inelastic Electron Tunneling. *Physical Review Online Archive (Prola)*, 165(3):821–832.

[40] Lambe, J. and Jaklevic, R. C. (1969). Charge-Quantization Studies Using a Tunnel Capacitor. *Physical Review Letters*, 22(25):1371–1375.

[41] Lauhon, L. J. and Ho, W. (2001). Effects of temperature and other experimental variables on single molecule vibrational spectroscopy with the scanning tunneling microscope. *Review of Scientific Instruments*, 72(1):216–223.

[42] Liao, J., Agustsson, J. S., Wu, S., Schönenberger, C., Calame, M., Leroux, Y., Mayor, M., Jeannin, O., Ran, Y.-F., Liu, S.-X., and Decurtins, S. (2010). Cyclic Conductance Switching in Networks of Redox–Active Molecular Junctions. *Nano Letters*, 10(3):759–764.

[43] Liao, J., Bernard, L., Langer, M., Schönenberger, C., and Calame, M. (2006). Reversible Formation of Molecular Junctions in 2D Nanoparticle Arrays. *Advanced Materials*, 18(18):2444–2447.

[44] Liao, J., Mangold, M. A., Grunder, S., Mayor, M., Schönenberger, C., and Calame, M. (2008). Interlinking Au nanoparticles in 2D arrays via conjugated dithiolated molecules. *New J. Phys.*, 10(6):065019.

[45] Liao, J., Zhou, Y., Huang, C., Wang, Y., and Peng, L. (2011). Fabrication, Transfer, and Transport Properties of Monolayered Freestanding Nanoparticle Sheets. *Small*, 7(5):583–587.

[46] Mantooth, B. A. and Weiss, P. S. (2003). Fabrication, assembly, and characterization of molecular electronic components. *Proceedings of the IEEE*, 91(11):1785–1802.

[47] Middleton, A. A. and Wingreen, N. S. (1993). Collective transport in arrays of small metallic dots. *Physical Review Letters*, 71(19):3198–3201.

[48] Muller, C., Van Ruitenbeek, J., and Dejongh, L. (1992). Experimental observation of the transition from weak link to tunnel junction. *Physica C: Superconductivity*, 191(3-4):485–504.

[49] Nonnenmacher, M., O'Boyle, M. P., and Wickramasinghe, H. K. (1991). Kelvin probe force microscopy. *Applied Physics Letters*, 58(25):2921–2923.

[50] Okabayashi, N. and Komeda, T. (2009). Inelastic electron tunneling spectroscopy with a dilution refrigerator based scanning tunneling microscope. *Measurement Science and Technology*, 20(9):095602.

[51] Okabayashi, N., Paulsson, M., Ueba, H., Konda, Y., and Komeda, T. (2010). Inelastic Tunneling Spectroscopy of Alkanethiol Molecules: High-Resolution Spectroscopy and Theoretical Simulations. *Physical Review Letters*, 104(7):077801.

[52] Parthasarathy, R., Lin, X. M., Elteto, K., Rosenbaum, T. F., and Jaeger, H. M. (2004). Percolating through Networks of Random Thresholds: Finite Temperature Electron Tunneling in Metal Nanocrystal Arrays. *Physical Review Letters*, 92(7):076801.

[53] Paulsson, M., Frederiksen, T., and Brandbyge, M. (2005). Modeling inelastic phonon scattering in atomic- and molecular-wire junctions. *Physical Review B*, 72(20):201101.

[54] Paulsson, M., Frederiksen, T., and Brandbyge, M. (2006). Inelastic Transport through Molecules: Comparing First–Principles Calculations to Experiments. *Nano Letters*, 6(2):258–262.

[55] Paulsson, M., Frederiksen, T., Ueba, H., Lorente, N., and Brandbyge, M. (2008). Unified Description of Inelastic Propensity Rules for Electron Transport through Nanoscale Junctions. *Physical Review Letters*, 100(22):226604.

[56] Pekola, J. P., Hirvi, K. P., Kauppinen, J. P., and Paalanen, M. A. (1994). Thermometry by Arrays of Tunnel Junctions. *Physical Review Letters*, 73(21):2903–2906.

[57] Rahimi, M. and Hegg, M. (2009). Probing charge transport in single-molecule break junctions using inelastic tunneling. *Physical Review B*, 79(8):081404.

[58] Rahimi, M. and Troisi, A. (2009). Probing local electric field and conformational switching in single-molecule break junctions. *Physical Review B*, 79(11):113413.

[59] Reed, M. (2008). Inelastic electron tunneling spectroscopy. *Materials Today*, 11(11):46–50.

[60] Salomon, A., Cahen, D., Lindsay, S., Tomfohr, J., Engelkes, V. B., and Frisbie, C. D. (2003). Comparison of Electronic Transport Measurements on Organic Molecules. *Adv. Mater.*, 15(22):1881–1890.

[61] Santhanam, V. and Andres, R. P. (2004). Microcontact Printing of Uniform Nanoparticle Arrays. *Nano Letters*, 4(1):41–44.

[62] Santhanam, V., Liu, J., Agarwal, R., and Andres, R. P. (2003). Self-Assembly of Uniform Monolayer Arrays of Nanoparticles. *Langmuir*, 19(19):7881–7887.

[63] Song, H., Kim, Y., Jeong, H., Reed, M. A., and Lee, T. (2010). Coherent Tunneling Transport in Molecular Junctions. *The Journal of Physical Chemistry C*, 114(48):20431–20435.

[64] Stipe, B. C., Rezaei, M. A., and Ho, W. (1998). Single-Molecule Vibrational Spectroscopy and Microscopy. *Science*, 280(5370):1732–1735.

[65] Tal, O., Krieger, M., Leerink, B., and van Ruitenbeek, J. M. (2008). Electron-Vibration Interaction in Single-Molecule Junctions: From Contact to Tunneling Regimes. *Physical Review Letters*, 100(19):196804.

[66] Taniguchi, M., Tsutsui, M., Yokota, K., and Kawai, T. (2009). Inelastic electron tunneling spectroscopy of single-molecule junctions using a mechanically controllable break junction. *Nanotechnology*, 20(43):434008.

[67] Tran, T. B., Beloborodov, I. S., Hu, J., Lin, X. M., Rosenbaum, T. F., and Jaeger, H. M. (2008). Sequential tunneling and inelastic cotunneling in nanoparticle arrays. *Physical Review B (Condensed Matter and Materials Physics)*, 78(7):075437.

[68] Troisi, A. and Ratner, M. A. (2006). Molecular Transport Junctions: Propensity Rules for Inelastic Electron Tunneling Spectra. *Nano Letters*, 6(8):1784–1788.

[69] Troisi, A. and Ratner, M. A. (2006). Propensity rules for inelastic electron tunneling spectroscopy of single-molecule transport junctions. *The Journal of Chemical Physics*, 125(21):214709.

[70] Trouwborst, M. L., Huisman, E. H., van der Molen, S. J., and van Wees, B. J. (2009). Bistable hysteresis and resistance switching in hydrogen-gold junctions. *Physical Review B*, 80(8):081407.

[71] Tsutsui, G., Huang, S., Sakaue, H., Shingubara, S., and Takahagi, T. (2001). Well-size-controlled Colloidal Gold Nanoparticles Dispersed in Organic Solvents. *Jan. J. Appl. Phys*, 40:346–349.

[72] Ueba, H., MII, T, and Tikhodeev, S. (2007). Theory of inelastic tunneling spectroscopy of a single molecule – Competition between elastic and inelastic current. *Surface Science*, 601(22):5220–5225.

[73] van der Molen, S. J., Liao, J., Kudernac, T., Agustsson, J. S., Bernard, L., Calame, M., van Wees, B. J., Feringa, B. L., and Schönenberger, C. (2009). Light–Controlled Conductance Switching of Ordered Metal–Molecule–Metal Devices. *Nano Letters*, 9(1):76–80.

[74] Šuvakov, M. and Tadić, B. (2010). Modeling collective charge transport in nanoparticle assemblies. *Journal of Physics: Condensed Matter*, 22(16):163201.

[75] Wang, C., Batsanov, A. S., and Bryce, M. R. (2004). Electrochromic tetrathiafulvalene derivatives functionalised with 2,5-diaryl-1,3,4-oxadiazole chromophores. *Chem. Commun.*, (5):578–579.

[76] Wang, C., Palsson, L. O., Batsanov, A. S., and Bryce, M. R. (2006). Molecular Wires Comprising π-Extended Ethynyl- and Butadiynyl-2,5-Diphenyl-1,3,4-Oxadiazole Derivatives: Synthesis, Redox, Structural, and Optoelectronic Properties. *J. Am. Chem. Soc.*, 128(11):3789–3799.

[77] Wu, S., Gonzalez, M. T., Huber, R., Grunder, S., Mayor, M., Schonenberger, C., and Calame, M. (2008). Molecular junctions based on aromatic coupling. *Nature Nanotechnology*, 3(9):569–574.

[78] Zabet-Khosousi, A. and Dhirani, A.-A. (2008).   Charge Transport in Nanoparticle Assemblies. *Chemical Reviews*, 108(10):4072–4124.

[79] Zimmerman, D. T., Weimer, M. B., and Agnolet, G. (1999). An adjustable oxide-free tunnel junction for vibrational spectroscopy of molecules. *Applied Physics Letters*, 75(16):2500–2502.

Appendix A

Measurements on nanoparticles trapped in nanogaps

A.1 Introduction

We had the opportunity to collaborate with Hassan Jafri and Klaus Leifer at the Department of Engineering Sciences, Electron Microscopy and Nanoengineering at Uppsala University. They make devices of nanoparticles trapped in nanogaps[10, 31, 30]. These devices are interesting for us since they contain far fewer nanoparticles than our current devices. The first results of our measurements on their devices are shown in this appendix.

A priory these devices were promising for IETS measurements since they have only a few, $\sim 3 - 5$, nanoparticles in series between the electrodes. As we realised during our measurements, although promising, these devices had their drawbacks. As seen in Figure A.1 some of the devices had very asymmetric *IV* responses. These asymmetries arise from the size distribution of the nanoparticles in the gaps. They have a diameter of 5 ± 1 nm. The charging energies of individual nanoparticle range from $E_c = 100$ meV for an individual 6 nm diameter nanoparticle to $E_c = 150$ meV for 4 nm diameter nanoparticle. The voltages needed to overcome Coulomb blockade in these nanoparticles are $V_{CB} = 200$ mV and $V_{CB} = 300$ mV for the 6 and 4 nm diameter nanoparticles, respectively. The nanoparticles are trapped in the nanogaps using delectrophoretic trapping. The coupling between the electrodes and clusters of nanoparticles is probably asymmetric, although it is hard to estimate the asymmetry. Furthermore, the conducting paths through the trapped clusters are also ill defined. In the case of these devices the conductance takes place through a disordered three dimensional cluster or even several such clusters.
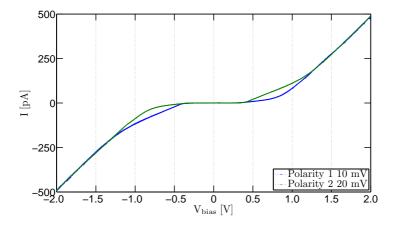
Figure A.1: An *IV* measurement of a device with nanoparticles trapped in a nanogap. The two curves in the figure were measured with two different polarities. The reversal of the asymmetry along with the reversal of the polarity of the sample indicate that the transport through the device is asymmetric. The voltage and current are not scaled to account for the number of junctions in the device since we do not know how many nanoparticles take part in the transport.
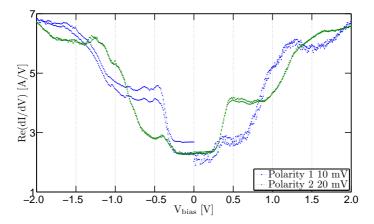

Figure A.2: *dI/dV* measurements of the same device as in Figure A.1. The *dI/dV* has many features, but since we do not know the sizes and the number of nanoparticles in the gap it is impossible to assign the features to specific processes.
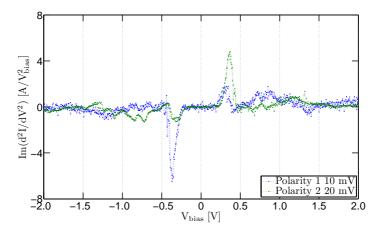
Figure A.3: The d^2I/dV^2 measurements of the same device as in Figure A.1. The asymmetry of the device is clearly visible.

From these first measurements we have learned that the nanogaps fabricated in the Group of Klaus Leifer offer an interesting platform for transport measurements on molecular junctions on a substrate. At the moment it is difficult to interpret the data obtained from these devices due to the fact that the size of the nanoparticles trapped in the them are small compared to the width of the nanogaps and there is a relatively large size distribution of the nanoparticles. Because of this it is impossible to predict how the current will flow through the nanoparticle clusters trapped in these devices. As discussed in Chapter 5 features in the IETS below the threshold for conduction, V_{th}, are masked by Coulomb blockade. The small nanoparticles trapped in these gaps have a threshold voltage of $V_{th} \approx 200 - 300$ mV. As discussed in Chapter 6 many phonon modes active in transport have energies between $50 - 300$ meV. These modes cannot be observed if the threshold voltage to overcome Coulomb blockade is as high as it is in these devices.

A solution to this problem would be to trap nanoparticles of the same diameter or larger than the nanogap width. If this were done it would be possible to create double junction devices and thus certainly only having one or two molecular junctions in series. Nanoparticles with a diameter of ~ 20 nm should be large enough to accomplish this. These nanoparticles would have charging energy of $E_c = 30$ meV and a threshold voltage to overcome Coulomb blockade of $V_{th} = 60$ mV. Thus, opening up the possibility to measure phonon energies above ~ 60 meV.

Appendix B

Measurements on nanoparticles using KPFM

It is of interest to measure the which conducting paths are most favourable in the nanoparticle arrays. Until now, we do not have detailed knowledge of how the nanoparticle array contacts the electrodes or how grain boundaries or defects influence the transport in the arrays. One way of answering these questions is by Kelvin probe force measurements (KPFM) [49]. Using KPFM it is possible to map out the current paths in the devices. In a collaboration with Thilo Glatzel and Marcin Kisiel, in the group of Ernst Meyer at Basel University, have started looking at the arrays with a KPFM.

So far we have not been able to measure the details of the transport using the method. This is due to the fact that the measurement is apparently quite difficult and requires the use of a well tuned instruments. Preliminary measurements show that it is possible to correlate a height profile measured with AFM to the contact potential measured with the KPFM. Figure B.1 shows an example of an AFM and a KPFM measurement on one device. The dark area on the right side of the figures is the substrate and the bright area on the left side is the nanoparticle array.

Since these measurements were made the KPFM has been optimised and now it should be possible to make more detailed measurements. Three is mutual interest in continuing the collaboration and we hope to have nice measurements in the future.
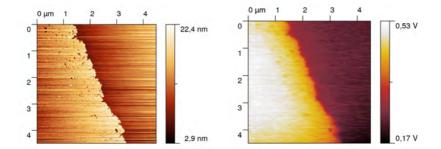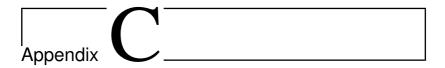
Figure B.1: AFM and KPFM measurements on a nanoparticle array. There figures show that it is possible to distinguish between the nanoparticle array and the substrate using AFM and KPFM. The dark area on the right side of the figures is the substrate and the bright area on the left side is the nanoparticle array.

Appendix C

Images of suspended nanoparticle arrays

In a collaboration with Susanne Baumann, a student at the Basel University, we tried fabricating freely suspended nanoparticle arrays. Two methods were tried. One focused on fabricating small nanoparticle arrays as described in Chapter 4. As a last step, after stamping the nanoparticles on the devices, the SiO_2 was etched away using buffered HF. After the HF etching the SiO_2 supporting the nanoparticles should be gone and the nanoparticle array free standing. On occasion, devices containing suspended nanoparticle arrays were observed by SEM. Figure C.1 shows a device where a nanoparticle array is suspended between two electrodes.
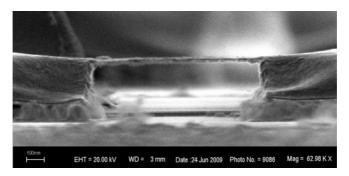
Figure C.1: An SEM image of a suspended nanoparticle array.

Looking closely at the SEM images and looking at several devices it became apparent that the nanoparticle array was not truly free–standing but supported by

an unknown film. Figure C.2 shows how the nanoparticles are supported by a gray film.
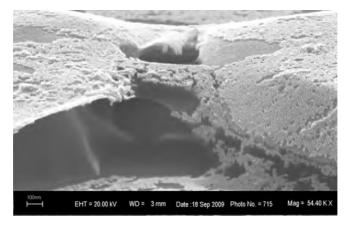

Figure C.2: An SEM image of a suspended nanoparticle array. The nanoparticles bridging the electrodes are supported by an unknown gray film.

Most devices looked like the one shown in Figure C.3. Although beautiful, they are useless for scientific measurements of transport.
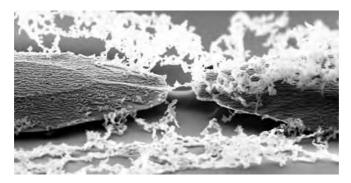

Figure C.3: An SEM image of a suspended nanoparticle array. After etching beautiful nanoparticle assemblies decorate the sample.

A different approach to fabricate free–standing nanoparticle arrays was implemented by Susanne Baumann. She made free–standing nanoparticle arrays which

spanned the openings of TEM grids. Figure C.4 shows an optical image of nanoparticle arrays spanning an opening in a TEM grid. Depositing these suspended nanoparticle arrays was problematic. Liao et al. [45] make free–standing nanoparticle arrays in a similar fashion and use high pressure air to transfer the nanoparticle array from the TEM grid to the substrate. Unfortunately we did not think of this.
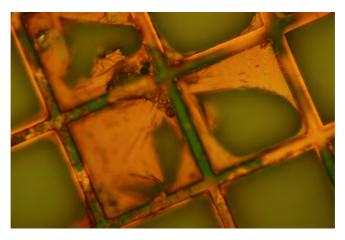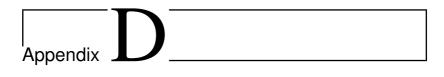

Figure C.4: An optical image of a suspended nanoparticle array in a TEM grid.

Protocol for nanoparticle array fabrication

All chemicals used in the synthesis and suspension of the nanoparticles were bought at Sigma–Aldrich and used as received unless otherwise stated. The di–ionised water had a resistivity greater than 13 MΩ–cm.

D.1 Au nanoparticle Synthesis

Colloidal gold particles, with a diameter of 10 nm, were formed by the reduction of gold(III) chloride hydrate (HAuCl$_4$·4H$_2$O, ACS reagent $\geq$ 49% Au basis) by sodium citrate tribasic dihydrate (C$_6$H$_5$O$_9$Na$_3$·2H$_2$O, for molecular biology $\geq$ 99.5%) and tannic acid (C$_{76}$H$_{52}$O$_4$6, ACS reagent)[71].

D.1.1 Solutions used

The solutions used are:

- 1 ml 1% (w/v) gold(III) chloride hydrate (HAuCl$_4$·4H$_2$O) in DI–H$_2$O.

- 4 ml 1% (w/v) sodium citrate tribasic dihydrate (C$_6$H$_5$O$_9$Na$_3$·2H$_2$O) in DI–H$_2$O.

- 80 μl 1% (w/v) tannic acid (C$_{76}$H$_{52}$O$_4$6) in DI–H$_2$O.

D.1.2 Protocol

- Use two beakers (a) 150 ml and (b) 25 ml.

- Clean beakers thoroughly using water and soap. Rinse using DI-H$_2$O.

- Turn hotplate to 80°C.

- In beaker (a) put:
    - 1 ml gold(III) chloride hydrate (HAuCl$_4$·4H$_2$O).
    - 79 ml DI-H$_2$O.
    - Place magnetic stirrer in beaker and turn on stirring.
    - Cover beaker.
    - Heat to 80°C on hotplate (10-15 min).

- In beaker (b) put:
    - 4 ml sodium citrate tribasic dihydrate (C$_6$H$_5$O$_9$Na$_3$·2H$_2$O), for 10 nm gold colloids.
    - 80 μl tannic acid (C$_{76}$H$_{52}$O$_{46}$).
    - Add water to fill 20 ml.
    - Cover beaker.
    - Heat to 80°C on hotplate (10-15 min).

- Turn hotplate to 250°C, wait 5 min.

- Quickly pour the contents of beaker (b) into beaker (a).

- The solution will turn purple.

- Wait until the solution color changes to red.

- When solution is red wait 10 more minutes.

- Cool solution to room temperature by placing the beaker in ice water. Stir continuously.

D.1.3 Extracting gold colloids and covering with a ligand

The gold colloids need to be extracted from the aqueous solution. This is done using a high–speed centrifuge, Heraeus Biofuge Pico.

- Place the colloid solution into test tubes. 1 ml into each eppendorf.

- Place eppendorfs symmetrically into centrifuge.

- Run centrifuge at 13 krpm for 45 min.

- Clean a 20 ml bottle with ethanol (CH_3CH_2OH, ACS reagent, absolute alcohol, without additive $\geq 99.8\%$).

- With a pipette carefully remove water from the colloids.

- Mix colloids and the remaining water.

- Infuse ethanol in each eppendorf.

- Mix with shaker.

- Transfer the ethanol–colloid solutions from all eppendorfs into the 20 ml bottle.

- Put the solution in an ultrasonic bath for 10 min (sweep) at a temperature below 30°C.

- Add 200 μl of the desired covering molecule to the bottle. 1–Octanethiol ($CH_3(CH_2)_7SH$, $\geq 98.5\%$, distilled before usage) or 1–Dodecanethiol ($CH_3(CH_2)_{11}SH$, $\geq 98\%$).

- Fill the bottle with ethanol.

- The color changes as the molecules cover the gold particles.

- Wait 2–3 days for the molecules to form a ordered layer on the gold

D.1.4 Washing the colloids

After the colloids have settled in the bottom of the small bottle the excess ligands can be removed and the colloids washed in Ethanol before they can be used as an ink for stamping.

  After this process the solution can be stored for up to a week before it is ruined.

- With a pipette remove excess solution from colloids.

- Infuse new ethanol.

- Wait until colloids precipitate, about 1 hr.

- Remove all ethanol, very carefully.

- Infuse 4 ml chloroform ($CHCl_3$, ACS spectroscopy grade $\geq 99.8\%$, 0.5–1.0% Ethanol).

- To disperse colloids put the bottle in ultrasonic bath at room temperature for 10 min.

- The solution turns red when ready.

D.2 Colloid density

The number of 10 nm diameter colloids resulting from the reduction of 1 ml 1% (w/v) $HAuCl_4 \cdot 4H_2O$ can be calculated as:

$$\frac{1}{100} \text{ g} = HAuCl_4 \cdot 4H_2O \tag{D.1}$$

$$HAuCl_4 \cdot 4H_2O = 411.8 \text{ Amu} \tag{D.2}$$

$$Au = 197 \text{ Amu} \tag{D.3}$$

The density of gold is:

$$D_{Au} = 19300 \frac{\text{kg}}{\text{m}^3} \tag{D.4}$$

$$D_{Au} = 1.93 \times 10^{-20} \frac{\text{g}}{\text{nm}^3} \tag{D.5}$$

The volume of a 10 nm diameter colloid is:

$$V_{Colloid} = \frac{4}{3}\pi r^3 \tag{D.6}$$

$$V_{Colloid} = 524 \text{ nm}^3 \tag{D.7}$$

The mass of one colloid is then:

$$M_{Colloid} = V_{Colloid} \times D_{Au} \tag{D.8}$$

$$M_{Colloid} = 1 \times 10^{-17} \text{ g} \tag{D.9}$$

The total mass of Au in the solution is:

$$M_{Auinsol} = \frac{197 \text{ Amu}}{411.8 \text{ Amu}} \times \frac{1}{100} \text{ g} \tag{D.10}$$

$$M_{Auinsol} = 4.8 \times 10^{-3} \text{ g} \tag{D.11}$$

And the total number of colloids in the solution is then:

$$\#_{Colinsol} = \frac{4.8 \times 10^{-3} \text{ g}}{1 \times 10^{-17} \text{ g}} \tag{D.12}$$

$$\#_{Colinsol} = 4.8 \times 10^{14} \text{ Colloids} \tag{D.13}$$

The colloid density is

$$\frac{4.8 \times 10^{14} \text{ Colloids}}{80 \text{ ml}} = 6 \times 10^{12} \text{ Colloids/ml} \tag{D.14}$$

The colloid density in the chloroform solution is

$$\frac{6 \times 10^{12} \text{ Colloids/ml} \times 10 \text{ ml}}{4 \text{ ml}} = 1.5 \times 10^{13} \text{ Colloids/ml} \tag{D.15}$$

D.3 Preparation of masters for PDMS stamps using UV lithography

The masters for the PDMS stamps were made by patterning SU–8 on a SiO_2 substrate.

- Spin:
    - 500 rpm - ramp time 5 s - for 10 s
    - 4000 rpm - ramp time 9 s - for 30s
- Bake: 1 min @ 95° C
- Expose: 2.5 s (i-line), 6s Hard Contact (1.2-1.3 Bar) (33mW/cm2*s)
- Bake IMMEDIATELY after exposure: 1 min @ 95°C.
- Develop: SU-8 developer for 1 min
- Clean and dry in IPA
- Hard bake: 10min @ 200°C

D.4 PDMS

Stamps are made from PDMS molded on the SU8 masters fabricated using UV lithography. The PDMS, SYLGARD® 184 SILICONE ELASTOMER KIT, is used as bought from Dow Corning.

- In a small vile pour 15 ml of base and 2 ml of the curing agent.
- Stir well, until a uniform distribution of small bubbles has formed.
- In a petri dish pour the PDMS over the substrates.
- Wait until no bubbles are close to the substrates, at least 30 min.
- Heat an oven to 60°C.
- Bake PDMS for 90 minutes.
- Let PDMS cool down and carefully pull it out of the petri dish.

- Using a sharp knife peel off the thin PDMS layer on the bottom of the masters.

- Cut slightly along the edges of the masters and carefully remove them from the PDMS.

- After you remove the masters from the PDMS there should be no PDMS left on the top surface of the Si masters. The transferred pattern is visible in the PDMS.

- Use a razor blade to cut out each PDMS stamp.

- Clean stamps in ethanol ultrasonic bath for 5 min.

D.5 Transferring patterns using PDMS stamps

Using a colloid solution in chloroform as ink and PDMS stamps self assembled arrays can be transferred to a substrate [62, 61]

Use a petri dish with three glass slides stacked in the bottom on two sides. Before placing the Teflon ring in the dish, clean the Teflon ring thoroughly using soap and water then rinse with DI–H_2O.

Place the Teflon ring on the glass slide stacks and carefully infuse 29 ml DI-H_2O into the dish outside of the Teflon ring. The colloid solution can be suspended on the water surface for the self assembled monolayer (SAM) to form.

- Turn on airflow in the fume hood, to help solvent to evaporate.

- Use a regular pipette to put $350 \sim 400\,\mu$l of solution into a small vial.

- Using a glass pipette empty the vial and place the solution in the centre of the Teflon ring.

- Wait 10-15 min until all the solvent has evaporated.

- Carefully bring PDMS stamp to touch the surface. Hold the stamp at the surface for 10 sec.

- Tilt the stamp to break contact with the surface and remove it.

- Dry off all excess water on the stamp.

- Place the stamp on the petri dish.

- By dropping, place a substrate on top of the stamp.

- Wait 10 sec. and remove the substrate from the stamp.

D.6 Fabrication of small nanoparticle arrays

D.6.1 Substrate cleaning and preparation of PMMA

- Use highly p– doped Si substrate, resistivity ∼ 10 $\mu\Omega$–cm dopant boron. Thermal oxide thickness 400nm.

- Clean substrate in a ultrasonic bath first with acetone (C_3H_6O, for analysis from Merck Chemicals), then isopropanol (C_3H_8O, for analysis from Merck Chemicals) for 10min each solvent. Dry sample with nitrogen gas.

- Clean substrate in UV ozone for 10 min (Jelight Company model 42).

- Spin on a 120nm thick layer of PMMA–MA 33% (AR–P 671.09 950K from ALLRESIST) at 2000 rpm, ramp 4sek, and duration 40sek.

- Bake PMMA–MA on a hot plate at 200°C for 10min.

- Spin 600-700nm thick PMMA (AR–P 671.09 950K from ALLRESIST, diluted) at 4000rpm, ramp 4sek, and duration 40sek.

- Bake on a hotplate at 180°C for 10min.

D.6.2 E–beam writing and development

Structures written in Zeiss Supra 40 SEM.

- Acceleration voltage: 30 kV

- Working distance: 9 mm

- Area dose: 290 μAs/cm^2.

- Aperture for large structures: 120 μm.

- Write field size: 1000 μm.

- Dose factor: 1.2

- Aperture for small structure: 10 μm.

- Write field size: 100 μm.

- Dose factor: 1.2

Develop in 1:3 4–methyl–2–pentanone(MIBK, $C_6H_{12}O$):isopropanol for 90 seconds. Clean in oxygen plasma using a Oxygen Plasmalab[80 Plus] reactive ion etcher (RIE) from Oxford:

- Background pressure: 5×10^{-5} mTorr

- Working pressure: 250 mTorr

- O_2 flow: 16 sccm

- Power: 30 W

- Time: 20 sec

D.6.3 Metal evaporation

Meta evaporation is performed in a Sharon Vacuum evaporator. The Ti and Au films are evaporated with electron beam evaporation, while the Cr film is evaporated thermally. Figure D.1 shows how the metal electrodes are evaporated on the substrate. The goal of the angular evaporation is to fabricate a relatively smooth height gradient from the metal electrodes to the bare SiO_2 separating them. The process yields metal electrodes approaching the SiO_2 in three steps each having a smaller height than an individual nanoparticle diameter. This will prevent the nanoparticle array from braking when deposited on top of the structure. The structure is composed of a Ti adhesion layer, an Au conducting layer, and a Cr etching mask.

After the metal evaporation liftoff is performed in heated acetone. After liftoff the samples are rinsed in isopropanol and UV ozone for 10min. The liftoff and isopropanol rinse are performed in an ultrasonic bath at 20% power. Fresh layers of PMMA–MA/PMMA are spun on using the process describe in section D.6.1. Small bridges, bridging the metal electrodes, are written. This is done using the same parameters as for the small structures in Sub.Sec D.6.2.

After e–beam writing the substrate is developed as before in 1:3 MIBK:Isopropanol for 90sec. After developing the sample is further cleaned in O_2 plasma as above.

A 45nm Cr etching mask is evaporated onto the substrate. The evaporation is performed at room temperature and under $0°$ angle. After evaporation liftoff is performed as described above.

D.6.4 SiO_2 etching

To fabricate small structures of nanoparticle arrays one needs to pattern the SiO_2 substrate, since the PDMS is too flexible to support these small structures. Using Cr as an etching mask, the SiO_2 can be etched away leaving a raised structure with metal contacts on top separated by exposed SiO_2. The SiO_2 etching is performed using reactive ion etching (RIE). This etching method is more anisotropic than hydrofluoric acid (HF) etching. During RIE etching of the SiO_2 using CHF_3 as an etching gas a fluorocarbon polymer is deposited on the side walls of the structure. This polymer is almost impossible to remove, but the remaining polymer can be kept to a minimum
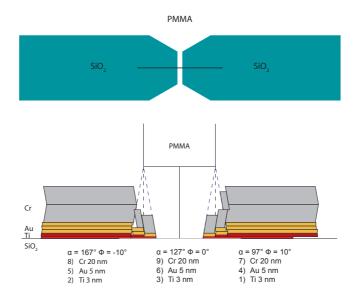
Figure D.1: The evaporation process for the large contact pads. At the top the structure of the electrodes is shown from above as written by the e–beam. The green areas represent the exposed SiO_2 and the white areas represent the PMMA. The horizontal line represents a cut through the structure. The bottom figure shows a side view of the metallic layers as deposited onto the substrate. The view is along the line cut shown in the top figure. The α values represent the angle chosen on the evaporator sample holder and Θ the relative angle between the normal of the substrate and the incoming metal atoms. The numbers followed by a metal and a thickness (i.e. 1) Ti 3nm) represent the order of the evaporated layers, the evaporated metal and the thickness of the evaporated metal. The coverage of the last 20nm Cr metal layer is not depicted in the figure.

in two ways. During CHF_3 etching small amount of O_2 is mixed with the CHF_3. After etching with CHF_3 the deposited polymer can be oxidised in a O_2 plasma and removed using heated Acetone in an ultrasonic bath. The normal etching process is described below in table D.1.

Pressure [mTorr]	O_2 flow [sccm]	CHF_3 flow [sccm]	power [W]	time [m:s]
25	16	0	100	2:00
25	2	40	100	20:00
250	16	0	100	2:00

Table D.1: The RIE etching process. This process will etch ~200nm of SiO_2.

D.6.5 Cr etching

The Cr etching mask is removed using a solution of ceric ammonium nitrate $((NH_4)_2Ce(NO_3)_6$, CAN) in Di–H_2O and Acetic acid (CH_3COOH):

- 10ml Di–H_2O

- 2g CAN

- 260μl Acetic acid

The etching rate of the solution is ∼ 3 nm/sec if the sample is dipped in an only slightly agitated. To fully remove the Cr the etching is performed in a ultrasonic bath at 20% power for 3min.
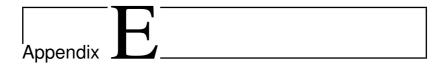
D.6.6 Stamping of Au nanoparticle arrays

When the raised structures have been prepared the nanoparticle arrays are stamped on top of them using a PDMS stamp with no pattern.

D.7 Molecular place exchange

For 2 mg OPE dithiol (426.55 g/mole) in 3 ml THF:

- Weigh molecule and add in a flask

- Infuse THF to the flask

- Bubble with Ar for 1–2 minutes

- Add 20 μL ammonium hydroxide Sigma Aldrich is 17837-100ML

- Bubble with Ar for 1–2 minutes

- Drop sample in the flask. Structures facing down.

- Store under Ar atmosphere over night

- Remove sample rinse twice with THF

- Dry sample

Appendix E

Electrical characterisation of the dip–stick

E.1 Frequency response of 10 GΩ resistor in the dip–stick

The frequency response of a 10 GΩ resistor in the dip–stick at room temperature is shown in figure E.1. The blue marks are the measured points and the blue dotted line a guide to the eye. The green line is a model of the differential conductance assuming a parallel connection of a resistor $R = 11$ GΩ and a capacitor $C = 2.1$ pF

$$\frac{dI}{dV} \quad = \quad \frac{1}{R} + i\omega C \tag{E.1}$$

The chip carrier is connected to a break out box with a flat ribbon cable of twisted pair wires. During the measurement wire 6 and 16 were used. They belong to the third and eighth twisted pairs respectively. To reduce the capacitive cross talk between them all the unused wires were grounded.

Using equation E.1 one can get the differential conductance of the equivalent circuit measured, assuming the circuit consists of the resistor being measured in parallel with a stray capacitance to ground. From the real part of the dI/dV measurement one gets the value of the resistor $R = 1/\mathrm{Re}\{dI/dV\} = 11$ GΩ and from the imaginary part of the signal one gets the value of the stray capacitance to ground $C = \mathrm{Im}\{dI/dV\}/(\omega) = 2.1$ pF.

The d^2I/dV^2 measurements show only noise when the resistor is measured. This is expected since the impedance of the equivalent circuit should not depend on voltage.
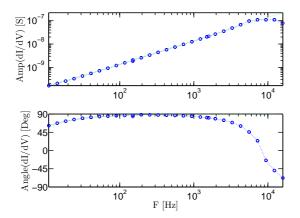
Figure E.1: The frequency response of a 10 GΩ resistor in the dip–stick. The blue marks are the measured data point and the blue dotted line a guide for the eye. The green line is a model of the differential conductance of the system with $C = 2$ pF and $R = 10$ GΩ. The bandwidth of the IV converter is reached around 5 kHz.
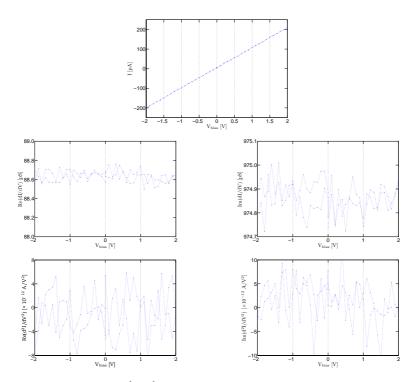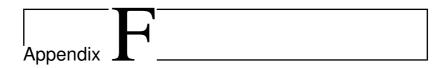
Figure E.2: *IV*, *dI/dV*, and d^2I/dV^2 measurement of a 10 GΩ resistor in the dip–stick. The *dI/dV* and d^2I/dV^2 are measured at a frequency of 73 Hz. From the *IV* and the real part of the *dI/dV* one can see that the resistance of the resistor is $R = 11$ GΩ. From the imaginary part of the *dI/dV* one can calculate the capacitance $C = 2.1$ pF.

Appendix F

Taylor expansion of the current measured

F.1 Details of the Taylor expansion of the current measurements

The current flowing in the device is comprised of an ac part and a dc part and can be expressed by a Taylor series as

$$I(V_{dc} + V_{ac}\sin(\omega t)) \quad = \quad I(V_{dc}) + \frac{dI(V_{dc})}{dV}V_{ac}\sin(\omega t)$$
$$+\frac{1}{2}\frac{d^2I(V_{dc})}{dV^2}V_{ac}^2\sin^2(\omega t) + \cdots \tag{F.1}$$

$$\sin^2(\omega t) \quad = \quad \frac{1 - \cos(2\omega t)}{2} \tag{F.2}$$

$$I(V_{dc} + V_{ac}\sin(\omega t)) \quad = \quad I(V_{dc}) + \frac{dI(V_{dc})}{dV}V_{ac}\sin(\omega t) + \frac{1}{4}\frac{d^2I(V_{dc})}{dV^2}V_{ac}^2\cos(2\omega t + \pi)$$
$$+\frac{d^2I(V_{dc})}{dV^2}\frac{V_{ac}^2}{4} + \cdots \tag{F.3}$$

Assuming a circuit comprised of a parallel connection of a resistor with conductance G and a capacitor C the $dI(V_{dc})/dV$ in (F.3) can be written as:

$$\frac{dI(V_{dc})}{dV} \quad = \quad G + C\frac{d}{dt} \tag{F.4}$$

inserting (F.4) into (F.3) gives

$$
I(V_{dc} + V_{ac}\sin(\omega t)) \;=\; I(V_{dc}) + \left(G + C\frac{d}{dt}\right)V_{ac}\sin(\omega t)
$$

$$
+\frac{1}{4}\frac{d}{dV}\left(G + C\frac{d}{dt}\right)V_{ac}^2\cos(2\omega t + \pi)
$$

$$
+\frac{d}{dV}\left(G + C\frac{d}{dt}\right)\frac{V_{ac}^2}{2} + \cdots \tag{F.5}
$$

The phase of the current is composed of an in phase part, $\propto \sin(\omega t)$, and an out of phase part, $\propto \cos(\omega t)$. The second term in (F.5) can then be represented as

$$
\left(G + C\frac{d}{dt}\right)V_{ac}\sin(\omega t) \;=\; GV_{ac}\sin(\omega t) + \omega C V_{ac}\cos(\omega t), \tag{F.6}
$$

where the conductance of the device is proportional to the in phase part of the signal and the capacitance as the out of phase part of the signal. Assuming that the resistor and capacitor are voltage controlled the third term in (F.5) can then be represented as

$$
\frac{1}{4}\frac{d}{dV}\left(G(V_{dc}) + C(V_{dc})\frac{d}{dt}\right)V_{ac}^2\cos(2\omega t + \pi) \;=\; \frac{1}{4}\frac{d}{dV}G(V_{dc})V_{ac}^2\cos(2\omega t + \pi)
$$

$$
+\frac{\omega}{2}\frac{d}{dV}C(V_{dc})V_{ac}^2\sin(2\omega t), \tag{F.7}
$$

where the voltage derivative of the conductance is proportional to the second harmonic of the out of phase part of the signal and the voltage derivative of the capacitance is proportional to the second harmonic of the in phase part of the signal.

As Equations F.6 and F.7 show the conductance G and capacitance C can be measured directly by measuring the in phase out of phase components of the ac current, respectively. The voltage derivative of the resistance and capacitance can also be measured directly by measuring the out of phase and in phase parts of the second harmonic of the ac current, respectively.

Appendix G

Error calculations

G.1 Calculation of the broadening in the Coulomb blockade induced feature due to disorder in the nanoparticle array

Nanoparticle capacitance in a nanoparicle array:

$$
\begin{aligned}
C &= 4\pi\epsilon_0\epsilon_r \frac{R(R+s)}{R} \\
\delta C &= 4\pi\epsilon_0\epsilon_r \sqrt{\left(\frac{2R+s}{s}\delta R\right)^2 + \left(\frac{2R^2}{s^2}\delta s\right)^2}
\end{aligned}
\tag{G.1}
$$

where ϵ_0 is the permittivity of vacuum, ϵ_r the dielectric constant, R the nanoparticle radius, and s the interparticle distance. The error in the capacitance δC is due to the error in the nanoparticle radius and the interparticle distance.

Charging energy.

$$
\begin{aligned}
E_c &= \frac{e^2}{2C} \\
\delta E_c &= \frac{e^2}{2C^2}\delta C
\end{aligned}
\tag{G.2}
$$

where e is the elementary charge of an electron.

Voltage to over come Coulomb blockade:

$$V_{\mathrm{CB}} = \frac{2E_{\mathrm{c}}}{e}$$

$$\delta V_{\mathrm{CB}} = \frac{2\delta E_{\mathrm{c}}}{e} \tag{G.3}$$

Reduction factor of threshold voltage due to temperature:

$$P(T) = \frac{4.8 k_{\mathrm{B}} T}{\rho_{\mathrm{c}} E_{\mathrm{c}}}$$

$$\delta P(T) = \frac{2 \cdot 4.8 k_{\mathrm{B}} T}{\rho_{\mathrm{c}} E_{\mathrm{c}}^2} \delta E_{\mathrm{c}} \tag{G.4}$$

where k_{B} is the Boltzmann constant, T the temperature, and $\rho_{\mathrm{c}} = 2\sin(18/\pi)$ the percolation threshold in a hexagonally closed array.

Threshold voltage:

$$V_{\mathrm{th}} = V_{\mathrm{CB}}(1 - P(T))$$

$$\delta V_{\mathrm{th}} = \sqrt{((1 - P(T))\delta V_{\mathrm{CB}})^2 + (V_{\mathrm{CB}}\delta P(T))^2} \tag{G.5}$$

Threshold voltage per molecular junction:

$$V_{\mathrm{th\,j}} = \frac{V_{\mathrm{th}}}{N}$$

$$\delta V_{\mathrm{th\,j}} = \sqrt{\left(\frac{\delta V_{\mathrm{th}}}{N}\right)^2 + \left(\frac{V_{\mathrm{th}}}{N^2}\delta N\right)^2} \tag{G.6}$$

where N is the number of nanoparticles spanning the gap between the electrodes.

The number of nanoparticles spanning the gap between the electrodes:

$$N = \frac{L}{2R + s}$$

$$\delta N = \sqrt{\left(\frac{\delta L}{2R + s}\right)^2 + \left(\frac{L}{(2R + s)^2}\delta s\right)^2 + \left(\frac{L}{(2R + s)^2}2\delta R\right)^2} \tag{G.7}$$

G.2 Calculation of the broadening in the Coulomb blockade induced feature due to charge disorder in the nanoparticle array

Assuming the model shown in Figure 5.1 with $C_1 = C_2$ and the charge on the nanoparticle $Q = 0$. The change in the energy of the nanoparticle when a single

charge is added to it is:

$$\Delta U^{\pm} \quad = \quad \frac{(Q \pm e)^2}{2C} - \frac{Q^2}{2C} \tag{G.8}$$

where e is the charge of an electron and $C = C_1 + C_2$ is the capacitance of the nanoparticle. Now the error in the energy U due to charge disorder δQ and disorder in the nanoparticle capacitance δC, from Equation G.1 is:

$$\delta \Delta U^{\pm} \quad = \quad \sqrt{\left(\frac{2e\delta Q}{2C}\right)^2 + \left(\frac{e^2 \delta C}{2C^2}\right)^2} \tag{G.9}$$

where δ denotes the error of $\delta U^{\pm}$. The error of $\delta U^{\pm}$ is carried to the change in energy when an electron tunnels onto or off the nanoparticle. The change in energy is given by:

$$\Delta E_1^{\pm} \quad = \quad \Delta U^{\pm} \mp e\frac{C_2}{C_{\Sigma}}V_{\mathrm{b}}$$

$$\Delta E_2^{\pm} \quad = \quad \Delta U^{\pm} \pm e\frac{C_1}{C_{\Sigma}}V_{\mathrm{b}} \tag{G.10}$$

as given by Equation 5.4. The error of $\Delta E_j^{\pm}$, $j = 1, 2$, due to the error in $\Delta U^{\pm}$ is:

$$\delta \Delta E_j^{\pm} \quad = \quad \sqrt{(\delta \Delta U^{\pm})^2 + \sqrt{2}\left(\frac{eV_{\mathrm{b}}\delta C}{C}\right)^2} \tag{G.11}$$

where V_{b} is the bias applied to the junction. Combining Equations 5.1, 5.3, 5.4, and 5.7 the threshold voltage for conductance in the presence of Coulomb blockade in a symmetric double junction is found as in Equation 5.10, but with errors added

$$- (E_{\mathrm{c}} \pm \delta \Delta E_j^{\pm}) \leq \frac{1}{2}eV_{\mathrm{b}} \leq (E_{\mathrm{c}} \pm \delta \Delta E_j^{\pm}) \tag{G.12}$$

which gives the voltage needed to over come Coulomb blockade with errors due to charge disorder and errors in the nanoparticle capacitance

$$|V_{\mathrm{CB}}| \quad = \quad 2E_{\mathrm{C}}/e$$

$$\delta|V_{\mathrm{CB}}| \quad = \quad 2\delta \Delta E_j^{\pm}/e \tag{G.13}$$

The error of $|V_{\mathrm{CB}}|$ is carried forward to the threshold voltage as shown in Equation G.6.
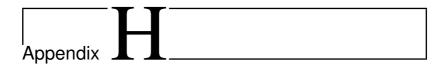
G.3 Calculation of the broadening of peaks beyond the threshold voltage due to variations in the interparticle separation

The nanoparticles in the array are capacitively coupled. We make the assumption that that the voltage drop between two neighbouring nanoparticles will depend on the capacitance between the nanoparticles[2, 24, 47]. In the terms of the double junction tunnelling model the voltage is found as in Equation 5.5:

$$V_j \quad = \quad \frac{C_1 C_2}{C_j C_\Sigma} V_b \tag{G.14}$$

where C_j is the capacitance of the individual junction, $C_\Sigma = C_1 + C_2$ is the sum of the capacitances of the junctions, V_b is the applied bias voltage, the number of nanoparticles in series bridging the electrodes. Using Equations G.14 and G.1 the broadening in the voltage between the nanoparticles can be calculated as:

$$\delta V_{ij} \quad = \quad \frac{1}{\sqrt{1}} \frac{\delta C}{C} \tag{G.15}$$

Appendix H

Literature values of phonon modes in molecules

H.1 Phonon modes in $CH_3(CH_2)_8SH$ and $CH_3(CH_2)_7SH$ molecules on an Au surface.

Mode	Wavenumber [cm^{-1}]	Energy [meV]	Molecule	Method	Reference
Au–S stretch	225	28	$CH_3(CH_2)_7SH$	HREELS	[36]
Au–S stretch	255	32	$CH_3(CH_2)_7SH$	HREELS	[36]
SCC deform CCC deform	385	48	$CH_3(CH_2)_7SH$	HREELS	[36]
$\nu(C\text{–}S)_G$	641	79	$CH_3(CH_2)_8SH$	RAMAN	[11]
$\nu(C\text{–}S)_T$	706	88	$CH_3(CH_2)_8SH$	RAMAN	[11]
CH_2 rock	715	89	$CH_3(CH_2)_7SH$	HREELS	[36]
CH_2 rocking	720	89	$CH_3(CH_2)_5CH_3$	IR	[12]
CH_2 rocking	766	95	$CH_3(CH_2)_5CH_3$	IR	[12]
CH_3 rock	915	113	$CH_3(CH_2)_7SH$	HREELS	[36]
CH_2 rocking	925	115	$CH_3(CH_2)_5CH_3$	IR	[12]
C–C stretch	1050	130	$CH_3(CH_2)_7SH$	HREELS	[36]
$\nu_a(C\text{–}C)_T$	1064	132	$CH_3(CH_2)_8SH$	RAMAN	[11]
$\nu_s(C\text{–}C)_T$	1120	139	$CH_3(CH_2)_8SH$	RAMAN	[11]
CH_3 rock	1190	148	$CH_3(CH_2)_7SH$	HREELS	[36]
CH_2 wagging	1230	152	$CH_3(CH_2)_5CH_3$	IR	[12]
CH_2 twist	1265	157	$CH_3(CH_2)_7SH$	HREELS	[36]
CH_2 wagging	1283	159	$CH_3(CH_2)_5CH_3$	IR	[12]
CH_2 wagging	1330	165	$CH_3(CH_2)_5CH_3$	IR	[12]
CH_3 s–deform	1380	171	$CH_3(CH_2)_7SH$	HREELS	[36]
CH_3 d–deform CH_2 scissors	1455	180	$CH_3(CH_2)_7SH$	HREELS	[36]
$\nu_s(CH_2)$	2854	354	$CH_3(CH_2)_8SH$	RAMAN	[11]
C–H stretch	2860	355	$CH_3(CH_2)_7SH$	HREELS	[36]
$\nu_s(CH_2)$	2880	357	$CH_3(CH_2)_8SH$	RAMAN	[11]
$\nu_s(CH_2)$	2907	360	$CH_3(CH_2)_8SH$	RAMAN	[11]
C–H stretch	2925	363	$CH_3(CH_2)_7SH$	HREELS	[36]
$\nu_s(CH_3FR)$	2936	364	$CH_3(CH_2)_8SH$	RAMAN	[11]
$\nu_s(CH_3)$	2967	368	$CH_3(CH_2)_8SH$	RAMAN	[11]

Table H.1: A summary of phonon modes in alkane thiols. The molecules are adsorbed onto Au surfaces and the phonon modes are investigated by Raman spectroscopy, high–resolution electron–energy–loss spectroscopy (HREELS), and infra red (IR) spectroscopy.

Publication list

Publications in journals

- *In–situ resistivity measurements during growth of ultra–thin $Cr_{0.7}Mo_{0.3}$*
  K. B. Gylfason, A. S. Ingason, J. S. Agustsson, S. Olafsson, K. Johnsen and J. T. Gudmundsson, Thin Solid Films, 2006, 515, p 583-586

- *A magnetron sputtering system for the preparation of patterned thin films and in–situ thin film electrical resistance measurements*
  U. B. Arnalds, J. S. Agustsson, A. S. Ingason, A.-K. Eriksson, K. B. Gylfason, J. T. Gudmundsson, and S. Olafsson, Review of Scientific Instruments, 2007, 78 (10), p 103901

- *Growth, coalesnce and electrical resistivity of thin Pt films grown by dc magnetron sputtering on SiO*
  J. S. Agustsson, U. B. Arnalds, A. S. Ingason, K. B. Gylfason, K. Johnsen, S. Olafsson and J. T. Gudmundsson, Applied Surface Science, 2008, 254 (22), p 7356-7360

- *In–situ electrical characterization of ultrathin TiN films grown by reactive dc magnetron sputtering on SiO*
  A. S. Ingason, F. Magnus, J. S. Agustsson, S. Olafsson, and J. T. Gudmundsson, Thin Solid Films, 2009, 517 (24), p 6731-6736

- *Light–Controlled Conductance Switching of Ordered Metal–Molecule–Metal Devices*
  Sense Jan van der Molen, Jianhui Liao, Tibor Kudernac, Jon S. Agustsson, Laetitia Bernard, Michel Calame, Bart J. van Wees, Ben L. Feringa and Christian Scöhnenberger, Nano Letters, 2009, 9 (1), p 76-80

- *Cyclic Conductance Switching in Networks of Redox–Active Molecular Junctions*
  Jianhui Liao, Jon S. Agustsson, Songmei Wu, Christian Schönenberger, Michel

Calame, Yann Leroux, Marcel Mayor, Olivier Jeannin, Ying-Fen Ran, Shi-Xia Liu and Silvio Decurtins, Nano Letters, 2010, 10 (3), p 759-764

Poseter contributions

- *Ultra–thin Lattice Matched Cr_xMo_{1-x}/MgO Multilayers*
  K. B.Gylfason, J. S. Ágústsson, S. Ólafsson, I. Meyvantsson, K. Johnsen and J. T. Guðmundsson, Poster presented at the 51st American Vacuum Society Symposium, Anaheim, California, November 16. 2004 (J. T. Guðmundsson presented)

- *In–situ Resistivitymeasurements during growth of ultrathin Cr_xMo_{1-x}*
  K. B.Gylfason, Á. S. Ingason, J. S. Ágústsson, S. Ólafsson, K. Johnsen, and J. T. Guðmundsson, Poster presented at the 13th International Congress on Thin Films, Stockholm, Sweden, June 19 - 23, 2005 (K. B. Gylfason presented)

- *Electrical charectization of MgO thin films grown by reactive magnetron sputtering*
  J. T. Guðmundsson, J. S. Ágústsson, K. B. Gylfason, S. Ólafsson, and K. Johnsen, Poster presented at the 13th International Congress on Thin Films, Stockholm, Sweden, June 19 - 23, 2005 (J. S. Ágústsson presented)

- *In–situ Resistivity measurements during growth of ultra thin Cr_xMo_{1-x}*
  K. B. Gylfason, Á. S. Ingason, J. S. Ágústsson, S. Ólafsson, K. Johnsen, and J. T. Guðmundsson, Poster presented at the Natural Science Symposium, Reykjavík, Iceland, March 3 - 4, 2006 (K. B. Gylfason presented)

- *Rafeiginleikar Þunnra MgO húða*
  J. S. Ágústsson, K. B.Gylfason, B. V. Ágústsson, S. Ólafsson, K. Johnsen, and J. T. Guðmundsson, Poster presented at the Natural Science Symposium, Reykjavík, Iceland, March 3 - 4, 2006 (J. S. Ágústsson presented)

- *Hydrogen uptake in MgO thin films grown by reactive magnetron sputtering*
  J. S. Ágústsson, B. V. Ágústsson, A. K. Eriksson, K. B. Gylfason, S. Ólafsson, K. Johnsen, and J. T. Guðmundsson, Poster presented at the 53st American Vacuum Society Symposium, San Francisco, California, November 14. 2006 (J. S. Ágústsson presented)

- *Cyclic conductance switching in networks of redox–active molecular junctions*
  Department of Physics, University of Basel, Switzerland Jianhui Liao, Jon S. Agustsson, Songmei Wu, Christian Schönenberger, and Michel Calame, Poster presented at Swiss nano, 2009 (J. Liao presented)

- *Molecular devices based on arrays of gold nanoparticles*
  Jon S. Agustsson, Haichao Huang, Jianhui Liao, Christian Schönenberger, and Michel Calame, Poster presented at the International Conference on Molecular Electronics, Emmetten, Switzerland, January 5–9. 2010 (J. S. Agustsson presented)

- *Molecular devices based on arrays of gold nanoparticles*
  Jon S. Agustsson, Claire Barrett, Jianhui Liao, Christian Schönenberger, and Michel Calame, Poster presented for the NCCR review panel, 2010 (J. S. Agustsson presented)

Oral presentations

- *Electrical characterization of MgO thin films grown by reactive magnetron sputtering*
  Department of Electrical Engineering, University of Iceland, June 2005

- *Reactive sputtering of oxide thin films*
  Natural Science Symposium, Reykjavík, Iceland, March 3 - 4, 2006

- *Molecules as active components in devices based on networks of molecular junctions.*
  Workshop on molecular electronics, University of Bern, Bern, Switzerland, May 2009

- *Molecules as active components in devices based on networks of molecular junctions*
  Faculty of Science and Technology, L'Université de Haute–Alsace, Mulhouse, France, 2009

- *Molecules as active components in devices based on networks of molecular junctions.*
  FUNMOLS project meeting, Copenhagen, Denmark, September 2009

- *Molecules as active components in devices based on networks of molecular junctions.*
  10th European Conference on Molecular Electronics, Copenhagen, Denmark, September 2009

- *Nanoparticle arrays*
  FunMol project meeting, Basel, Switzerland, October 2009

Acknowledgements

The three and a half years I have spent in Basel have been very rewarding. I have grown academically, personally, and even financially, relative to many of my own countrymen.

I am thankful that Christian Schönenberger took me into his group. He has a talent for creating an particularly friendly and comfortable work environment. It is rare to find a person who can so nicely balance support, friendliness, and yet question every measurement and protocol. I remember meetings where you criticised all my work, but in a way that was constructive and inspired by helpfulness. Those were hard meetings, but also the ones where I came out motivated to answer the questions I could not answer in the meeting.

Of all the people I met during my study Michel Calame is the one who has inspired me the most. You has taught me about science and life. You showed me how to appreciate the best Switzerland has to offer: The food, the wine, and the mountains. Michel you have a special talent of holding my hand and kicking my ass at the same time.

Jianhui Liao was the one who introduced me to the secret of the nanoparticle arrays. He has to be the most patient man I have met. Although we are two very different people, I think we made a good team and I would have loved to work on the suspended arrays with you. I realised how patient you were when I had to teach others to make the arrays. I did not need a lot of patience when I taught Claire Barrett to make the nanoparticle arrays. She picked up on the protocol quickly after she realised to mix the solutions with water and not ethanol. Claire, thank you for the support and all the talks in the last year of my thesis.

Thanks to Aidan Quinn and Sense Jan van der Molen for taking the time and refereeing my thesis defence.

The people who make up the group have made the stay here fun and easy. I have met many interesting and fun people who have helped me develop in many ways. I am truly thankful for the great companionship I have experienced in the group: All the trips to the climbing halls with Andreas Kleine, Jens Schindele, Jan Brunner, Cornelia Nef, and Lukas Hofstetter; The avalanche and mountaineering discussions

My girlfriend María has made my stay here in Switzerland so enjoyable. I am really thankful that she decided to move to Basel with me and partake in this whole adventure. Together we have discovered new ways to enjoy the life in Switzerland and how useful skis are in that respect.